Metallic and molecular ions in the magnetosphere

M. Yamauchi[1], S. Christon[2], I. Dandouras[3], S. Haaland[4], D. Kastinen[1], L.M. Kistler[5], I. Mann[6], S. Nozawa[7], J.M.C. Plane[8], Y. Saito[9], L. Schulz[10], S. Watababe[11], P. Wurz[12], and A.W. Yau[13]

1 Swedish Institute of Space Physics (IRF), Kiruna, Sweden; <M.Yamauchi@irf.se>
2 Focused Analysis and Research (FAR), USA;
3 IRAP, CNRS/U. Toulouse/CNES, France;
4 U Centre Svalbard;
5 U New Hampshire, USA;
6 UiT, Arctic U. of Norway, Tromsø, Norway;
7 Nagoya U, Japan;
8 U Leeds, UK;
9 Institute of Space and Astronautical Science (ISAS), Sagamihara, Japan;
10 TU-Braunschweig, Germany;
11 Hokkaido Information U.;
12 U Bern, Switzerland;
13 U Calgary, Canada;

Abstract

Observations and present knowledge of heavy ions with mass ≥ 27 in the magnetosphere are reviewed. There are four ultimate sources of these heavy ions: the solar wind (mainly high charge-state atomic ions), the ionosphere (mainly molecular ions), the atmospheric metal layers that are originating ultimately from ablation of meteoroids and possibly space debris (low charge-state metallic ions and metal-rich molecular ions), and lunar surface and exosphere (low charge-state metallic and molecular ions).

The upstream heavy ions (solar wind origin and lunar origin) give independent information on the ion entry route to the magnetosphere from proton (H^+) and alpha particles (He^{++}): with similar mass-per-charge (m/q) values, or gyroradius, for the solar wind origin, and much larger gyroradius for the lunar origin. The lunar origin ions also give independent insights from laboratory observations on the sputtering processes. The atmospheric origin molecular and metallic ions are essential in understanding energization, ionization altitudes, and upward transport in the ionosphere during various ionospheric and

magnetospheric conditions. These ions are also important when considering the evolution of the Earth's atmosphere on the geological timescale.

Only a few terrestrial missions have been equipped with instrumentation dedicated to separate these molecular and metallic ions, within only a limited energy range (cold ions of < 50 eV and energetic ions of ~100 keV or more) and a limited mass range (mainly ≤ 40 amu). This is far too limited to make any quantitative discussion on the very heavy ions in the magnetosphere. For example, we cannot dismiss any of four possible sources with the existing data.

Under this circumstance, it is worth to re-examine, using available tools, the existing data from the past and on-going missions, including those not designed for the required mass separation, to search for these ions. The purpose of this review is to summarize the availability of these datasets and tools. This review also shows some examples of combinations of different datasets that provide important indications of the sources of these heavy ions and their amounts that have been overlooked to date.

Finally, we note the possible future contamination of specific masses (mainly Aluminium (Al), but also lithium (Li), iron (Fe), nickel (Ni), copper (Cu), titanium (Ti) and germanium (Ge)) by the ablation of re-entering human-made objects in space (debris and alive satellites) in the coming decades. This possibility argues the need for dedicated observations of magnetospheric and ionospheric metallic ions before these metallic ions of space debris origin start to dominate over the natural contribution. The required observations can be performed with the available designs of space instrumentation and available ground-based instruments.

Acronyms

CIR: Co-rotating interaction region
CME: Coronal mass ejection
ESA: electrostatic analyzer
ESA: European Space Agency
FOV: field of view
IMF: interplanetary magnetic field
IS radar: incoherent scatter radar
LEO: low-Earth orbit
lidar: light detection and ranging (now is accepted as normal noun, though)
MCP: microchannelplate
PHA: pulse height analysis
QL: quick look plot
RPA: retarding potential analyser
SSD: solid-state detector
TOF: time of flight

<u>Space missions and instruments</u>

ACE: Advanced Composition Explorer
  ULEIS: Ultra-Low-Energy Isotope Spectrometer
AE-C and AE-D: Atmosphere Explorer C and D
AMPTE: Active Magnetospheric Particle Tracer Explorers
  CCE/CHEM: Charge-Energy-Mass Spectrometer on board Charge Composition Explorer
  IRM/SULEICA: SUprathermaL Energy Ionic Charge Analyzer on board Ion Release Module
ARGOS/ISAAC: Ionospheric Spectroscopy and Atmospheric Chemistry instrument on board the United States Air Force's Advanced Research and Global Observing Satellite
ARTEMIS: Acceleration, Reconnection, Turbulence and Electrodynamics of the Moon's Interaction with the Sun
ASAN: Advanced Small Analyzer for Neutrals on board Chang'e-4
au: Astronomical unit
Cassini/MIMI-CHEMS: Charge-Energy-Mass Spectrometer of Magnetosphere Imaging Instrument on board Cassini
Chandrayaan-1/SARA: Sub-keV Atom Reflecting Analyser
Cluster/CIS/CODIF: COmposition DIstribution Function of Cluster Ion Spectrometry
CRRES: Combined Release and Radiation Effects Satellite
DE: Dynamics Explorer
  RIMS: Retarding Ion Mass Spectrometer

EICS: Energetic Ion Composition Spectrometer
Geotail:
STICS: Supra-Thermal Ion Composition Spectrometer (STICS)
LEP: Low Energy Particle experiment
ISIS: International Satellites for Ionospheric Studies
JUICE/PEP: Particle Environment Package on board JUpiter ICy moons Explorer
JDC: Jovian Dynamics and Composition
NIM: Neutral gas and Ion Mass spectrometer
LADEE: The Lunar Atmosphere and Dust Environment Explorer
Kaguya/IMA: Ion Mass Analyzer of MAgnetic field and Plasma experiment - Plasma energy Angle and Composition Experiment (MAP-PACE) on board Kaguya
MAVEN/STATIC: SupraThermal And Thermal Ion Composition on board Mars Atmosphere and Volatile Evolution mission
MMS/HPCA: Hot Plasma Composition Analyzer on board Magnetospheric MultiScale mission
OGO: Orbiting Geophysical Observatory satellite
STEREO/PLASTIC: Plasma and Suprathermal Ion Composition on board Solar Terrestrial Relations Observatory
SOHO/CELIAS: Charge, Element, and Isotope Analysis System on board SOlar and Heliospheric Observatory
VAP: Van Allen Probes
Wind STICS: Geotail:
STICS: Supra-Thermal Ion Composition Spectrometer (STICS)

Models
CABMOD: Chemical Ablation Model
LEGEND: LEO-to-GEO Environment Debris model
MASTER: Meteoroid and Space Debris Terrestrial Environment.
ORSAT: Object Reentry Survival Analysis Tool
SAMI: Southern Appalachian Mountains Initiative
SCARAB: SpaceCraft Atmospheric Re-entry and Aerothermal Break-up
WACCM: Whole Atmosphere Community Climate Model
WACCM-X: WACCM with thermosphere and ionosphere eXtension

1. Introduction

Heavy ions have been found in the magnetosphere since the early 1970's (Shelley et al., 1972; Hoffman et al., 1974). Subsequently, magnetospheric ion dynamics has been studied with four major components (H^+, He^{++}, He^+, and O^+). Both helium and oxygen have been used as markers for plasma coming from the solar wind (He^{++}), plasmasphere (He^+), and ionosphere (O^+), respectively, while we cannot distinguish the origin of H^+. The minor components thus give important information regarding the source and transport.

This applies to the even less-abundant minor ions such as molecular ions and metallic ions. The molecular N_2^+, NO^+, or O_2^+ ions, compared to the atomic O^+ ions (without separating from N^+), carry certain important information on the internal processes in the ionosphere as well as the ion outflow processes above the ionosphere. The metallic ions give information on the metal deposit to the mesosphere, mesosphere-thermosphere coupling, as well as on the lunar-origin ions and its entry route to the magnetosphere. Such information is not obtained from the four major ion species (H^+, He^{++}, He^+, and O^+).

For example, the lunar origin ions of four major species are completely masked by those of solar wind origin. Similarly, H^+, He^+, and O^+ originating from the lower part of the ionosphere and mesosphere are masked by those originated at upper ionosphere. Thus, the heavy molecular and metallic ions provide unique information that is not obtained from the four, and contributes to understanding many aspects of the geospace environment: the ion escape process from the ionosphere, related ionospheric and even mesospheric process, deposition of near-Earth small bodies at different altitudes, solar wind-magnetosphere interaction, and even the dynamics of the Moon-origin ions.

The molecular and metallic ions were actually found a long time ago by the ISIS-2 and DE-1 satellites (Hoffman et al., 1974, Chapell et al., 1982, Craven et al., 1985). Despite this, the roles of such heavy ions (mass ≥ 27) and their composition in the terrestrial magnetosphere have received little attention, and the observations of heavy ions and molecular ions in the magnetosphere are sparse. The limited numbers of existing magnetospheric observations are often the bi-products from missions with other prime objectives.

1.1. Four possible sources

For heavy molecular ions, the majority is of ionospheric origin, and supplied mainly from the polar ionosphere (e.g., see review by Lin and Ilie, 2022), but there may be contributions from other sources and via other routes. For the metallic ions with energies greater than 100 keV/q (energy range of Supra-Thermal Ion Composition Spectrometer (STICS) instruments on board Geotail and Wind spacecraft), the majority are high charge-state solar wind ions such as Fe^{12+}, while some ions are low charge-state such as Fe^{+} and K^{+} (e.g., Christon et al., 2017). Considering the ion distribution of the topside ionosphere and its further energization to reach the magnetosphere against the escape energy, the supply of metallic ions from the ionosphere to the magnetosphere is expected to be very small. This makes it difficult to understand how these metallic ions are provided to the magnetosphere and where they come from.

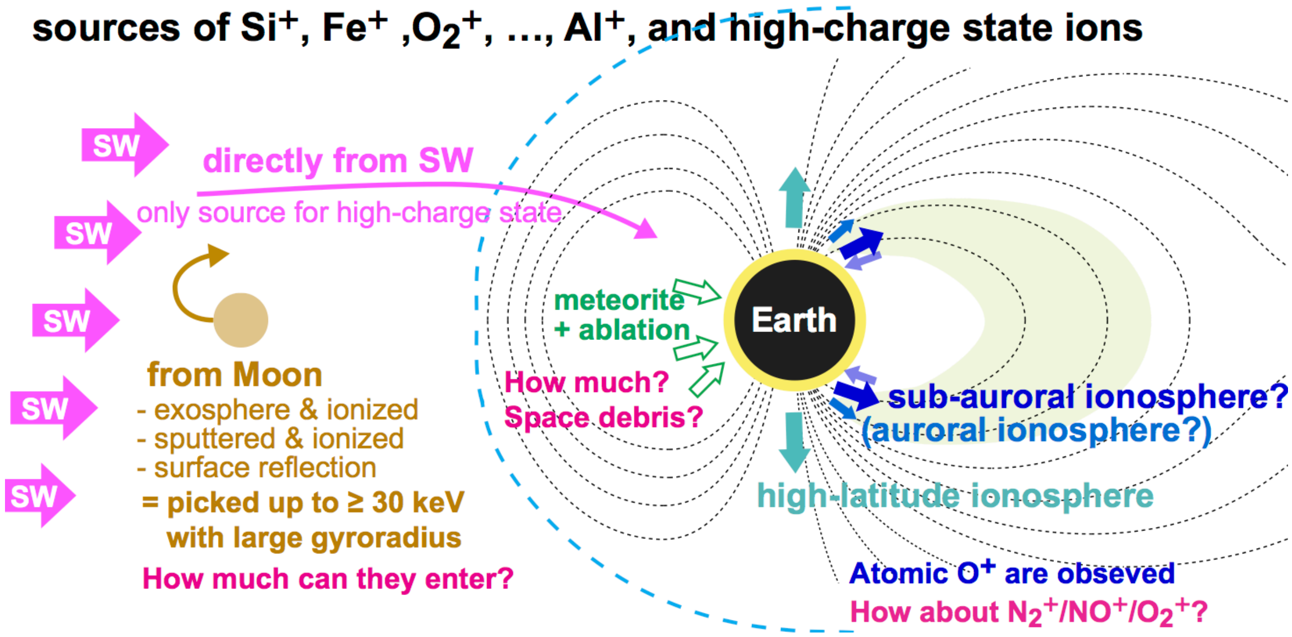

Figure 1.1. <metallic_source>: Illustration of possible sources of heavy molecular ions and metallic/silicate ions to the magnetosphere. Solid arrows show the pathway of these ions: (1) solar wind for high charge-state metallic/silicate ions (we call them simply "metallic ions" hereafter), (2a) dayside polar ionosphere (cusp and its vicinity) low charge-state heavy ions, (2b) night-to-morning auroral and sub-auroral ionosphere molecular ions, (3) mesospheric layer of heavy elements, which are ultimately provided by meteoric ablation, for metallic/silicate ions, and (4) The Moon surface and exosphere for low charge-state heavy ions. Note that the outflow mechanism from mesospheric layer means the atoms or ions must receive the same electromagnetic energization mechanisms as ionospheric ions.

As illustrated in Figure 1.1, there are four major sources of heavy ions in the Earth's magnetosphere with mass > 27 amu (here, we limit our discussions to mass < 100 amu, i.e., molecules, metallic atoms and their ionized forms). These sources are: (1) The solar wind; (2) The ionosphere (and thermosphere); (3) The mesospheric layer of heavy elements (hereafter, "metal layers”) for which the metallic ions have been detected by the sounding rocket since 1970; and (4) The surface and exosphere of the Moon. Here, the upper atmospheric sources are further divided into: (2a) the dayside polar ionosphere (cusp and its vicinity) low charge-state heavy ions, and (2b) night-to-morning auroral and sub-auroral ionosphere molecular ions. Unlike the molecular ions (N_2^+, NO^+ and O_2^+) that can be produced in the upper part of the ionosphere, metallic ions come from (3) mesospheric metal layers because of the low concentration of metallic atoms in the atmosphere otherwise.

The mesospheric metal layers are produced by mainly the ablation of cosmic dust (meteoroids), but a possible contribution from the ablation of space debris may increase in near the future because of the rapid increase of space debris and satellites. The ablation of these human-made objects during their atmospheric re-entry from space (in this paper termed as “ablation of space debris/waste”) results in the deposition of human-made metallic atoms to the mesosphere. Some common metals in spacecraft such as aluminum (Al) and lithium (Li) are very rare in the natural meteoroids, and may substantially contribute to the metallic layers, which in the end contribute to the magnetospheric metallic ions.

While the high charge-state ions and majority of the molecular ions come from (1) the solar wind and (2) the high-latitude ionosphere, respectively, the sources of the low charge-state metallic ions (including Si^+, and we simply refer them "metallic ions" hereafter) have not been identified. Two theoretically possible candidates are (3) the mesospheric metal layer and (4) the Moon, but both the sources have a too-low flux problem, and hence the possibility of coming from upstream solar wind is not dismissed. So far, not a single satellite observation has confirmed (or even indicated) the source and condition.

Here, we cannot dismiss the Moon as a source of metallic and molecular ions (Hilchenbach et al., 1993; Mall et al., 1998), as the result of sputtering at the surface (Saito et al., 2010) or photoionization in the thin exosphere (Halekas et al., 2015). When the Moon is upstream of the Earth (near the new Moon), these sputtered and photoionized ions are picked up by the solar wind plasma and gain up to twice the solar wind velocity (tens keV to hundred keV), with sufficiently large gyroradii to penetrate the magnetosphere. The problem is their flux. The initial result of Apollo did not show the upper lunar atmosphere containing metallic species, and only upper limits have been derived from ground-based observations (Stern, 1999). Although Kaguya found a signature of metallic ions at 100 km altitude around the Moon by in-situ measurement (Saito et al., 2010), and the Lunar Atmosphere and Dust Environment Explorer (LADEE) confirmed the thin exosphere with heavy species (Poppe et al., 2016b), the Moon-origin ion flux in the Earth' magnetosphere must be nearly impossible to detect after spreading over the large volume of the magnetosphere.

The very low ion flux also applies to the mesospheric source. Although the upward ion convection below the exobase is common and the escape energy is similar (about 20 eV for mass 30) between the metallic atoms (or ions) and molecules (or molecular ions), we expect the metallic ion flux at the exobase to be much lower than that of the molecular ions. The heavy mass (high escape energy) also makes it difficult for metallic ions to reach the ion energization region above the exobase where ions are accelerated to more than the escape energy. In the best case when any metallic ions are upflowing from the exobase, it must be in the polar region where the magnetic field line is near vertical and upflowing molecular ions with similar masses are observed (Yau et al., 1993). Note that this energization works for ions but not for neutrals. Since the density ratio of ion to neutral is small at the lower part of the ionosphere, drag of neutrals by the ions is not very effective to gain the escape energy at exobase, and therefore, we hereafter focus on ions but not neutrals.

These possible sources for low charge-state metallic ions, in the best case, may account only for a very low flux in the magnetosphere. On the other hand, such low flux that makes detection difficult, may enable these ions to work as a good marker of how these ions are transported from the source. Considering the completely different energy and energy/charge from the light ions or high charge-state ions (large gyroradius and high energy), the distribution and amount of these metallic ions give independent information on the entry of ions from the solar wind and from the ionosphere. Thus, these very minor ions work as good tracers.

1.2. Sciences related to each source

The source mechanism of metallic or heavy molecular ions (producing them and bringing them into the magnetosphere) are different between different sources. This opens up a possibility of classifying these ions in the magnetosphere in terms of dependency on the source condition (which also depends on the geomagnetic and solar wind conditions).

Together with the fact that they are very minor in the magnetosphere, quantitative measurements of these ions in the magnetosphere through each source at various places and various condition help revealing the source mechanisms of various source, and thus contribute to many science topics, as summarized in Table 1.1.

First, metallic (and heavy molecular) ions coming from the ionosphere carry essential information of the particle transport (by electromagnetic and electrostatic fields) in a collision-free frame from the exobase, particle transport in the ionosphere (and even in the mesosphere), ionization and chemistry in the ionosphere, and dynamics of the metal layers in the mesosphere and ionosphere. Here, ablation of the cosmic dust and near-Earth small bodies is considered as the source of the metal layers, and hence metallic ions of mesospheric and thermospheric origin are largely attributed to meteoroids.

In addition, the amount of escaping molecular ions gives extra information on the evolution of the Earth's atmosphere, although the main evolution is caused by the surface interaction including biological activity. Here, the evolution is not limited to the change in the total amount of oxygen, but also includes the oxidization rate (low CO_2/O_2 ratio and low N_2/O_2 ratio compared to Mars and Venus) and its fluctuation (just 5% change in 0.1 million scale often happen). The observed O^+ escape suggests a substantial contribution the latter (Yamauchi, 2019; Dandouras et al., 2018; 2016).

Table 1.1: Possible scientific contribution of heavy ion measurement

Ion source	Relevant science topics
(1) Solar wind (metallic ions)	Solar wind - magnetosphere interaction for different masses (with similar E/q) Ion entry into the magnetosphere
(2) Ionosphere (molecular ions)	Magnetosphere-Ionosphere coupling
	Energization processes at low altitude
	Ionospheric chemistry and dynamics for both dayside and nightside
	Atmospheric evolution (high latitude source only)
(3) Mesosphere / lower thermosphere (metallic ions)	Thermospheric dynamics
	Expansion of mesosphere and mesosphere-thermosphere-ionosphere coupling
	Ionospheric dynamics on both dayside and nightside
	Flux and deposition altitude of meteoroids
	Ablation and deposition of space debris with lower velocity than meteoroids
	On-orbit space debris fragmentation
(4) Moon surface and exosphere (low charge-state ions)	Solar wind - surface interaction different mass (with similar E/q)
	Micrometeorite-surface interaction
	Solar wind-magnetosphere interaction for pick-up heavy ions with different masses (with different E/q)

The low charge-state metallic ions in the magnetosphere can also be a possible indicator of space debris because, in the near future, we expect a substantial increase of human-made heavy atoms/ions (e.g., Lithium (Li) with mass 7, Aluminum (Al) with mass 27, Silicon (Si) with mass 28, Titanium (Ti) with mass 48, Iron (Fe) with mass 56, Nickel (Ni) with mass 59, Copper (Cu) with mass 64, and Germanium (Ge) with mass 73) deposited to the mesosphere during the ablation of space debris/waste as mentioned above. Among them, those relatively rare in the natural meteoroids may become detectable. These amounts, although they are small, might exceed the natural heavy ions in the near future if no new countermeasures against space debris are taken before the Kessler syndrome (Kessler and Cour-Palais, 1978) starts over a wide altitude range (which might have started at a limited altitude around 500-800 km in the worst-case estimate).

Table 1.2: Overview of heavy ion observations in the terrestrial magnetosphere.

Species	**Mass – Energy range**	**dedicated or not**	**Examples (Earth/Moon missions)**
C^+, N^+, or O^+ (m/q=14–16)	altogether (not distinguished)	dedicated*1	Cluster, VAP, MMS, etc
	each of C, N, O (<50 eV)	non-dedicated*2	DE-1, Akebono
	each (0.05–100 keV)	(missing)	
	each (>100 keV)	non-dedicated	AMPTE, Geotail
N_2^+, NO^+, or O_2^+ (m/q=28–32)	altogether (<50 eV)	dedicated	e-POP, ISIS-2
	altogether (10–100 keV)	dedicated	Arase
	altogether (>100 keV)	dedicated	CRRES, Polar
	each (<50 eV)	non-dedicated	DE-1, Akebono
	each (0.05–10 keV)	(missing)	
	altogether (0.05-30 keV)	non-dedicated	Cluster, Arase, MMS, etc
	each (30–100 keV)	non-dedicated	AMPTE
	each (>100 keV)	non-dedicated	AMPTE, Geotail
High charge-state heavy	each (>100 keV)	dedicated	Geotail, Wind, AMPTE, etc
Low charge-state metallic	each (>100 keV)	dedicated	Geotail, Wind
	each (cold)	dedicated@moon	LADEE
	each (0.01–30 keV)	dedicated@moon	Kaguya, LADEE

*1. Routine, *2 Non-routine,

Finally, the lunar origin low charge-state metallic ions give information of how the ions with very large gyroradii are picked up and enter the magnetosphere (through the bow shock, magnetosheath, and magnetopause). The entry processes and routes must be quite different from those of the high charge-state metallic ions originating from the solar wind and the solar energetic particles. To investigate them, we need to monitor the lunar origin ions near the Moon, which also allows us to further understand the sputter process on the lunar surface and striving process of the lunar exosphere for different solar wind conditions including its composition.

1.3. Lack of observations

Unfortunately, these heavy ions and atoms are largely unexplored in near-Earth space, and no terrestrial mission has had a dedicated instrument for the mass range covering up to the metallic ions at energy less than 100 keV, as summarized in Table 1.2. Past and recent works in detecting these molecular and metallic ions were carried out with non-dedicated instruments, such as plasma instruments designed to separate only four major species H^+, He^+, He^{++}, and O^+. Thus, the current understanding is at a preliminary level, and in the best case, only qualitative (even for the major four possible sources in Figure 1.1).

Due to such difficulties in extracting the heavy molecular and metallic ions from the data, past works on these very heavy ions in the magnetosphere are very sparse, spanning over many years by different missions. Furthermore, it is difficult to have event studies between different spacecraft, because the observation of metallic ions requires a long integration time (to accumulate adequate counting statistics for these low-abundant species), and active observations of wide mass ranges between different missions do not normally overlap within the same time period. With these reasons, obvious question remains such as whether any source is dominant over other sources, and if so, under what conditions. At the present, even the relative importance of ions of the Moon origin and Earth origin of different species is not known.

Any quantitative (statistically significant) measurements in the future will give important information on the transport of these very heavy ions in the magnetosphere: e.g., on the entry route, acceleration, and dependence on the external condition. On the other hand, during the best conditions such as large geomagnetic storms, some of the existing instruments on-board the past and current spacecraft listed in Table 1.2 actually separated N^+, O^+, N_2^+, NO^+ in observations, and even metallic ions (Fe^{n+}) after sufficient integration of the data over times. In other words, existing data from past and on-going missions are capable of detecting them, although the result is qualitative. Thus, it is very useful to make a list of all possible instruments that can potentially detect heavy molecular and atomic ions. Of course the limitation is severe. Even tracing the source of the observed metallic ions is often not possible from the available data except for some obvious cases such as near the interaction region with the solar wind.

In the list, we should include the Moon and solar wind missions that actually observed the Earth's magnetosphere, if the mission included a mass spectrometer better suited for these investigations than those onboard magnetospheric missions. One example is the Kaguya Moon mission that was inside the magnetotail or upstream of the magnetosphere for substantial time periods (Saito et al., 2010). Another example is the WIND mission that traversed the magnetotail for many hours. Non-mass resolved ion spectrometers with a wide energy range might also detect heavy ions when ions are picked up and flowing with the solar wind velocity, such as the observation of Venus downstream at the Sun-Earth Lagrange point (Grünwaldt et al., 1997). Ideally, Earth-flybys of planetary missions should also be included because they normally carry mass spectrometers with much better mass resolution at energies of 0.01–100 keV than those on magnetospheric missions, but it is not very practical to include them because very limited data are taken by only Cassini and STEREO.

Since the molecular and low charge-state metallic ions were not a prime observation target of the all past and current magnetospheric missions listed in Table 1.2, software tools and methodology to extract information about these heavy ions are normally not well documented or maintained. Thus, there is a risk of losing the relevant data (including the case that the data becoming unreadable with modern computer systems) even for data that are used as examples of the reported metallic or heavy molecular ions. Therefore, collection of the capable missions and instruments requires information of software availability. This is very difficult for terminated missions if not impossible.

It would be also useful to combine different types of observations, e.g., solar wind monitor, Moon data, satellite data in both the magnetosphere and ionosphere, and ground-based (lidar) data. We present several examples that can actually update the present knowledge about the heavy ion entry into the magnetosphere.

Finally, we discuss a possible "ideal" and "compromised" suite of observations, including feasible improvements of the instruments (including software). Such a suite helps planning the future observation by many capable missions (such as onboard the Space Safety/Earth Observation/Lunar Exploration missions) as well as a dedicated mission. Here, we aim to answer fundamental questions that arise for different conditions, such as:

- What is the relative importance of the terrestrial (ionosphere or mesosphere) source and the lunar source for the low charge-state heavy ions in the magnetosphere?
- How much of the observed heavy ions emanate from the aurora/sub-auroral ionosphere compared to the cusp and its vicinity?
- Is it possible to quantitatively evaluate the present and future contamination by space debris?

The review has the following sections.

2. The scientific importance of molecular and metallic ions

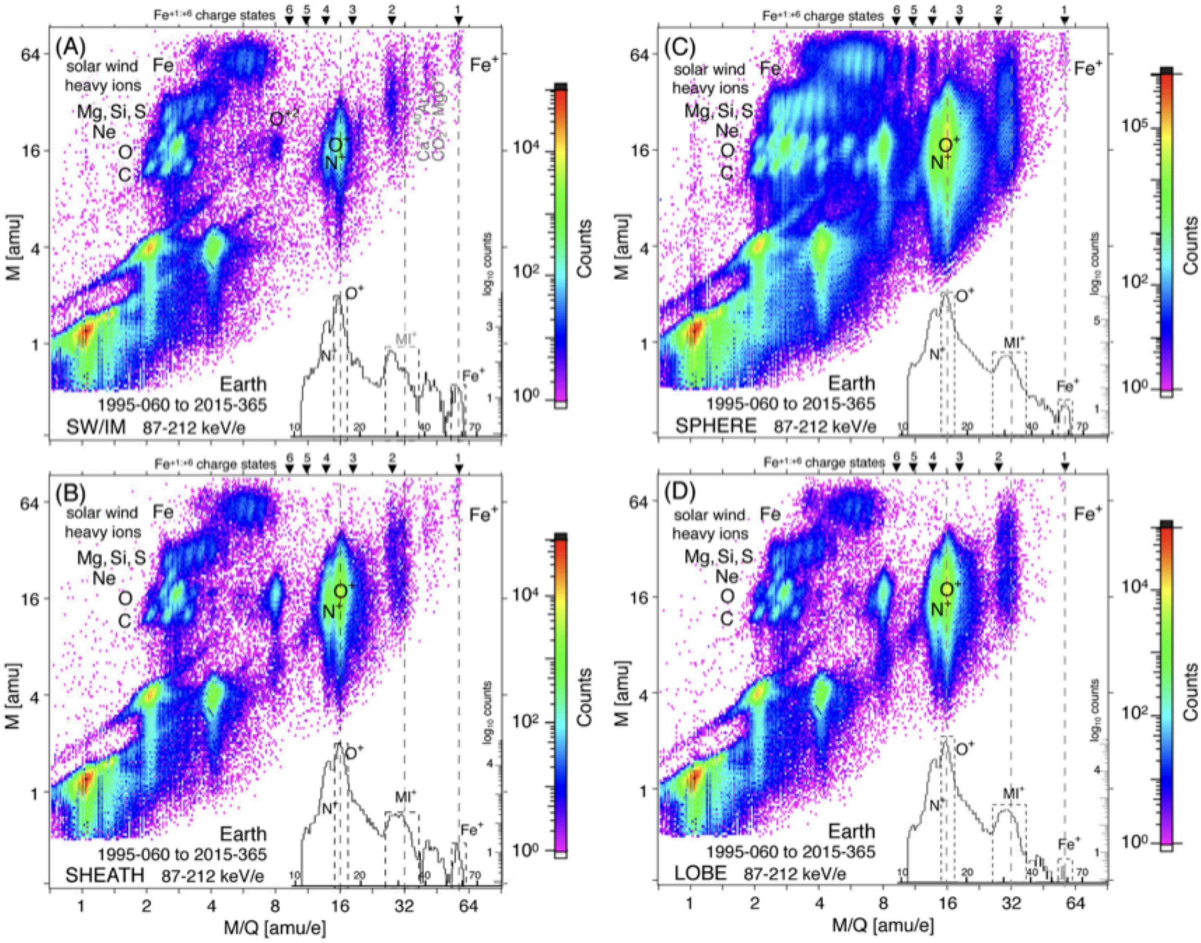

<<Fig 2.1: Steve_100-200keV/e Ions@Earth_a>>: Average 100-200 keV/e ion composition in and near Earth's Magnetosphere. Mass – mass-per-charge (m – m/q) diagrams are shown for 4 different regions (see Christon et al., 2017 for definition): (a) the upstream region (SW/IM), (b) the magnetosheath (SHEATH), (c) the magnetosphere (SHERE), and (d) lobe, respectively. The counts found in the upper left half of each panel correspond to high charge-state ion of the solar wind origin. At lower right part of each panel, histogram for m/q is also shown for low charge-state heavy ions. Here, m/q is obtained from the combination of electrostatic analysis (giving energy-per-charge E/q) and time-of-flight TOF (giving velocity), and m is obtained from the combination of pulse height analysis PHAs (giving total energy E) and TOF. The measurement accuracy is the best for E/q and the worst for E, resulting in more spread in the m direction than in the m/q direction.

Figure 2.1 shows Geotail/STICS statistics of the count distributions over 20 years, ordered by mass (m) and mass-per-charge (m/q) in four different regions (Christon et al., 2017). In the magnetosphere (Figure 2.1c: SPHERE), low charge-state metallic ions (Fe^{+}) are seen

as (marked as 1 at the top of the panel) isolated from high charge-state Fe ions, in addition to heavy molecular ions (MI+) at around m/q~30.

2.1 Importance and present knowledge of the solar wind source (high charge-state metallic ions)

The solar wind is the obvious source of high charge-state metallic ions in the terrestrial magnetosphere because the high temperature of the solar corona provides for multiple high charge-state ionizations of all elements. During the travel or even at the corona, ions are often energized to more than 1 MeV, forming the solar energetic particles (SEPs), and these ions have sufficiently high energy to be detected by mass spectrometers of energetic particles, as shown in Figure 2.1. Note that the term "solar wind" does not necessarily mean that all these elements are flowing with the solar wind proton flow. Some solar flare origin energetic ions take different path such as along the IMF, while some are accelerated at the interplanetary shock to reach the energy detectable by the Geotail/STICS instrument (Figure 2.1). Even atoms and of interstellar origin, including galactic cosmic rays, are also present in the solar wind, although in much smaller abundances than those of solar origin.

Figure 2.1 also shows existence of Fe^{+} and Fe^{++}, isolated from high charge-state Fe ions, indicating upstream source of atomic metals, i.e., other than the solar corona. The obvious candidate is the Moon when it is upstream, as discussed in Sect. 2.4. Such low charge-state metallic ions have quite different gyroradius from the solar wind protons. Considering it is difficult to provide from the ionosphere means that ions, these metallic ions work as the tracer as mentioned in Sect. 1.1, i.e., one can gain a clue in the pathway of these ions to the Earth by knowing the distribution and amount of these metallic ions, and by comparing with those of light ions. Furthermore, the distribution of the low charge-state metallic ions provides the effectiveness of their energization mechanisms across bow shock and magnetospheric boundaries, and even entry mechanisms to the magnetosphere because any electrostatic acceleration (e.g., at the bow shock) gives different acceleration efficiency from light ions even for the same mass per charge (m/q).

A major challenge is that, compared to good-quality observations and datasets in the solar wind for both the solar wind energy (generally < 100 keV and < 2 keV/q) and the SEP energy (up to 100 MeV), magnetospheric observations are sparse and are typically limited to high energy for high charge-state ions.

2.1.1. Observations in the solar wind

The observations of heavy ions in the solar wind date back to the first space missions, such as the Vela missions (e.g., Hundhausen et al., 1967) and the Apollo Moon missions in the 1960s. The satellites in Vela series were equipped with energy per charge instruments from which composition could be derived. Heavy ions, in the form of high charge-state oxygen, were reported by Bame et al. (1968a,b) using observations from the Vela 3 satellite. Subsequent versions of the Vela satellites carried more advanced instruments, and even heavier ions like silicon (Si) and Iron (Fe) and possibly sulphur (S) of various charge states were reported by Bame et al (1970).

Composition of the solar wind was also inferred from depositions in the aluminium foils deployed on the Moon surface by astronauts of the Apollo 11-16 missions (Geiss et al., 2004) and from analysis of sample returns for updated information (e.g., Reisenfeld et al., 2007; Jurewicz et al., 2007; Heber et al., 2021)

In the late 1980s and early 1990s, space missions fitted for solar wind observation such as ISEE-3, Ulysses, SOHO, ACE, and WIND, measured the solar wind compositions (e.g., Gloeckler et al., 1992; Geiss et al., 1995; von Steiger et al., 2000; von Steiger and Zurbuchen 2002; Reisenfeld et al., 2007). The new generation of instrumentation, particularly particle spectrometers with electrostatic deflectors and time-of-flight analyzers, enabled a more comprehensive mapping of the solar wind composition. For example, SOHO CELIAS/MTOF instrument (Hovestadt et al., 1995) identified and classified elements where no coronal spectroscopic measurements are possible (Wurz, 2005).

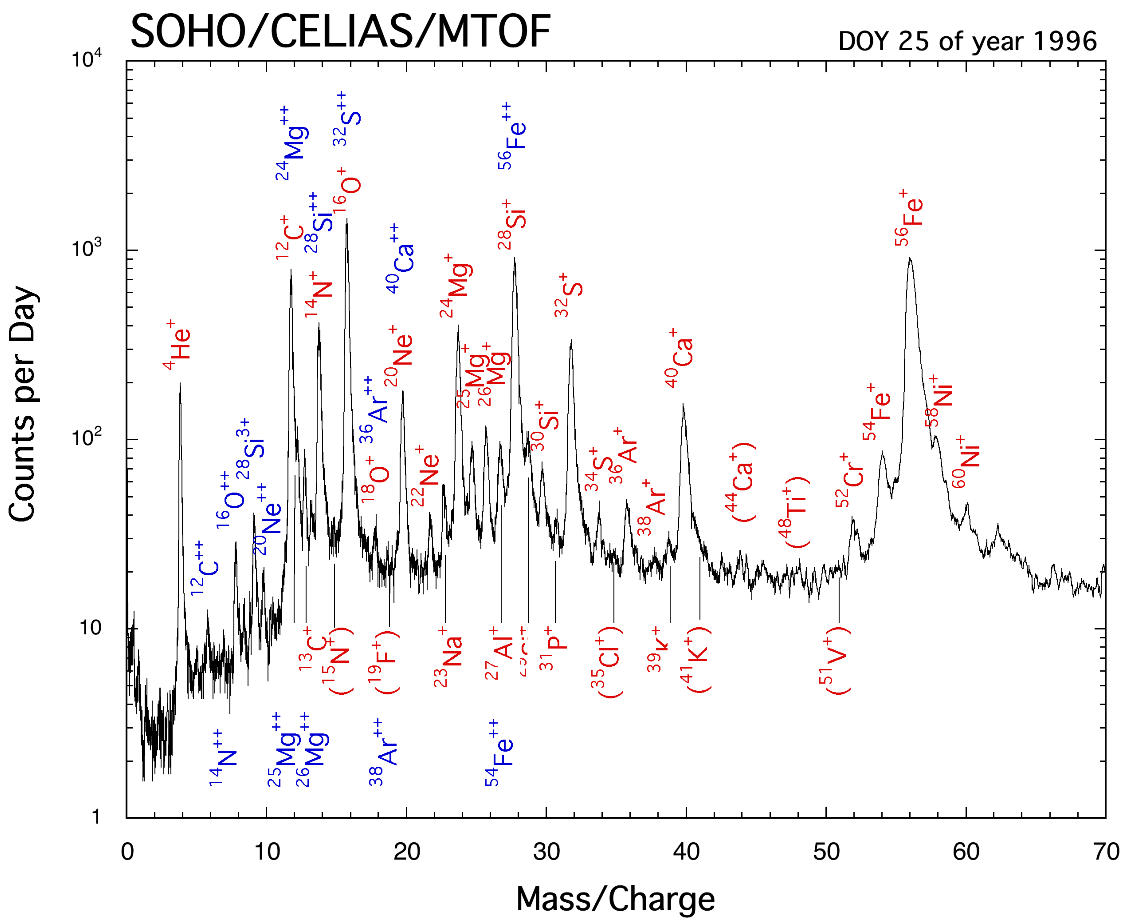

Fig 2.2: SOHO CELIAS/MTOF data of mass spectrum (Wurz, 2005). The charge state given in the labels refers to the charge inside the MTOF instrument (it not referring to the charge state in the solar wind), and so is the horizontal axis “Mass/Charge”. Up to two main ion contributors are indicated at each peak. Labels in parenthesis indicate that the identification of that ion is highly uncertain.

Figure 2.2 shows a mass spectrum observed by SOHO/CELIAS with its MTOF sensor. The figure shows the variety of atomic constituents in the solar wind over a wide energy range. Table 2.1 shows an overview of metallic (atomic number $Z \geq 10$) ion species detected in the solar wind, and their abundance relative to that of oxygen (oxygen itself constitutes about 0.05–0.15% of all ions in the solar wind (e.g., Bame et al., 1975, von Steiger et al., 2010). The table even includes the solar surface data obtained by optical methods. Because many processes in the solar atmosphere, chromosphere, and corona, and the eventual formation of the solar wind depend on m/q, the composition of the photosphere and the solar wind differ by factors of 2 to 4, depending on slow and fast solar wind conditions.

Table 2.1: Relative abundance compared to Oxygen element

Element	Photosphere (*1)	Meteoric (*1)	SW: Inter-stream (*2)	SW: Coronal-hole (*2)	SEP-derived Corona (*3)
H	1500	–	1900	820	–
Li	<0.001	<0.001	–	–	–
O	1	(*4)	1	1	1
Na	0.003	0.003	–	–	0.012
Mg	0.056	0.056	0.16	0.083	0.192
Al	0.004	0.005	–	–	0.015
Si	0.052	0.054	0.18	0.054	0.176
P	<0.001	<0.001	–	–	0.001
S	0.032	0.023	–	–	0.043
Cl	<0.001	<0.001	–	–	<0.001
K	<0.001	<0.001	–	–	0.001
Ca	0.003	0.003	–	–	0.014
Ti	<0.001	<0.001	–	–	0.001
Cr	0.001	0.001	–	–	0.003
Mn	<0.001	<0.001	–	–	0.001
Fe	0.047	0.047	0.12 - 0.19	0.057	0.224
Ni	0.003	0.003	–	–	0.008
Cu	<0.001	<0.001	–	–	<0.001
Zn	<0.001	<0.001	–	–	<0.001

*1: Photospheric and meteoritic abundances are from a compilation by Anders and Grevesse (1989) and Grevesse and Sauval (1998)
*2: Solar wind abundances (SOHO/CELIAS) are taken from von Steiger (1995)
*3: SEP-derived coronal abundances (SOHO/CELIAS) are taken from Breneman and Stone (1985).
*4: Assumed as the same as photosphere

2.1.2. Observations in the magnetosphere

Observations of metallic ions in the magnetosphere are very sparse because of their high mass (long TOF and large gyrordius compared to H^+) and extremely low flux. This applies to ions of both the solar wind origin (high charge-state) and the Earth/Moon origin (low charge-state). Except planetary missions, only energetic particle detectors (> 100 keV that give short enough time-of-flight to obtain the velocity) are capable of detecting the metallic ions, such as STICS instruments on board Geotail and Wind. Ion mass spectrometers for lower energies that were capable of identifying molecular ions (e.g., DE-1/EICS, Akebono/SMS) did not routinely sample the full mass range. One notable exception for the magnetospheric observation was the Kaguya Moon mission that could detect metallic ions, although the detection of the metallic ions was limited to those from the Moon surface, but not from the near-Earth region.

For the solar wind source, its contribution to metallic ions in the magnetosphere varies with the solar activity and with the solar cycle (e.g., Mitchell et al., 1983, Reames, 1995, von Steiger et al., 1997, Zurbuchen et al., 2002, Gilbert et al., 2012, Zurbuchen et al., 2016; Wurz, 2005), as well as connectivity to the Sun, e.g., slow vs. fast solar wind (e.g., Feldman et al., 2005). Nevertheless, traces of these heavy ions are almost always present in the magnetosphere.

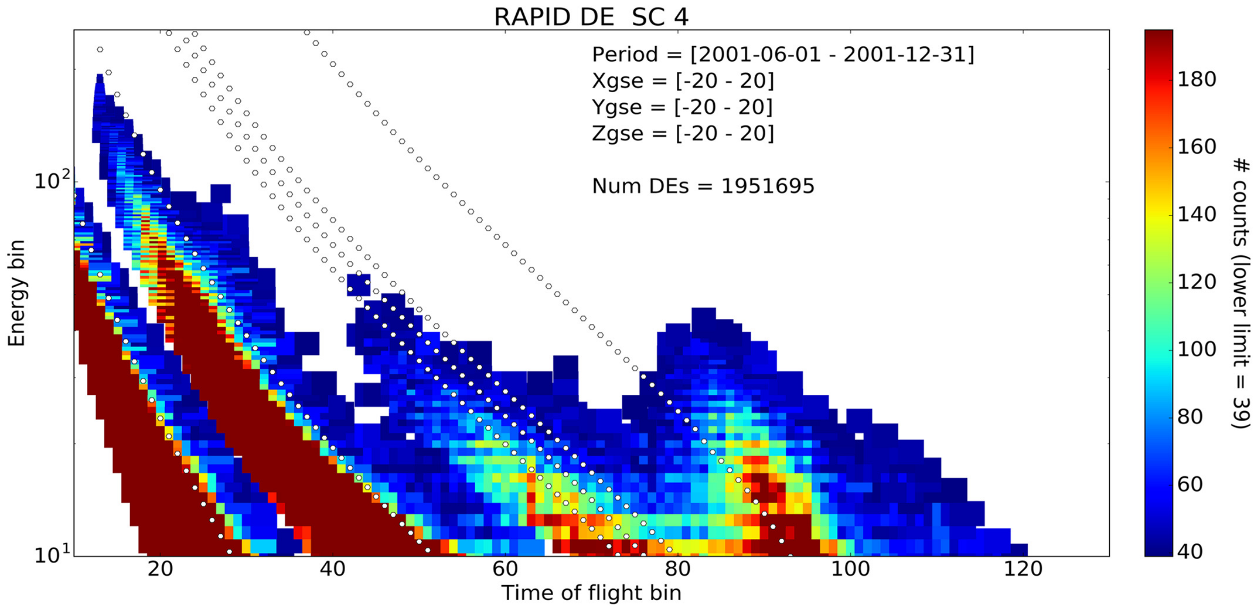

Figure 2.3: Composition measurement by Cluster/RAPID over 18 years (Haaland et al., 2020). Energy for Fe channel (no distinction of charge state) is > 400 keV, which covers higher energies than Figure 1 for Fe+, as well as the same energy range as solar wind F+≥7.

Using AMPTE/CHEM data, Gloeckler et al. (1985) and Gloeckler and Hamilton (1987) reported that the relative abundances of the solar wind species in the magnetosphere, including high charge-state Fe ions, were very similar to the corresponding solar wind abundances, indicating that the solar wind enters the magnetosphere without significant mass discrimination. The M – M/Q diagram shown in Figure 2.1.1c (Christon et al., 1994; 2017) clearly show that high charge-state solar wind ions of Fe, Mg, Si, C, N, and O exist in the magnetosphere. Examining the iron charge states close to geosynchronous orbit measured by CRRES, Grande et al. (1996) showed a dramatic change of the dominant charge state from +9 to +16 during a large magnetic storm, again suggesting that the charge states measured in the outer magnetosphere reflect the changes of the charge state in the solar wind. A comparison of the iron charge states measured by ACE/SWICS in the solar wind and by POLAR in the cusp/cleft region (Perry et al., 2000) showed that the solar wind material direct enters during southward IMF time periods. Haaland et al. (2020, 2021) identified Fe using the RAPID instrument on Cluster (which does not measure charge state), as shown in Figure 2.3. They find that the abundance varies with solar activity, again indicating a solar wind source. Thus, the charge state measurements clearly showed that the solar wind is the dominant source of energetic iron in the magnetosphere.

On the other hand, Geotail/STICS observation includes low charge-state metallic ions of m/q>35, such as Fe^+, as shown in Figure 2.1. Possible sources of metals and low charge-state metallic ions are the Earth's upper atmosphere, the Moon, and meteoroids, as illustrated in Figure 1.1. This is a completely unexplored field because of the lack of suitable instruments, even considering the very marginal capability for these measurements. Therefore, when considering the magnetospheric heavy ions, we need to know the charge state information even for metallic ions, although almost all signals are of high charge-state of the solar wind origin.

2.2 Importance and present knowledge of the ionospheric source (molecular ions)

Molecular ions such as N_2^+, NO^+, and O_2^+ were found together with O^+ ions in the topside ionosphere in the 1970's (Hoffman et al., 1974) and at high altitude (above 2 R_E altitude) in 1980's (e.g., Chapell et al., 1982; Craven et al., 1985). Unlike the many atomic ion species in the magnetosphere (H, He, N, and O), which are partly supplied from the solar wind, molecular ions cannot be of solar wind origin. In fact, Akebono SMS instrument found upflowing molecular ions. One peculiar feature is that the fluxes of molecular ions (N_2^+, NO^+, and O_2^+) in the magnetosphere, for both the upflowing ions coming from the ionosphere and trapped one in the inner magnetosphere, increase more drastically than atomic ions (O^+) during strong geomagnetic storms (Yau et al., 1993; Craven et al., 1985; Klecker et al., 1986; Hamilton et al., 1988). The correlation between the magnetospheric activity (measured by geomagnetic indices) and the ion flux of ionospheric origin in the outer magnetosphere had been recognized already in the 1970's (Geiss et al., 1978).

The drastic increase of molecular ion flux during strong magnetic storms in the inner magnetosphere (L = 2–8) is seen over a wide energy range by the Arase satellite (Seki et al., 2019; Takada et al., 2021), with the MEPI and LEPI instruments, by the velocity filter effect which are capable of quantitatively separating heavy molecular ions (in the mass group of 28-32) from atomic ions (Yokota et al., 2017; Asamura et al. 2018). Therefore, these low-energy O^+ and O_2^+ ions in the outer magnetosphere must be, together with low energy He^+, considered to originate from the ionosphere (Young et al., 1977; Geiss et al., 1978).

Since geomagnetic storms increase the energy deposition (in both forms of electromagnetic energy flux and particle precipitation) from space to the ionosphere and to the coupled magnetosphere-ionosphere system, we expect enhanced upward transport in the ionosphere (ionospheric dynamics), enhanced production of ions in the ionosphere (ionospheric chemistry), and/or enhanced pre-energization before reaching the main energization region (particle dynamics above the ionosphere), as summarized in Sects 2.2.1, 2.2.2, 2.2.3, respectively. These effects are more drastic for molecular ions than atomic ions because the threshold energy input to makes the molecular ions outflowing is higher than such energy for the atomic ions. In addition, such enhancement of the molecular ion outflow may influence the evolution of the life more than atomic ions, as are described in Sect 2.2.4.

Although these heavy molecular ions are of ionospheric origin (lunar source is negligibly small, see Sect. 2.4), the source location is not completely understood, partly because of the lower fluxes compared with atomic ions and partly because of the difference in the ionospheric processes between the molecular ions and atomic ions, as described in Sect. 2.2.3. For heavy atomic ions (O^+), there are two major outflow regions: one is the dayside polar region (cusp and its downstream region) and the other is auroral region where auroral acceleration is taking place (Moore et al., 1999, Peterson et al., 2008). On the other hand, the Akebono satellite at more than 2 R_E geocentric distance found intense fluxes of upflowing heavy molecular ion predominantly on the dayside (Yau et al., 1993), while much less flux or zero flux of the molecular ions were detected in the nightside at auroral latitudes in the observation where the O^+ upflow are observed.

Note that this O^+-O_2^+ difference can still be attributed to the orbit and data sampling coverage because we expect an equatorward shift of heavier species with respect to light species in the nightside, where the magnetospheric convection is predominantly equatorward during geomagnetic storm conditions, the condition when the molecular ion upflow from the ionosphere is enhanced. Under any convection, heavier ions with the same energy as the lighter ions are carried further downstream by the magnetospheric convection compared with the lighter ions. Such mass dependency is actually observed by Freja as the difference between the H^+ injection and O^+ injection in the opposite hemisphere (Hultqvist, 2002; Yamauchi et al., 2005). Thus, we expect that the upflowing molecular ions reach lower latitudes (e.g., the outer radiation belt) than atomic ions during the upflow process, such that they travel beyond the latitude range of SMS operations at Akebono altitude.

The coverage problem is not limited to Akebono observation because the ion instruments on board the magnetospheric satellites are often turned off at the sub-auroral latitudes to avoid the damage from the radiation belts, potentially missing the molecular ions flowing in such low latitudes. Since the energization is expected to be quite different between different latitudes, the outflowing path and/or the pre-energization process may be different between the molecular ions and atomic ions.

It is yet unknown whether the ionospheric molecular ions outflow from the topside ionosphere (or exobase) in the nightside auroral/sub-auroral region, and if so, how much and in what condition do they populate the magnetosphere. These questions apply even to the dayside high-latitude route. By comparing these results, we can gain more information on the ionospheric processes as well as the energization processes above the ionosphere.

Molecular ions of ionospheric origin can possibly be observed deep in the magnetotail (> 50 R_E). Although no mass spectrometer for the magnetotail observation is capable of separating O_2^+ ions from O^+ ions at energy less than 100 keV (Kaguya Moon mission with a capable instrument did not looking at the magnetotail flow), an ion energy spectrometer with large geometric factor may in principle detect it at higher energy than atomic ions (O^+) because we expect the same velocity for all species. However, in reality the energy spread of O^+ is wide and O^+ energy can even be 30 times as the H^+ energy. For example, the Acceleration, Reconnection, Turbulence, and Electrodynamics of the Moon's

Interaction with the Sun (ARTEMIS) spacecraft detected an anti-sunward high ion flux at about the concurrent proton velocity, i.e., at nearly 25 times the energy as the main anti-sunward flux at the lunar distance in the magnetotail during geomagnetically disturbed times (Poppe et al., 2016a), which was initially interpreted as potentially containing molecular species (N_2^+, NO^+, and O_2^+, approximately masses m/q 28–32), but majority of this high-energy flux must be atomic ions (O^+), if not all, for this event.

2.2.1 The importance of the ionospheric and thermospheric dynamics and energization (upflow) for the molecular ions in the magnetosphere

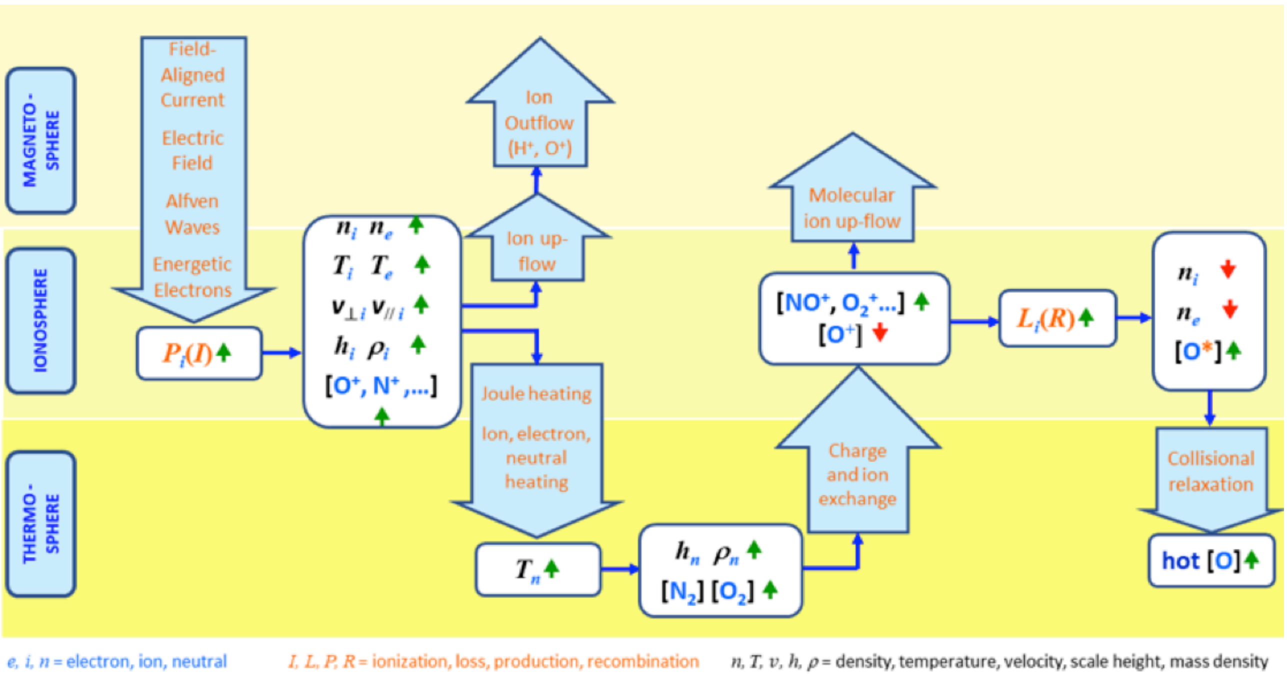

Figure 2.4 \ref{fig22_Yau_outflow_schematic.png}: A schematic illustration of the underlying physical processes of ion upflow and their importance in ionosphere-thermosphere dynamics, including (a) the energy deposition in the auroral ionosphere due to field-aligned currents, convection electric fields, Alfvén waves, and auroral electron precipitation; (b) increase in ion production *Pi* by electron impact ionization I, increases in ion and electron densities and temperatures (n_i, n_e, T_i, T_e), ion convection and parallel velocities ($v_{i\perp}$, $v_{i//}$), plasma scale height and mass density (h_i, ρ_i), and O^+, N_2^+, and N^+ ion composition; (c) ion upflows, Joule heating, and neutral heating; (d) resulting increase in the neutral scale height and mass density, N_2 and O densities, and N_2/O density ratio; (e) increased production of molecular N_2^+, O_2^+, and NO^+ ions in the F-region and above, due to increase in auroral electron impact ionization of N_2 and O_2 and in their charge-exchange and ion-exchange with the dominant O^+ ion.

Figure 2.4 illustrates schematically the underlying physical processes of ion upflow and their importance in the ionosphere-thermosphere dynamics in the context of magnetosphere-ionosphere-thermosphere (MIT) coupling, including the energy deposition in the auroral ionosphere associated with field-aligned currents, convection electric fields, Alfven waves, and auroral electron precipitation (both energetic and soft electrons). Such energy deposition causes an increase in ion production P_i due to electron impact ionization I, and subsequently increases in ion and electron densities and temperatures (n_i, n_e, T_i, T_e), ion convection and parallel velocities ($v_{i\perp}$, $v_{i//}$), plasma scale height and density (h_i, ρ_i), and changes in the O^+, N_2^+ and N^+ ion composition.

The resulting plasma pressure gradients and ion convection velocities give rise to ion upflows and Joule heating, respectively, as well as neutral heating due to ion-neutral collisions. The latter in turn gives rise to an increase in the neutral scale height and mass density, and a corresponding increase in both N_2 and O densities at a given altitude, with the N_2 density increasing at a faster rate relative to O with increasing altitude, so that the increase in the N_2/O density ratio is also largest at the highest altitude.

This in turn leads to an increased production of molecular N_2^+, O_2^+, and NO^+ ions in the ionospheric F-region and above, due to the combination of (a) auroral electron impact ionization of N_2 and O_2, both at increased densities, (b) charge-exchange of both N_2 and O_2 with the dominant O^+ ion, giving rise to N_2^+ and O_2^+, respectively, and (c) ion-exchange reaction between N_2 and O^+, giving rise to NO^+. While contributing the significant enhancement of ion upflow, these molecular ions contribute to the reduction of the overall electron density due to their rapid dissociative recombination rate in the F-region, as explained in details below (see also Sydorenko et al., 2016), and also contribute the production of hot oxygen and nitrogen atoms in the thermosphere (see e.g., Richards et al., 1994).

2.2.2 The importance on the ionospheric chemistry (source and re-combination during upflow)

In terms of their influence on the ion composition in the Earth's ionosphere, the two most important types of chemical processes are ion-neutral charge exchange and recombination reactions. The lower thermosphere is dominated by molecular oxygen (O_2) and nitrogen (N_2), and the upper thermosphere is dominated by atomic oxygen (O) below the H-O crossover height and by atomic hydrogen (H) above, respectively. Correspondingly, the E-region ionosphere is dominated by molecular NO^+ and O_2^+ ions (Del Pozo et al., 1997; Grebowsky and Bilitza, 2000), while the F-region and the upper ionosphere up to the crossover height is dominated by atomic oxygen ions. Above the crossover height, the topside ionosphere and beyond is dominated by atomic hydrogen ions (proton, H^+), although the hydrogen exosphere still extends to more than 10 R_E (e.g., Kameda et al., 2017) in the proto-dominated region.

The charge exchange reactions of highest importance to the F-region and topside ionosphere are therefore those involving O^+ and H^+ ions, respectively, such as:

$$H^+ + O \rightarrow O^+ + H \qquad k = 3.8 \times 10^{-10}\ \text{cm}^3\ \text{s}^{-1}$$

$$O^+ + N_2 \rightarrow NO^+ + N \qquad k = 1.2 \times 10^{-12}\ \text{cm}^3\ \text{s}^{-1}$$

$$O^+ + O_2 \rightarrow O_2^+ + O \qquad k = 2.1 \times 10^{-11}\ \text{cm}^3\ \text{s}^{-1}$$

$$O^+ + H \rightarrow H^+ + O \qquad k = 6.4 \times 10^{-10}\ \text{cm}^3\ \text{s}^{-1}$$

where *k* denotes the best accepted value of the room-temperature rate coefficient in the literature in each case.

Dissociative recombination processes often dominate the ion composition (abundance) of a planetary ionosphere. In the Earth's ionosphere, the dissociative recombination of the molecular O_2^+, N_2^+, and NO^+ ions is particularly important. While this reaction produces oxygen atoms and/or nitrogen atoms, some of the produced atoms are meta-stable excited electronic states, which ultimately lead to the formation of airglow and the aurora, and some atoms are 'hot atoms' in the ground electronic state with excess kinetic energy that ultimately contribute to heating of the thermosphere via their collisional relaxation with the ambient oxygen atoms. In the case of the O_2^+, the dissociative recombination process can proceed in as many as 5 branches:

$$O_2^+\left(X\ ^2\Pi_g\right) + e \rightarrow O(^3P) + O(^3P) + [6.99\ \text{eV}] \quad ; \quad p = 0.22$$

$$\rightarrow O(^3P) + O(^1D) + [5.02\ \text{eV}] \quad ; \quad p = 0.42$$

$$\rightarrow \quad O(^1D) + O(^1D) + [3.06\,eV] \quad ; \quad p = 0.31$$

$$\rightarrow \quad O(^3P) + O(^1S) + [2.80\,eV] \quad ; \quad p < 0.01$$

$$\rightarrow \quad O(^1D) + O(^1S) + [0.83\,eV] \quad ; \quad p = 0.05$$

$$\alpha = 2.0 \times 10^{-7}\,(300/T_e[K])^{0.7}\ cm^3\,s^{-1}\ (T_e < 1200\ K);$$

$$\alpha = 0.74 \times 10^{-7}\,(1200/T_e[K])^{0.56}\ cm^3\,s^{-1}\ (T_e > 1200\ K)$$

where the parameter p denotes the branching ratio, i.e., the fraction going to each branch, the value listed in the square bracket is the excess kinetic energy, and α is the dissociative recombination rate coefficient.

Similarly, in the case of molecular nitrogen (N_2^+) and nitric oxide (NO^+) ions:

$$N_2^+\left(X\ {}^2\Sigma_g^+\right) + e \quad \rightarrow \quad N(^2D) + N(^2D) + [1.04\,eV]$$

$$\alpha = 2.2 \times 10^{-7}\,(300/T_e[K])^{0.39}\ cm^3\,s^{-1}$$

$$NO^+\left(X\ {}^2\Pi\right) + e \quad \rightarrow \quad O(^3P) + N(^4S) + [2.75\,eV] \quad ; \quad p = 0.22$$

$$\rightarrow \quad O(^3P) + N(^2D) + [0.38\,eV] \quad ; \quad p = 0.78$$

$$\alpha = 4.0 \times 10^{-7}\,(300/T_e[K])^{0.5}\ cm^3\,s^{-1}$$

where the rate coefficient of dissociative recombination α decreases slowly with increasing temperature. In the case of atomic ions, recombination with electrons has to occur via photon emission, and is quite inefficient. For example, the radiation recombination rate coefficient for the radiative recombination of Fe^+ with an electron is $8x10^{-12}\cdot(300/T)^{0.51}$ $cm^3\,s^{-1}$ (Nahar et al., 1997), which is about 5 orders of magnitude slower than for the typical dissociative recombination reaction of a molecular ion.

In the auroral ionosphere, the dominant ion production process for atomic O^+ ion is the collisional ionization of neutral atomic oxygen (O) by precipitating auroral electrons, followed by the dissociative ionization of molecular oxygen (O_2). For atomic N^+, the dominant ion production process is the corresponding dissociative ionization of molecular nitrogen (N_2). Likewise, the dominant ion production process for molecular oxygen and nitrogen ions (O_2^+ and N_2^+) is the electron impact ionization of molecular O_2 and N_2, respectively. Following the treatment of Jones (1974, equation 4.2) the ion production ratio γ between N^+ and O^+ may be written semi-empirically as (see also Yau et al. 1992):

(2.1) $$\gamma = \frac{P_\mathrm{N}}{P_\mathrm{O}} = \frac{[\mathrm{N_2}]}{2.46[\mathrm{O}]+1.46[\mathrm{N_2}]}$$

where P_N and P_O are the N^+ and O^+ ion production rates, respectively, and [X] denotes the density of neutral species X.

Thus, in the F-region (above ~150 km), where $[O_2] << [O]$, the production rate ratio γ is directly proportional to the local neutral molecular nitrogen to atomic oxygen density ratio $[N_2]/[O]$. During a large magnetic storm and an extended period of auroral substorms, the neutral N_2 density at auroral latitudes substantially increases (i.e., atmospheric scale height increases) due to the thermospheric heating. For example, based on the MSIS model, γ typically increases by a factor of 2–5 from its quiet-time value (Ap index < 5) in the 300–500 km altitude region during disturbed times (Ap ~ 100).

All these reactions imply that the combination of (a) auroral electron impact ionization and dissociative ionization) of molecular N_2 and O_2 and (b) the chemistry of ion-neutral charge-exchange and of dissociative recombination results in a significant increase in the N_2 to O density ratio in the F-region and topside auroral ionosphere during the geomagnetic storms and extended periods of the auroral substorms. Consequently, the molecular ion density increases in such geomagnetic conditions, resulting in the upflow of the molecular ions the reduction in overall plasma density in the topside ionosphere.

2.2.3 Importance of the transport above exobase (above about 500 km)

Except for H^+ and to a lesser extent He^+, all ions need extra energy to reach the magnetosphere from the ionosphere. For heavy atomic ions such as O^+ and N^+, a substantial portion of the upward moving ions is bounded by gravitation and returns to the ionosphere (Yamauchi, 2019, and references therein; Dandouras, 2021) before acquiring sufficient further energy in the main energization region at higher altitudes to overcome gravity and reach the distant magnetosphere (Delcourt et al., 1993; Yau and André, 1997; Nilsson et al., 2008; Gronoff et al., 2020).

Table 2.2 summarizes the escape energy needed for various ions to reach various altitudes along a vertically oriented geomagnetic field from the ground and from 500 km altitude (the exobase near solar maximum), respectively, with the latter value given inside the parenthesis. For example, O_2^+ ions at 500 km altitude flowing along such a field line needs a minimum of 3.4 eV to reach 2000 km and a minimum of 5.2 eV to reach 3000 km (actual required energy depends on how much are distributed to the perpendicular directions), while half the energy is required for the O^+ atomic ions (1.7 eV for reaching 2000 km and 2.6 eV for 3000 km).

The main energization includes both the electromagnetic wave acceleration (including mirror acceleration) (Gorney et al., 1982, Yau et al., 1983; Lundin and Guglielmi, 2006) and electrostatic acceleration (including centrifugal acceleration (Cladis, 1986)), and these main energization regions vary with time and with locations (latitudes and MLT), with the lowest altitude about 2000 – 4000 km altitudes.

Table 2.2: Escape velocity (km/s) and energy (eV) for different species and minimum energy to reach from 500 km altitude (inside parenthesis)

height	escape velocity	O	N_2	Fe
500 km	**10.8 km/s**	**9.7 eV (0 eV)**	**17.0 eV (0 eV)**	**34 eV (0 eV)**
1360 km (e-Pop)	10.2 km/s	8.6 eV (1.1 eV)	15.1 eV (1.9 eV)	30 eV (3.8 eV)
1500 km	10.1 km/s	8.5 eV (1.2 eV)	14.8 eV (2.2 eV)	30 eV (4.3 eV)
1700 km (Freja)	9.9 km/s	8.2 eV (1.4 eV)	14.4 eV (2.5 eV)	29 eV (5.0 eV)
2000 km	9.8 km/s	8.0 eV (1.7 eV)	13.9 eV (3.0 eV)	28 eV (6.1 eV)
2500 km	9.5 km/s	7.5 eV (2.2 eV)	13.1 eV (3.8 eV)	26 eV (7.6 eV)
3000 km	9.2 km/s	7.1 eV (2.6 eV)	12.4 eV (4.5 eV)	25 eV (9.0 eV)
4000 km	8.8 km/s	6.4 eV (3.3 eV)	11.2 eV (5.7 eV)	22 eV (11.4 eV)
9000 km	7.2 km/s	4.3 eV (5.4 eV)	7.6 eV (9.4 eV)	15.2 eV (19 eV)
3 R_E	6.5 km/s	3.5 eV (6.2 eV)	6.1 eV (10.9 eV)	12.2 eV (22 eV)
4 R_E	5.6 km/s	2.6 eV (7.1 eV)	4.6 eV (12.4 eV)	9.1 eV (25 eV)
Venus 500 km	9.9 km/s	8.2 eV	14 eV	28 eV
Mars 500 km	4.7 km/s	1.8 eV	3.2 eV	6.4 eV

It is not trivial if the ions can acquire such "pre-energization" because the electric field (both DC and AC) available to energize the ions is normally very small near the exobase. In fact, even upflowing atomic O^+ ions often return back to the ionosphere (Loranc et al., 1991, Yamauchi et al., 2005). There are several mechanisms for the required pre-energization for overcoming gravity above the exobase, but predominantly it is wave-particle interactions. No matter what the mechanism is, the energization is often barely sufficient for a certain ion species to reach the main energization region such that the difference in the m/q by just a factor of two may render the energization insufficient for the heavier mass species to reach the main energization region. If the pre-energization just below 2500 km altitude is only 3–4 eV while the main energization altitudes are different between the dayside and the nightside, the absence of O_2^+ outflow in the nightside can easily be explained. Thus, it is quite possible that such acceleration is sufficient only for atomic ions such as O^+ (and H^+) but not for heavy molecular ions.

As mentioned above, we expect molecular O_2^+ to reach the main energization region at more equatorward latitudes than atomic O^+ due to the velocity filter effect in the nightside auroral region during geomagnetic storm conditions. Considering that there is less wave activity at lower latitude in the nightside sub-auroral region where O^+ upflow is observed, pre-energization by the wave activity can also be smaller at O_2^+ upflow latitudes than O^+ upflow latitudes.

In addition to the velocity filter effect inside the ionosphere, ionospheric chemistry, ionosphere-thermosphere coupling (see Sects. 2.2.1 and 2.2.2), and upward convection also play roles in determining the distribution of molecular and atomic ions at the topside ionosphere (near and above the exobase). These lead to significant differences for molecular ion distribution between the cusp region and auroral region, possibly allowing molecular ions to leave the ionosphere only from the dayside. Therefore, to understand the magnetospheric molecular ions, we need to know the composition and dynamics of molecular ions at the topside of the ionosphere, too.

In this respect, it is useful to compare heavy atomic ions (O^+) and heavy molecular ions (N_2^+, NO^+, and O_2^+) in terms of total flux only. At high altitude (such as Akebono and Polar altitudes) much above the main energization region, heavy atomic ions (O^+) are found over a wide latitudinal range. Through various route, these upflowing O^+ ions from both the low-latitude ionosphere and high-latitude ionosphere can enter the magnetosphere according to the past observation (e.g., Yamauchi 2019 for review). This is quite different from the heavy molecular ions for which the cusp source dominates in both occurrence and ion flux already at the Akebono altitude (Yau et al., 1993).

If energy-time profiles can be obtained for molecular ion observations, they give information even on the main energization mechanisms (electrostatic (DC) and electromagnetic (AC)) because they have different mass-per-charge dependences, from no dependence on electrostatic acceleration to mass dependency of ΔE nearly ~ $m^{(-0.5)}$. By knowing the altitude dependence of the flux ratio between different masses and energies, one can estimate the relative importance of different mechanisms at different altitudes, although the feasibility of such measurements is not evident. While the electrostatic (DC) acceleration is normally strong enough to give sufficient energy for all ions (independently of their mass) to reach high-altitude, such DC acceleration does not start below 2000 km altitude, and hence, heavy ions with only a few eV at exobase do not reach the DC acceleration region.

The detection of heavy ions also gives clues on how low the electromagnetic (AC) acceleration starts. On the other hand, AC acceleration might start from much lower altitudes during magnetic storms or other conditions, but details are unknown. If AC acceleration is strong enough and starts at low enough altitudes, even metallic ions may reach the DC acceleration region. Therefore, quantification of heavy ions in the magnetosphere provides information on the strength and altitudes of the AC acceleration.

2.2.4 How much change of atmospheric composition (e.g., N_2/O_2 ratio) on geological scales is caused by the ion escape?

Evolution of the Earth's atmosphere is another science theme that benefits from our knowledge of the magnetospheric molecular ions (N_2^+, NO^+, and O_2^+), in addition to atomic heavy ions N^+ and O^+ (e.g., Yamauchi, 2019). The present atmospheric composition is quite different from that of the other planets after 4.5 billion years of evolution (e.g., Mars and Venus for which the initial atmospheric composition is believed to be similar to that of the Earth, Lammer et al. (2008)). The difference in the atmospheric evolution must have influenced the habitability of these three planets: very limited habitability in best case for Mars (underground where water exists) and Venus (cloud layer where temperature is in the habitable range) compared to the full habitability for all known forms of life on the Earth.

From the viewpoint of evolution of life, a very small change of the atmospheric composition is important. A change of only a few percent in the atmospheric O_2/N_2 ratio or in the water pH, or a change of a few degrees in the atmospheric and water temperature may significantly affect the biochemical reactions and hence metabolism and photosynthesis (e.g., Loesche, 1969; Hill, 1976; Servaites, 1977; Ku et al., 1977; Harrison, 2010). A change of a few percent in the atmospheric N/O ratio corresponds to a change of about 10% in the nitrogen inventory in the present-day biosphere ($(4–5)\times10^{18}$ kg). This amount of loss is achieved by 600 million years ($=2\text{x}10^{16}$ sec) of average nitrogen loss rate of 10^{27} s^{-1} (about 20 kg/s). The same level of change (15% fluctuation in O_2 content) has actually occurred during a duration of 100 million years in the past according to the geological record (Berner, 2006). These durations and amount are short enough compared to the history of life and large enough in quantity, respectively, to affect bacteria through change in the N/O ratio in the atmosphere.

In addition, the simultaneous presence of significant amounts of N_2 and O_2 in an atmosphere is chemically incompatible over geological timescales, and hence, the present N_2/O_2 ratio must have resulted from the biological activity (Lammer et al., 2019; Stüeken et al., 2020; Dandouras et al., 2020), constituting a bio-signature.

The question is then what causes such changes and fluctuations of the atmospheric composition. There are six main channels that determine the evolution of the atmosphere: (a) net escape to space after removing the return flow; (b) net influx from space (e.g., meteors); (c) biospheric reactions (e.g., O_2 from photosynthesis); (d) sub-surface sink through ocean bottom; (e) emission from sub-surface through both non-organic (e.g., volcanic) and organic activities (bacterial denitrification) (Berner, 1999; Canfield, 2005; Barabash et al., 2007; Johnson and Goldblatt, 2015); and (f) geochemistry (e.g. CO_2 chemical capture through limestone formation) (Stüeken et al., 2020).

Among those, the net contribution of the biosphere (c) and from the Earth's interior (d and e) diminishes once the photosynthesis and mantle convection are stabilized because these contributions mainly recycle elements rather than causing net changes. Also, the net influx of biological elements (N, O, C) from space (b) is much smaller than that of escape to the space. On the other hand, (a) the escape to space causes net changes, and therefore its relative importance compared to the sub-surface migration is large in the geological time scale. The question is: how much?

The aforementioned escape rate to space of 10^{27} s^{-1} is not unrealistic during the ancient time of about 4 billion years ago, because the composition and amount (flux) should depend strongly on the solar UV, solar wind, and geomagnetic activity conditions, all of which are known to be much higher in the ancient than present (Yamauchi, 2019; references therein). This means that we can assume frequent Kp ~10 at that time (Krauss et al., 2012, Slapak et al., 2017). Due to increased frequency of high Kp activity, Kp ~10 can be used, the increased escape can be assumed almost continuously, rather than a summation of short-lived events of "massive escape" for the present days. Assuming escape rate decreasing linearly with time, Slapak et al. (2017) estimated the total loss of heavy atomic ions (O^+ and N^+) over 4 billion years as about 5 ×10^{17} kg, which corresponds to 40% of today’s total oxygen mass in the atmosphere.

In such a condition, i.e., during an enhanced outflow rate, energization of the ionosphere is also enhanced, allowing even molecular ions (N_2^+, NO^+, and O_2^+) to gain sufficient initial velocity to enter the outflow process (few-ten eV) within their relatively short dissociative recombination lifetime. Therefore, during "massive escape" events, flux enhancement of the ion outflow becomes more drastic for molecular ions than for atomic ions (and within atomic ions, N^+ outflow is more enhanced than O^+ outflow). These factors cause higher N/O ratio of the atmospheric loss during enhanced outflow rate, and hence in the ancient time in the geological scale.

The high N/O ratio of escaping elements is consistent with what has been observed in the very sparse observations that simultaneously detected the molecular ions (Yau et al. 1993, Hamilton et al., 1988). However, no quantitative value for N/O ratio or even molecular/atomic ratio for ion outflow flux (or upflow flux at low altitude) is available due to a lack of proper instruments in the magnetospheric missions covering a wide variety of escape routes and respective energy ranges. From the detection capability viewpoint, quantitative separation of N^+ and O^+ requires much higher m/Δm capability than separating molecular ions (N_2^+, NO^+, or O_2^+) from atomic ions (N^+ or O^+), but capable instruments have already flown on board planetary missions such as Cassini, Kaguya, MAVEN, Bepi-Columbo, and JUICE.

2.3 Importance and present knowledge of the mesospheric sources (metallic ions)

Figure 2.1 demonstrates the existence of accelerated (> 100 keV) low charge-state metallic ions (such as Fe^+) in the magnetosphere, although their flux is much lower than the flux of the solar wind metallic ions entering the magnetosphere. This also indicates that some ions with m/q ≈ 30 can also be Si^+. The low charge-state indicates that they must come from either from the Moon (see Sect 2.4) or the atmosphere. Although metallic species are a very minor component of the atmosphere, there are several layers of metallic species in the mesosphere and lower thermosphere, mainly from the ablation of cosmic dust entering the Earth's atmosphere, as illustrated in Figure 2.5.

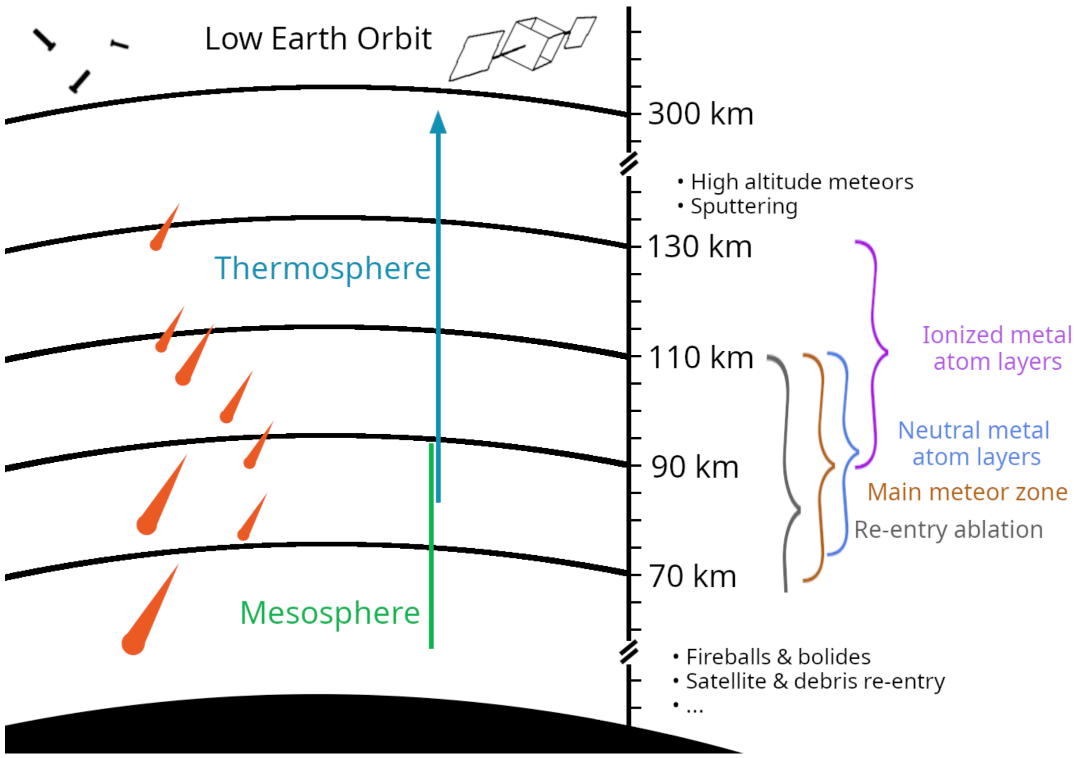

Fig2.5: Illustration of the ablation of material entering the atmosphere, showing relevant altitude ranges.

2.3.1 Meteoroids and the metal layers

Every day the Earth's atmosphere is bombarded by billions of dust-sized particles and larger pieces of material from space. The primary sources of these cosmic dust particles are the sublimation of volatile species in comets as they are heated by the Sun, which release dust particles that are then ejected by drag forces, and collisions between asteroids in the main asteroid belt between Mars and Jupiter (Plane et al., 2018b). These particles are collectively termed meteoroids. Because the particles range in size by more than 12 orders of magnitude as shown in Figure 2.6 (Murad and WIlliams), estimating the total input of cosmic dust into the atmosphere is very challenging, with estimates ranging from roughly 5 – 300 t d^{-1} (tonnes per day) (Plane et al., 2012).

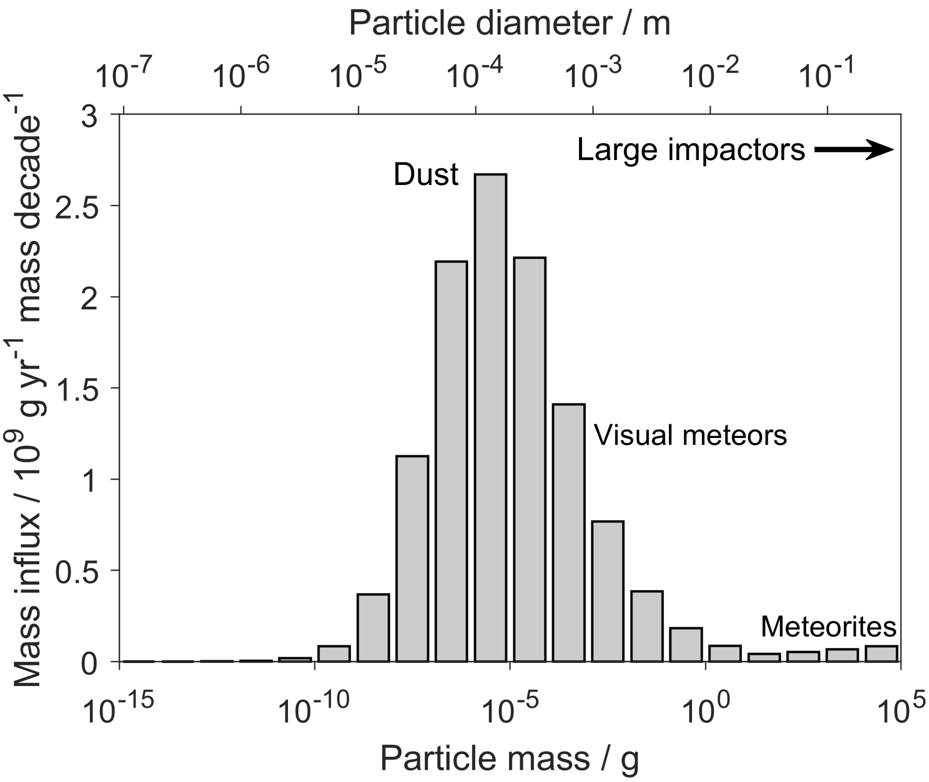

Figure 2.6. The annual meteoroid mass influx (expressed per decade of mass) plotted against particle mass, adapted from Plane et al. (2018b) and Schulz and Glassmeier (2021).

The most likely value currently is thought to be around 30 t d^{-1}, based on measurements of the vertical fluxes of Na and Fe atoms which ablate from dust in the lower thermosphere and upper mesosphere, and the accumulation of cosmic spherules (dust particles that melt but do not completely evaporate) at the South Pole (Carrillo-Sánchez et al., 2020). This input rate is corroborated by the optical extinction of meteoric smoke particles (which form from the polymerisation of metallic compounds produced from ablated metal atoms) in the lower mesosphere (Hervig et al., 2021), and the accumulation of unmelted micrometeorites in a large collection from Concordia in Antarctica (Rojas et al., 2021) as well as earlier estimates considering their respective biases (Schulz and Glassmeier, 2021, and references therein).

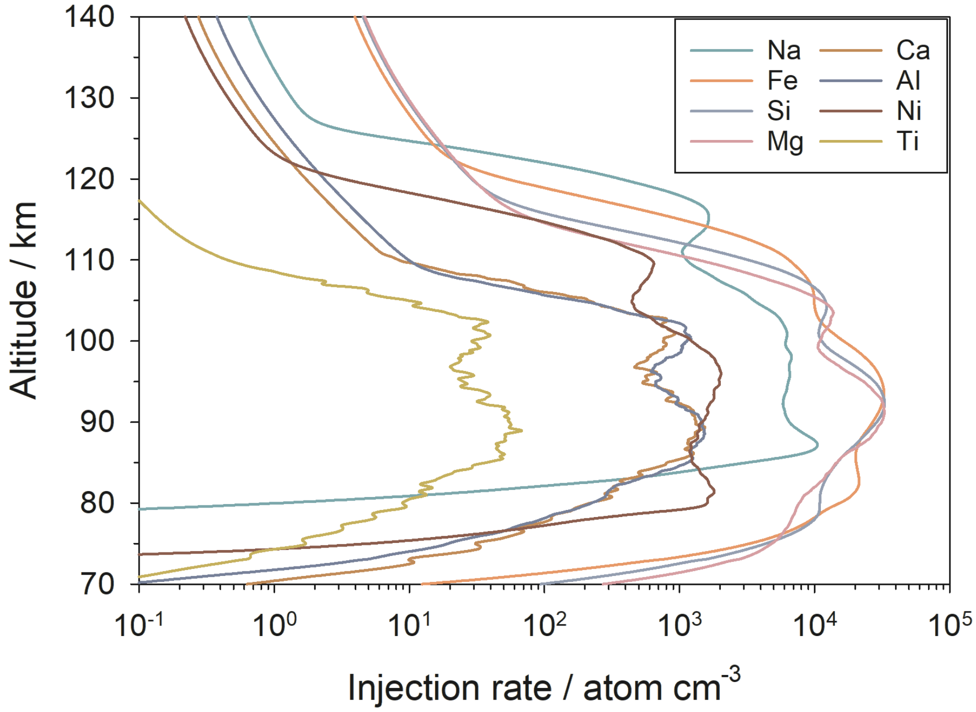

Figure 2.7. Global average ablation rates as a function of altitude for the main metal constituents in cosmic dust (Carrillo-Sánchez et al., 2020).

As meteoroids enter the atmosphere, they undergo heating by inelastic collisions with air molecules. If they reach the melting point (~1800 K), then ablation (i.e., evaporation) of the constituents becomes rapid. Initially the relatively volatile elements (Na and K) ablate, followed by the main constituents (Fe, Mg and Si) around 2000 K. Finally, the refractory elements (Ca, Al and Ti) ablate if the particle reaches a temperature over 2400 K (Vondrak et al., 2008). Figure 2.7 shows the ablation rates of the individual elements as a function of altitude, illustrating that most ablation occurs between 70 and 110 km (Carrillo-Sánchez et al., 2020). This injection is the source of the layers of neutral metal atoms that occur globally between about 75 and 110 km, and the layers of ionized metal atoms between about 90 and 130 km (Plane, 2003; Plane et al., 2015a)

Metallic atoms have comparatively low ionization energies. Since they are initially travelling at the same speed as their parent meteoroid, they can undergo collisional ionization with air molecules. The meteoroid energy velocity ranges from 11 km s^{-1} to 72 km s^{-1}, and the ionization probability strongly depends on the velocity (see Figure 3 in Janches et al., 2017). The resulting dense plasma, together with optical emissions from atoms and molecules in excited electronic states, is termed the meteor, which moves together with the ablating meteoroid (Ceplecha et al. 1998). If the meteoroid survives the ablation process and reaches the ground, it is termed a meteorite. Note that the analysis of meteorites and observations of meteor spectra provide conclusive evidence that the meteoroid population contains metallic elements roughly in same abundance as the photosphere (Asplund et al., 2009; Lodders et al., 2009, Kero et al., 2019).

There have also been rare observations of the meteor phenomena at altitudes up to 200 km. For optical observations these events have been mainly explained by sputtering (non-thermal ablation) (Popova et al., 2007). With sufficient meteoroid size and velocity, sputtering can create enough photons to be detected by optical systems (Koten et al., 2006). The majority of published optical observations of high altitude meteors originate from the Leonid meteor shower due to its very high velocity (about 70 km s^{-1}). These events are also characterized by the sputtering-dominated part of the meteor event with a brightness that is several orders of magnitude fainter then the thermal ablation part, indicating that a much smaller part of the meteoroid mass is lost at these altitudes (Vondrak et al., 2008). High altitude meteors have also been observed with radars. However, the very high-altitude cases (>150 km) are still an open question due to possible ambiguities in the observation techniques (Brosch et al. 2013; Vierinen et al. 2014; Gao and Mathews 2015). Radar observations of high-altitude meteors up to 142 km have been validated with respect to such ambiguities (Kastinen and Kero 2022) and may be explained by thermal ablation, particle disruption, and/or the pyrolysis of refractory organics within the dust particles (Bones et al., 2022).

To determine the altitude and element distribution of mass deposition in the atmosphere, the meteoroid atmospheric entry needs to be modelled. For an overview of modelling the atmospheric entry of meteoroids (Ryabova et al., 2019, and references therein). These models have been widely used for determining the physical properties of meteoroids from observations (e.g., Gritsevich 2009; Campbell-Brown et al., 2013), and for estimating the injection flux of metals into planetary atmospheres as input when modelling the atmospheric chemistry and dynamics in the mesosphere and lower thermosphere (Plane et al., 2015a). In recent years, chemical ablation models have been tested using different types of laboratory meteoric ablation simulators (Gomez Martic et al., 2017; Thomas et al., 2017) to constrain chemical ablation models, such as the CABMOD model which now includes separate metal silicate and Fe-Ni-S phases (Bons et al., 2019).

In Hulfeld et al., (2021), the break-up of dustball meteoroids was simulated using fluid dynamics simulations of the meteoroid's atmospheric entry flow, including both thermal and mechanical break-up mechanisms. A Draconid meteoroid was simulated starting with compression by the aerodynamic forces to approximately half its size at the beginning of the simulation (200 km altitude), and then mechanically disintegrated at 120 km altitude due to aerodynamic-induced meteoroid rotation. In contrast, camera and radar observations of Draconids show a lower break-up altitude of ~ 100-110 km (Borovička et al. 2007, 2014; Kero et al. 2012). These studies indicate that there may be an additional influx of meteoroid material that disperses (=ablates) at higher altitudes than regular thermal ablation of a single solid body allows.

2.3.2: Observations of metallic ions in the thermosphere/ionosphere

Metallic ions in the lower thermosphere (lower ionosphere) have long been detected and observed by both in-situ observation (rockets and satellites) and remote observation (ground and satellites), although the spatial and temporal resolution at higher altitude is insufficient to reveal the vertical transport.

(a) Spaceborne observations

For in-situ sampling, the mass spectrometer on board Atmosphere Explorer C (AE-C) satellite detected patches of Fe^{+} between 220 and 320 km that seemed to be associated with regions of upward plasma transport (Grebowsky and Brinton, 1978). Moreover, the retarding potential analyser (RPA) on board OGO-6 satellite occasionally observed Fe^+ at much higher altitudes between 600 and 950 km (Hanson and Sanatani, 1971; Hanson et al., 1972). Measurements of metallic ions up to around 130 km have been made using ion mass spectrometers on sub-orbital rockets, mostly at mid- and high-latitude locations. This type of experiment provides vertical profiles with typically 2 km height resolution of all ions with masses below ~100 amu and concentrations larger than ~10 cm^{-3}, but not at middle and upper ionosphere. These measurements were mostly made in the 1970s and 1980s (for review, Kopp, 1997; and Grebowsky and Aikin, 2002).

Metallic species such as Mg^+ and Fe^+ have also been observed by resonant scattering of sunlight, for example by the Space Shuttle (Gardner et al., 1995; 1998). An optical spectrometer, ARGOS/ISAAC, detected clear Fe^+ emission in the 100-340 km altitude region (Dymond et al., 2003). In the last 15 years, spaceborne limb-scanning optical spectrometers have been used to determine the vertical profiles of metal atoms and ions: the Optical Spectrograph and Infra-Red Imager System (OSIRIS) spectrometer on the ODIN satellite for Na (Hedin and Gumbel, 2011) and K (Dawkins et al., 2014); and the Scanning Imaging Absorption Spectrometer for Atmospheric Chartography (SCIAMACHY) spectrometer for Mg and Mg^+ (Langowski et al., 2015) and the Global Ozone Measurement by Occultation of Stars (GOMOS) spectrometer for Na (Fussen et al., 2010), both on the Envisat satellite.

(b) Resonance lidars

The first measurements of metal atom densities (Na, K, Fe and Ca^+) in the upper mesosphere were made in the 1950s using ground-based twilight photometry, where resonance fluorescence from spectroscopic transitions of metal atoms excited by solar radiation was measured during twilight (Hunten, 1967). These measurements were superseded in the 1970s when the development of tunable lasers led to the resonance lidar technique (Plane, 1991). Lidar has been used to observe Na, K, Li, Ca, Ca^+ and Fe (Plane, 1991), and recently Ni (Gerding et al., 2019). Most of these observations have focused on the main metal layers between 75 and 110 km.

One important development in the past 15 years has been the use of high performance lidars to extend observations into the thermosphere of Fe (Schneider et al., 2015) and Na

(Liu et al., 2016) above 150 km, K and Ca up to 130 km (Höffner and Friedman, 2004, 2005; Friedman et al., 2013), and Ca^+ up to 180 km (Raizada et al., 2020). Even the diurnal observations became possible (Plane, 2003). Thus, it has long known that these metallic species exist at detectable levels in the lower thermosphere/ionosphere.

2.3.3 Transport to the exobase (old sec 5.3.2)

In the thermosphere, metals exist almost entirely as metallic ions after the efficient ionization either by charge exchange with ambient NO^+ and O_2^+ ions, or by photoionization (Plane et al., 2015a). Unlike the molecular ions such as NO^+ which undergo rapid dissociative recombination with electrons, metallic ions can only undergo dielectronic or radiative recombination with electrons, a process about 10^6 times longer lifetime (Plane et al., 2015a). Thus, the metallic ions have lifetimes of days in the thermosphere.

Table 2.3 Metallic elements and their mass

ions	mass	molecular ions with same mass	space debris
Na^+	m=23		
Mg^+	m=24		
Al^+	m=27	HCN^+	yes
Si^+	m=28	N_2^+, CO^+	yes
P^+	m=31	$^{15}N^{16}O^+$ or $^{14}N^{17}O^+$	
S^+	m=32	O_2^+	
K^+	m=39		
Ca^+	m=40		
SiO^+	m=44	CO_2^+	
Ti^+	m=48		yes
Fe^+	m=56		yes
Ni^+	m=59		yes
Cu^+	m=64		yes
Ge^+	m=73		yes

Furthermore, some metallic ions like Na^+ (m=22), Mg^+ (m=24), Al^+ (m=27), Si^+ (m=28), P^+ (m=31), and S^+ (m=32) have similar or even larger m/q compared to heavy molecular ions, allowing them lifted upward longer distances than heavy molecular ions within the lifetime. Such long upward distance even applies to the other relatively abundant heavy metallic ions, such as K^+ (m=39), Ca^+ (m=40), SiO^+ (m=44), Fe^+ (m=56), Ni^+ (m=59), Cu^+ (m=64), because them have masses that are within a factor of two of the heavy molecular ions listed in Table 2.3 (here, we note that mass 44 in the magnetosphere is not necessarily CO_2^+, but could also be SiO^+ of lunar origin).

Since molecular ions must be transported from the lower ionosphere to reach the exobase within the dissociation timescale, the same "strong" upward ion convection in the ionosphere may also transfer metallic ions against the gravity (particular those lighter than O_2^+) from the lower ionosphere. Inversely, the detection of the heavy molecular ions ($m/q \approx 30$) above the ionosphere by e-POP suggests that metallic ions may also access the topside ionosphere (exobase). If one can measure the ratio of metallic ions and molecular ions of similar masses in the ion outflow above the ionosphere, the variation of this ratio indicates change in the convection and/or change in the chemical reaction.

Unfortunately, no dedicated instrument or mission exists in a terrestrial orbit to monitor such ions leaving the ionosphere or arriving at the topside ionosphere from lower altitudes. Meanwhile, modeling efforts have advanced to include the metallic ions and atoms, as described in Sect 4.3.3.

2.3.4 Possible human-made contribution by atmospheric re-entry of space debris

Out-of-service satellites, rocket bodies, and subsequent fragmented parts, together constitute space debris. Their re-entering into Earth's atmosphere causes the same ablation process as the entry of meteoroids although with much smaller entry velocities (~ 8 km/s), shallower entry angles and different composition, resulting in the deposition of metallic atoms and ions into the upper atmosphere (Schulz and Glassmeier, 2021). Returning spacecraft with astronauts and goods may experience the same process, but the degree of ablation is much smaller than that of space debris for which re-entry is designed to result in complete ablation, and therefore this is included in the category of "ablation of space debris" or a wider terminology of "ablation of space waste".

Currently, the mass injected into the atmosphere by re-entering space debris is only a fraction (about 3 % in 2019) of what is injected by meteoroids (Schulz and Glassmeier, 2021). However, metallic species are present in much higher fraction in space debris than in meteoroids, resulting in the atmospheric re-entry flux of some metallic species (mainly

Al and Li, but also Ni, Cu, Ti, and Ge) from space debris surpassing the entering flux of the same species from meteoroids. For these species, the annual mass input to the whole atmosphere will exceed or has already exceeded the natural input considering the strong increase in launch activity every year. The details of such future increase and its implications are discussed in section 4.3.2. All this poses the question how much the input of re-entering space debris contaminates the natural origin metallic atoms and ions in the mesospheric metal layers. To answer the question, knowledge about the ablation characteristics of entering space debris and the subsequent chemical processes are vital.

For re-entering space debris, ablation starts as high as 110 km (Fritsche et al. 2000, Klinkrad 2005, Rafano Carná and Bevilacqua 2018) which is 20 km lower than the meteoroid cases. For larger spacecraft (few 100 kg or more), the main part of mass loss takes place at altitudes below 80 km depending on the spacecraft velocity, entry angle, mass, and composition (Reynolds et al. 2001, Lips et al. 2005, Battie et al. 2013, Buttsworth et al. 2013, Jenniskens et al. 2016 and Park et al. 2021). For example, debris on a very elliptic orbit (high-apogee) enters the atmosphere with higher velocity and angle than low-Earth orbit (LEO) debris. Note that Buttsworth et al. (2013) and Jenniskens et al. (2016) considered non-typical re-entries (very high apogee orbits, thus a very high entry velocity and angle compared to LEO spacecraft), allowing the spacecraft survive to lower altitudes for long-lasting ablation.

Metallic atoms that ablate below 80 km will quickly be oxidized to metal oxides, hydroxides and carbonates (Grebowsky et al., 2017). For instance, an Fe atom that ablates at around 64 km will be oxidized to FeO by O_3 in about 2 s (Grebowsky et al., 2017), and Al will be oxidized by reaction with O_2 much more rapidly (Plane et al., 2021). Oxidized metallic species that form below 80 km as a result of the ablation of space debris will rapidly polymerize with themselves or the background population of nanometer-sized meteoric smoke particles that are produced from meteoric ablation (Plane et al., 2021). These tiny particles will then be transported down to the Earth's surface by the residual atmospheric circulation. An increase in the number and size of these particles as a result of space debris may have some effect on the stratospheric ozone layer (e.g. freezing polar stratospheric clouds droplets (James et al., 2018) or removing the main chlorine reservoir HCl (Plane, 2003)). However, the particles are very unlikely to be transported above 90 km, such that they provide a source of thermospheric metallic ions after decomposing.

In contrast, for metals that ablate from space debris above 80 km, the high background concentrations of atomic O and H in the upper mesosphere (Plane, 200) will maintain a high level of metal atoms (or AlO in the case of Al) because they reduce metal oxides and other compounds. These metals may then be transported to the lower thermosphere, analogously to the transport of ions from the natural metal layers, and ionized.

2.4 Importance of the Moon as source and present knowledge (sputtering and pickup process)

The Moon is a source of heavy ions. These ions are generated on the lunar surface either directly sputtered from the lunar surface by impact of solar wind plasma or magnetospheric plasma (Yokota et al., 2009, Wieser et al., 2010), or by the photoionization (solar UV and EUV) of the neutral exosphere (Stern, 1999). These exospheric neutrals are originally generated by (1) micro-meteorite impact vaporization, (2) solar photon stimulated desorption, (3) sputtering by the solar wind and magnetospheric ions, and (4) thermal desorption (Colaprete et al. 2016; Wurz et al. 2022).

Since these Moon-origin ions are typically high mass but singly charged, m/q values are much higher than those of the solar wind ions (all species have similar m/q within a factor of 2). Therefore, the gyroradius of the Moon-origin ions after gaining the solar wind speed due to the pick-up process is quite different from those of the solar wind. This uniqueness of the lunar metallic species makes even a tiny amount of the ion as a tracer to give extra information in the ion dynamics at the magnetospheric boundary.

2.4.1 Formation of the exosphere and ion pickup

The lunar exosphere, although very thin according to Apollo observations (Stern, 1999), has been observed by Lunar Atmosphere and Dust Environment Explorer (LADEE) mission (Mahaffy et al., 2015; Halekas, et al., 2015). The column densities of alkali elements (K and Na) on the Moon observed by LADEE increased during the meteor shower events during its mission from November 2013 to April 2014 (Colaprete et al.

2016). For the Leonid meteor shower (November) and Geminid meteor shower (December), response was sharper for K than Na, whereas for Quadrantid meteor shower (January) the response was small and nearly the same for both elements. These meteor showers are more important than CIRs or CMEs for the production of the exospheric neutrals (Colaprete et al. 2016).

As for the composition, Neutral Mass Spectrometer (NMS) on board LADEE has reported observations of lunar exospheric ions (at low energies < 25 eV) in the lunar orbit when the Moon was in the solar wind. Using the dedicated ion mode (Mahaffy et al., 2015), ions of expected species of the lunar exosphere were recorded at masses 2 (H_2^+), 4 (He^+), 16 (O^+), 20 (Ne^+), 23 (Na^+), 39 (K^+), and 40 (Ar^+) amu, but also of unexpected ions including $^{12}C^+$, $^{14}N^+$ and at mass 28, which could be Si^+, N_2^+ or CO^+ (the presence of ^{12}C (Halekas et al., 2015) suggests that it is most likely CO^+). These observed ions originate from the exosphere, rather than directly from the surface (Mahaffy et al., 2015).

Lunar Dust Instrument (LDEX) on board LADEE showed that the electric current, which is most likely monitoring the lunar pickup ions, is linearly correlated with the solar wind flux (Poppe et al., 2016b, Fig. 3). The reported ion fluxes are best fit by total exospheric ion production rates of about 6×10^3 m^{-3} s^{-1}. Since LDEX does not have a means to identify the mass of the recorded ions, the ion composition was inferred based on modelling with dominant contributions from Al^+, CO^+, and Ar^+.

2.4.2 Sputtering from the lunar surface

The sputtering from the lunar surface is theoretically expected (Yokota and Saito 2005; Futaana et al., 2006; Wurz et al., 2007) and actually observed by Kaguya (SELENE) and Chandrayaan-1 lunar orbiters. Kaguya Ion Mass Analyzer (IMA) detected the sputtered ions of many species together with the ionized exospheric neutrals and the reflected solar wind ions (Yokota et al., 2009; Tanaka et al., 2009). Chandrayaan-1 Sub-keV Atom Reflecting Analyser (SARA) detected sputtered neutral hydrogen and heavy atoms of oxygen mass group (Wieser et al., 2010; Vorburger et al. 2014).

The sputter yields from general surfaces are energy dependent, and approaches zero for lower energies, because the energy deposited in the surface by the impacting ion is not sufficient to overcome the binding energy of atoms at the surface. The sputter yield also approaches zero for very high energies because high-energy ions penetrate deeper into the solid without depositing significant energy at and near the surface to cause the release of particles. The maximum yield is expected at an energy around 1 keV/nuc of the impacting ions for the lunar case (Wurz, 2012; Wurz et al. 2022), which compatible with ions with the solar wind velocity (for all species) and with the thermal magnetospheric plasma (light ions).

This means that we expect effective sputtering from the lunar surface when the Moon is exposed to the solar wind. Particularly, we expect drastic increases in the surface sputtering by CMEs (Leblanc et al., 2022) because a CME is accompanied by drastic flux enhancements of the heavy ion component: the degree of flux increase is much greater than that for H^+ (Wurz et al., 2001, 2003; Wimmer-Schweingruber et al., 2006). The effective sputtering is even expected in the magnetospheric plasma lobe or magnetosheath. On the other hand, contribution by EUV (ionization of exospheric heavy atoms by EUV) should not cause such drastic change compared to the sputtering contribution because the solar flare that is very short-lived.

Elphic et al. (1991) conducted a laboratory study of the ion emission caused by ion impact on materials (sputtering) with solar wind-like ion and material analogue to the lunar surface. Using H^+ and He^{++} primary ions, they found that these ions produce significant fluxes of sputtered ions (so-called secondary ions) of lunar surface material, including Na^+, Mg^+, Al^+, Si^+, K^+, Ca^+, Ti^+, Mn^+, and Fe^+, although H^+ and He^{++} are not efficient sputterers. The predicted secondary ion fluxes from the lunar surfaces is between ~10 and 10^4 ions cm^{-2} s^{-1}, depending on the species. Thus, the range of relative ion yields covers four digits of variation depending on sputtered ion species. Similar studies were performed on Apollo soils (soil number 10084 and soil number 62231) and on a synthetic Corning glass lunar simulant (Dukes and Baragiola, 2015). X-ray photoelectron spectroscopy was correlated with the spectra of secondary ions ejected from these soils by 4 keV He ions. The ejected secondary ion species from the Apollo soils by 4 keV He include the atomic ions: Na^+, Mg^+, Al^+, Si^+, Ca^+, Ca^{++}, Ti^+, Fe^+, and molecular the ions: NaO^+, MgO^+ and SiO^+.

Yokota and Saito (2005) modelled the ion production near the Moon, at 100 km above the surface, including photoionization of the lunar exospheric atoms, photon-stimulated ion desorption, and ion sputtering. They proposed that an intense flux of picked-up lunar ions (10^4 cm^{-2} s) exists at an altitude of 100 km, for nearly a quarter of the orbit, with the main contributions from Na^+, Mg^+, Al^+, Si^+, K^+, Ca^+, Ti^+, Mn^+, and Fe^+ ions. In the other model by Sarantos et al. (2012), ion species of Ti^+, Fe^+, Mg^+, and especially Ca^+ are mainly ejected from the surface, and ionization of the exospheric constituents the other species, leading to the estimated fluxes that significantly exceed the ion production rate at the surface. These sputtering yields also depend on the lunar geographical areas (Futaana et al., 2006) as confirmed by Chandrayaan-1 (Wieser et al., 2010).

2.4.3 Amount and composition of ions leaving the Moon: Kaguya observation

Kaguya/IMA made the first in-situ detection of the heavy ions originating from the lunar surface and exosphere in a polar orbit with an altitude of 100 km, 50 km, and in an elliptical orbit with perigee altitude as low as 10 km (Saito et al., 2010). Kaguya/IMA is capable of detecting Moon-origin ions (both sputtering ions directly from the surface and pickup ions in the terminator region) for energy up to 12 keV/q. In their observation at 100 km altitude, Kaguya/IMA detected heavy ions including C^+, O^+, Na^+, K^+, and Ar^+ originating from the Moon surface/exosphere (Yokota et al., 2009; Lee et al., 2024) when the Moon was in the solar wind.

The Kaguya/IMA observation confirms that the sputtered ions have energies of about a few hundred eV in most cases, in agreement with the above expectation (Yokota et al., 2009, 2020; Tanaka et al., 2009). Figure 2.8a shows an example of such Kaguya observation. However, when a CIR (Corotating Interaction Region) passed the Moon carrying enhanced IMF and solar wind speed (which causes also an enhanced convection electric field), the energy of the sputtered heavy ions can become even higher than the incident solar wind proton energy, as shown in Figure 2.8b. More importantly, the ion flux of heavy ions drastically increased during the CIR passage, as shown in Figure 2.9 (same events as Figure 2.8). Note that the CIR contains H^+, He^{++}, He^+, C^+, O^+, Na^+/Mg^+, A^{l+}/Si^+, P^+/S^+, K^+/Ar^+, Mn^+/Fe^+. Existence of the high-energy low charge-state metallic heavy ions associated with CIRs indicates that the contribution of the solar wind sputtering becomes important when the solar wind pressure is high.

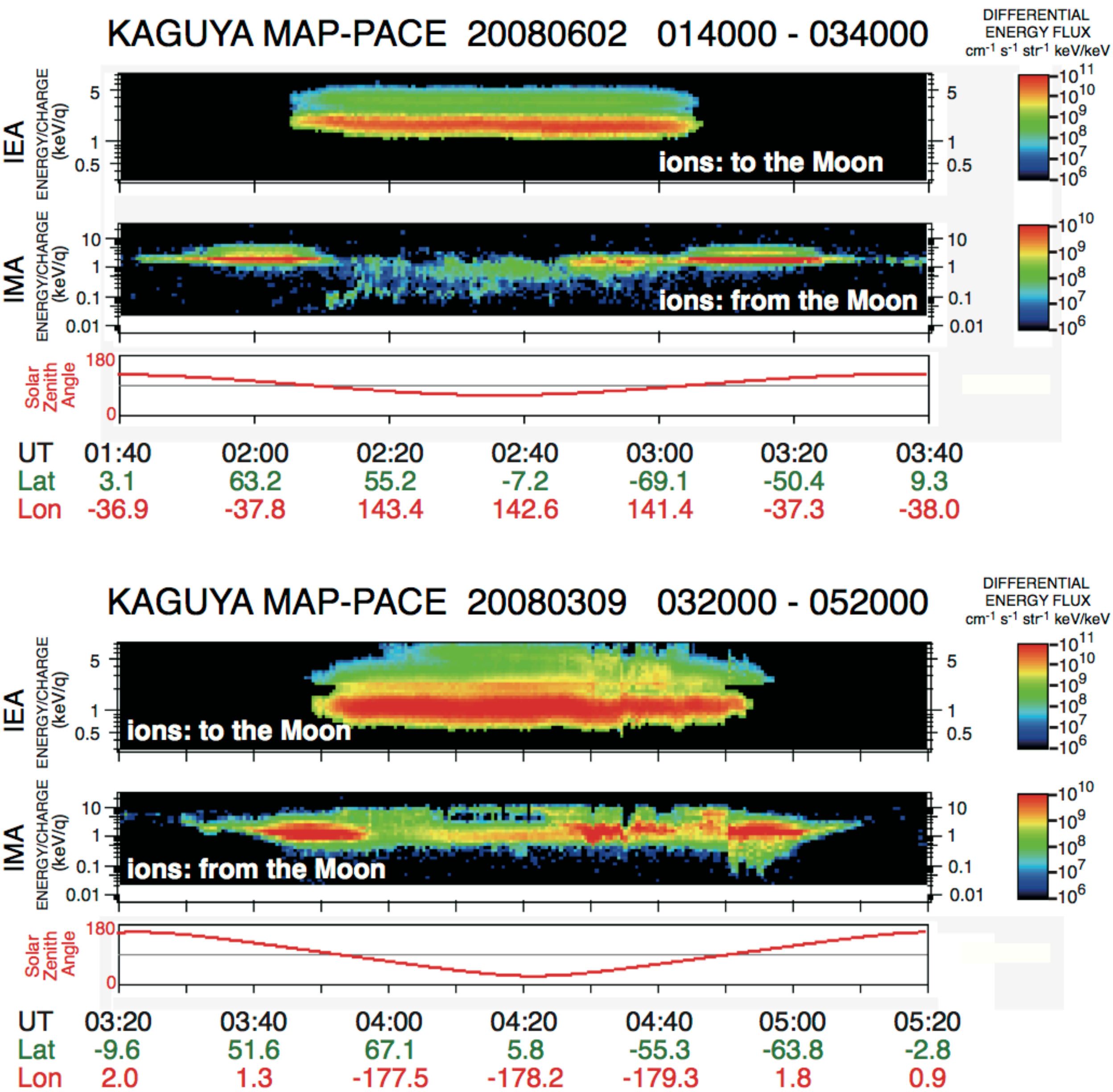

Figure 2.8: Energy-time spectrogram of ions observed by MAP-PACE on Kaguya during (a) normal solar wind condition on 2 June 2008, and (b) CIR on 9 March 2008. Moon is located upstream of the bow shock in the subsolar region. Ions measured by IEA (without mass separation) looking above the spacecraft (injection to the Moon surface) and Ions measured by IMA (with mass separation) looking downward the spacecraft (emission from the Moon surface) are shown.

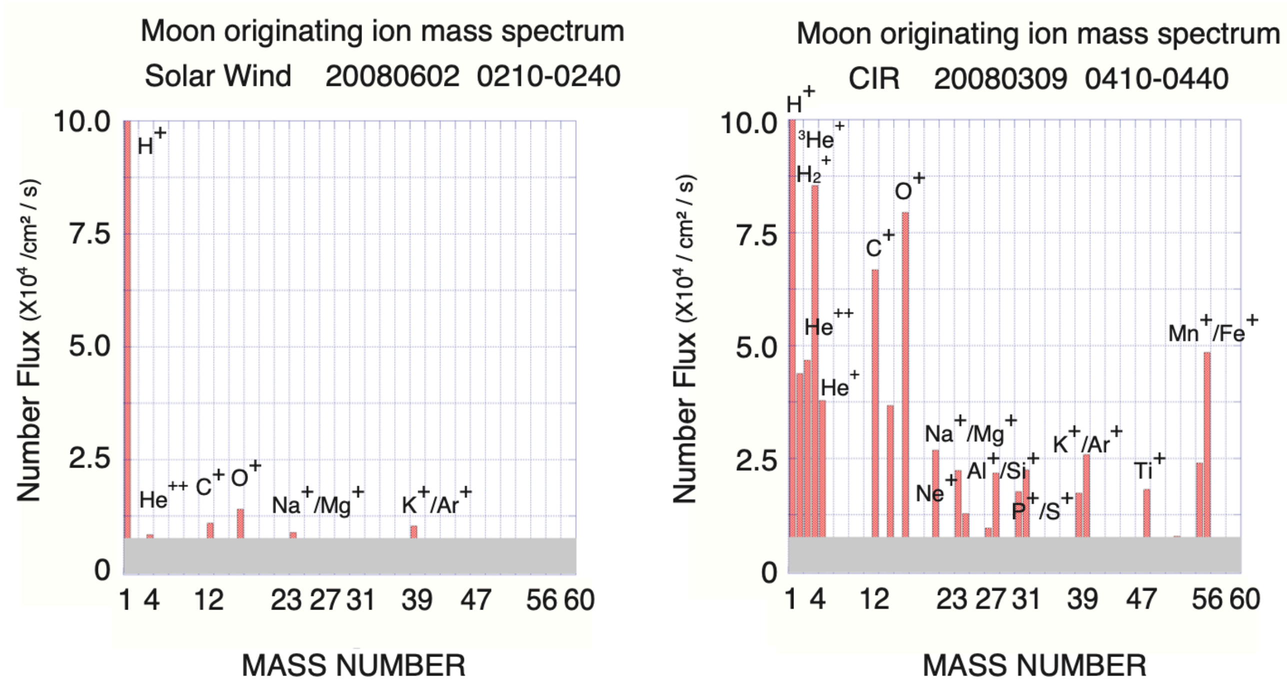

Figure 2.9: Number fluxes of ions coming from the lunar surface for the same days as Figure 2.8. Left: during a normal solar wind condition (2 June 2008, Figure 2.8a). Right: during a CIR (9 March 2008, Figure 2.8b). Low charge-state indicates that they are sputtered ions from the lunar surface rather than reflected solar wind. In both cases Kaguya was located upstream of the bow shock.

The Moon-origin ions were also detected even when the Moon stayed in the Earth's magnetosphere lobes (Tanaka et al., 2009), where the direct impact of the solar wind is less pronounced. These ions were observed on the dayside of the Moon, especially when the solar zenith angle was below 40 degrees. IMA detected peaks of flux for the heavy ions including C^+, O^+, Na^+, K^+, and Ar^+. These ions were mostly accelerated by the convection electric field in the Earth's magnetotail. The ions originating from the lunar surface and the exosphere showed characteristic variation of the flux intensity that presumably related to the lunar surface structure or composition.

When the Moon stayed in the Earth's magnetosphere, during a high geomagnetic activity period, the IMA instrument detected both lunar O^+ ions, originating from the Moon surface, and energetic O^+ ions originating from the Earth's ionosphere and streaming downtail (Terada et al., 2017). These two O^+ populations are clearly distinguished from their distribution functions and their energy spectra, the terrestrial O^+ ions streaming downtail with energies of the order of few keV whereas the lunar O^+ ions have energies of the order of ~10 eV.

With the ion electrostatic analyzer on board the Acceleration, Reconnection, Turbulence and Electrodynamics of the Moon's Interaction with the Sun (ARTEMIS) mission, lunar pickup ions were observed when the Moon was within the terrestrial magnetotail lobe (Halekas et al., 2012; Poppe et al., 2012). Although ARTEMIS does not have any instrument that can separate the mass, it is possible to infer the existence of heavy ions if accurate ion and electron densities can be obtained. Assuming that the density calculation is accurate, Zhou et al. (2013) compared electron density and ion density when ARTEMIS detected similar energy-time profiles as Kaguya (lower energy from the solar wind or lobe plasma and the thermal component does not exist) during high flux periods, and found that the calculated ion density (assuming proton) is 5 time higher than the electron density most of the time, suggesting a significant fraction can possibly be consisting of heavy species.

2.4.4. Magnetospheric observation of possible Moon-origin ions

Thus, the very heavy ions of the lunar origin (sputtered ions/neutrals from the surface or ionized exospheric neutrals) constantly exist in the "lunar ion wake" (downstream plasma region of the Moon where pickup heavy ions may reach, and is wider than the lunar wake in the flow dynamical meaning due to the finite gyroradius of heavy ions). The generated heavy ions are accelerated by the solar wind convection electric field and are finally picked up, with their flux varying depending on the solar wind conditions. The question is then how much these ions contribute to the metallic ions in the magnetosphere, such as those detected by Geotail/STICS (cf. Figure 2.1). Here, we dismiss the case when the Moon is located in the Earth's magnetotail because we do not expect the Moon-origin ions to return to the Earth against the strong anti-sunward plasma flow at the Moon location, as is confirmed by Geotail/STICS (Christon et al., 2020).

Therefore, we consider the case when the Moon is located upstream of the Earth, or more precisely, when the magnetosphere in within the "lunar ion wake" (downstream plasma region of the Moon where pickup heavy ions may reach, and is wider than the lunar wake in the flow dynamical meaning due to the finite gyroradius of heavy ions). Then, the ~60

Re distance from the Earth is far enough for these pickup ions to gain the solar wind speed even for Fe^+ with its large gyroradius, reaching to nearly 100 keV for Fe^+. Considering further energization in the bow shock and magnetosheath, the other metallic ions with less mass may also reach the energy detectable by the Geotail/STICS and Wind/STICS instruments.

Metallic ions that are consistent with the Moon-origin ions (also consistent with Earth's origin from the metal layer) are actually detected upstream of the Earth. With the STICS instrument on the WIND spacecraft, low charge-state heavy metallic ions were observed during flybys on the earthwards side of the Moon as close as 17 lunar radii well in front of the Earth's bow shock (Mall et al., 1998). The ion composition measurements in the energy range of 20 – 200 keV/q show O^+, Al^+, and Si^+ ions and heavier ions. The Active Magnetospheric Particle Tracer Explorers (AMPTE) SULEICA instrument detected ions in the m/q range of 23-37 were observed in the solar wind upstream of the Earth's bow shock (Hilchenbach et al., 1993), with ion fluxes of at least 0.3 cm^{-2} sec^{-1} sr^{-1} keV^{-1} in the energy range of 5 keV/q to 230 keV/q.

Figure 2.10 summarizes these upstream observations (by Wind/STICS and AMPTE/SULEICA) and compared with the Geotail/STICS observation. Although the Geotail/STICS count rate of these low charge-state metallic ions is, including all sources, normally 0-1 count/day, the operating lifespan of more than 20 years and its ~9 x ~30 Re orbit allowed statistical studies of near-Earth heavy ions in the magnetosphere, the magnetosheath, and the solar wind sunward of Earth. In Figure 2.10 (cf. Christon et al., 2020), the peak mass around $m/q \approx 30$ is substantially different between the upstream data (black trace in (C), around mass 27 - 28: Al^+ and Si^+) and magnetospheric data (red trace in (C), around mass 30 - 32: NO^+ and O_2^+). Unlike the magnetospheric peak that is dominated by the molecular ions (N_2^+, NO^+, O_2^+), the upstream peak is centered at Al^+ and Si^+ (slightly lower mass than molecular ions) in good agreement with mass spectra observed by Kaguya and LADEE (Saito et al., 2010; Halekas et al., 2015) as described in Sect. 2.4.

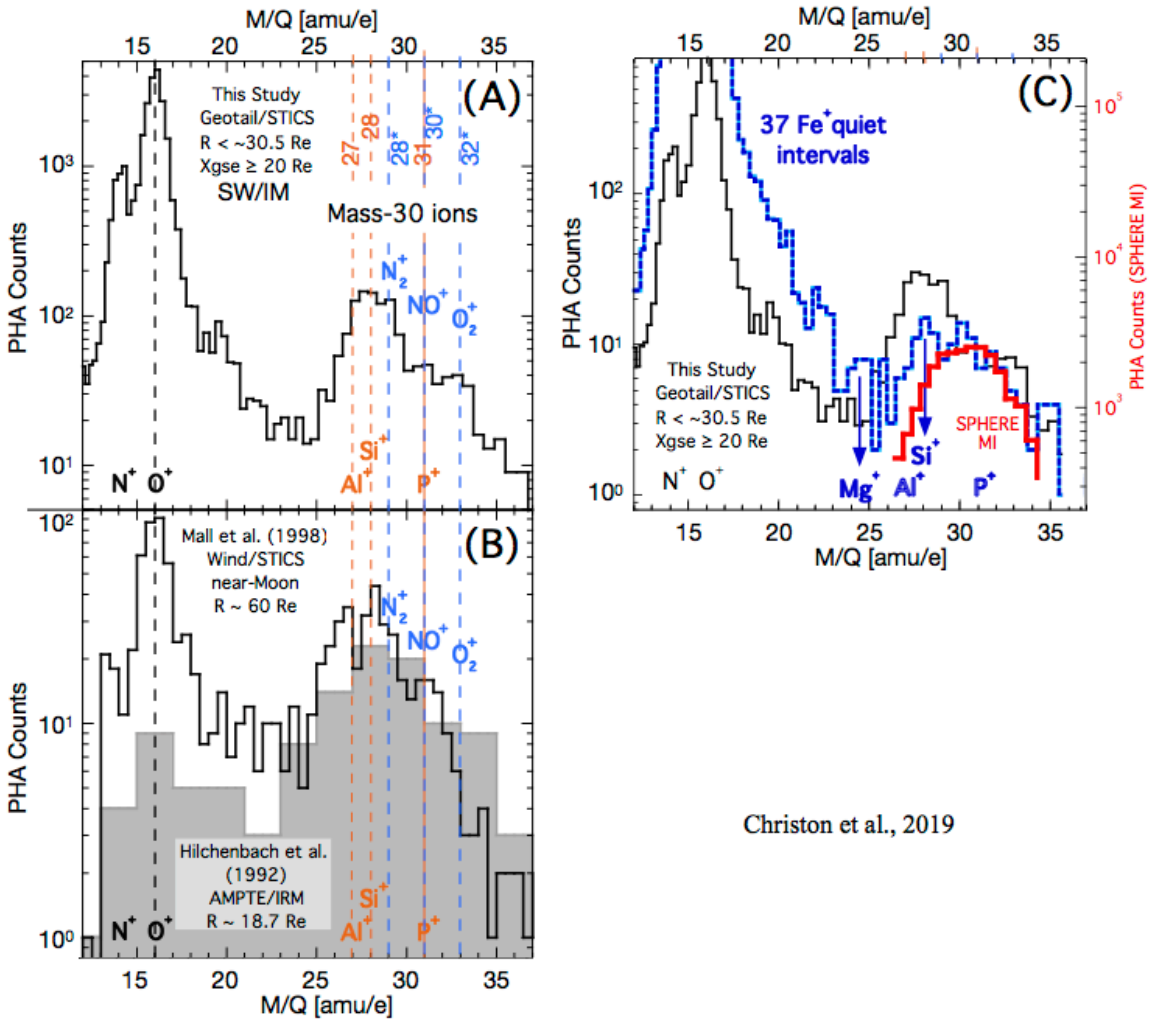

Figure 2.10: <<energeticMass-30_Lunar_Ions.pdf>>

Histograms of ion pulse height analysis (PHAs) events ordered by m/q with the ion species N^+, O^+, and ions around mass 30 (Christon et al., 2019, Fig 9). (A) Geotail/STICS data (~87 - 212 keV/q) at farthest upstream (XGSE = 20 - 30.5 Re). (B) Solid line: Wind/STICS data (~20 - 200 keV/q) near the Moon at >17 lunar radii when Wind is at sunward of the Earth (Mall et al., 1998), and shaded area: AMPTE/IRM data (80 - 226 keV/q) upstream of the bow shock at 18.7 Re from (Hilchenbach et al., 1993). Vertical orange dashed lines, which pass through the peaks of solid lines (both Geotail and Wind data), correspond to the masses for light metallic ions of lunar origin: 27 (Al^+) and/or 28 (Si^+), and 31 (P^+) and/or 32 (S^+). As reference, mass lines for molecular ions (N_2^+=28, NO^+=30, O_2^+=32) are shown by vertical blue dashed lines and mass line for O^+ is shown with black dashed line. Geotail data were obtained over approximately 2 full solar cycles, Wind data were obtained during tail traversals over 1995 - 1997 (solar minimum), and AMPTE data were obtained over 3 months in late-1985 (solar minimum). (C) Geotail/STICS data at, black line: farthest upstream (the same as (A)); red line: the overall magnetosphere data (SPHERE in Figure 1.1) which is dominated by molecular ions; and blue line: the average of 37 orbits (data over 24 hr covering all regions) during low to moderate solar/geomagnetic condition. The data are translated vertically to match values at ≥ 30 - 32 amu/e.

However, the existence of low charge-state heavy ions does not necessarily mean that the excess part of upstream counts beyond the magnetospheric profile (m/q = 22-30) is of lunar origin, because (1) in addition to N_2^+ and CO^+ (m/q = 28), metallic ions at this mass ranges exist in the Earth's upper atmosphere (Na^+ (23), Mg^+ (24), Al^+ (27), and Si^+ (28)) through the ablation of meteoroids (Plane et al., 2016) that forms the mesospheric/thermospheric metal layer, as described in Sect. 2.3, (2) their large gyroradii makes it possible to access the far upstream region by the foreshock (Kronberg et al., 2011) once they reach the space, although lifting these very species to the exobase is extremely difficult (Schunk and Nagy, 2009), and (3) the solar wind may also contain low charge-state heavy ions through the solar wind comet/microdust interaction. Thus, the mass profiles cannot be used to select the lunar ions detected even in the solar wind upstream of Earth (Christon et al., 2019). We come back this problem in §4.1.

3. List of datasets and models that actually detected molecular/metallic ions

As summarized in Section 2, observations of molecular and metallic ions and modelling of their transport are important from many inter-disciplinary aspects. However, these very minor ions are vastly unexplored in the near-Earth space. This is because only a few terrestrial missions have been equipped with dedicated instrumentation capable of separating these molecular and metallic ions, and because even these few dedicated instruments were capable of detecting a limited energy range (cold ions of < 50 eV and energetic ions of ~100 keV) and a limited mass range (≤ 40 amu). Nevertheless, existing data from the past and on-going missions, including those not designed for the required mass separation, are sometimes capable of detecting some of these molecular (very limited for metallic) ions with available tools, although severe limitations exist (sensitivity and energy range, in addition to mass resolution and mass range). In this section, we list these datasets.

3.1 Satellite datasets

Table 3.1 summarizes the available datasets from the magnetospheric and Moon missions by which the heavy molecular or metallic ions are observed. As a reference, we also list the capability of planetary missions with the Earth flyby data in Table 3.2. The table includes the measurement methods because they determine the approximate resolution, sensitivity, and mass-energy ranges. There are roughly three different methods of mass separation for particle instruments: magnetic method, time-of-flight (TOF) method in various formats, and retarding potential analyzer (RPA) method. By combining with the electrostatic analyzer for energy per charge (E/q) selection at the entry of the instrument (by using a perpendicular electric field, only ions with specific energy per charge can follow the curved entry), the magnetic method and the TOF method give m/q and E/q, respectively.

Table 3.1: Terrestrial missions that reported heavy molecular or metallic ions since 1980's

Table 3.1: Terrestrial missions that reported heavy molecular or metallic ions since 1980's

mission/instrument (duration) @where	method	Specification (*1)	what was actually observed	reference (spec + obs m>26)
Cluster/CIS (2001-) @magnetosphere (almost everywhere)	TOF (for > 28 eV) RPA (for low-energy)	0.7 eV/q – 40 keV/q m/q: 1 - 16 (H^+, He^{++}, He^+ O^+)	1 - ~40 amu/q (~50 lower statistics) $m/\Delta m \sim 5 - 7$	Rème et al., 2001. Kistler et al., 2013.
Cluster/RAPID (2001-) @magnetosphere (almost everywhere)	SSD TOF	> 400 keV H, He, and O (C, N, O are not separated)	m>16 up to more than 60	Wilken et al., 2001. Haaland et al., 2020, Haaland et al., 2021.
e-POP/IRMS (2013-2021) @325-1500 km altitude	TOF	< 70 eV/q m/q: 1-64	N^+ and O^+ are separated but not between N_2^+, NO^+, and O_2^+.	Yau et al., 2015. Yau et al., 2016.
Arase/LEPI (2017-present) @Inner magnetosphere	TOF	0.01-25 keV/q m/q: 1 - 40	H^+, He^{++}, He^+, O^{++}, O^+, O_2^+(no separation between N and O) $m/\Delta m \sim 2\text{-}4$	Asamura et al., 2018. Seki et al., 2019. (statistics)
Arase/MEPI (2017-present) @Inner magnetosphere	SSD TOF	7 - 87 keV/q m/q: 1 - 48	H^+, He^{++}, He^+, O^{++}, O^+, O_2^+(no separation between N and O) observed $m/\Delta m \sim 3\text{~}5$	Yokota et al., 2017. Seki et al., 2019. (statistics)
Kaguya/MAP-PACE/IMA (2008-2010) @Moon	LEF-reflectron	10 eV/q – 28 keV/q m/q: 1 - ~ 60 $m/\Delta m \sim 5$ ($m/\Delta m \sim 15$ for reflected ions < 12 keVq)	Na^+, Ca^+, K^+, C^+, Si^+, O^+ are eparated. no molecular ions (due to start foil breaks molecules)	Saito et al., 2010 Yokota et al., 2009.
Geotail/STICS (1992-2022) @magnetosphere	SSD TOF	energy > 200 keV/q for m=30 m: <1 up to ~60-70 amu m/q: <1 up to ~95 amu	10^-2 Fe ions/ 3hr in -> at best once every 900 hr	Christon et al., 2017.
Wind/STICS (1994-) @magnetotail	SSD TOF	6 - 230 keV/q otherwise, the same method as Geotail.	Separate O^+ from Al^+, Si^+	Mall et al., 1998.
Polar/TIDE (1996-2008) @below 8 Re	TOF	0.1-500 eV/q 1 - 40 amu/q $m/\Delta m = 4$	"Significant component of molecular ions in polar wind flux in response to CME"	Moore et al., 1995.
Polar/TIMAS (1996-2008) @below 8 Re	Magnet (double focusing)	15 eV/q – 33 keV/q m: 1 - >32 amu/q $m/\Delta m = 2\text{-}5$	Separate O_2^+ from O+ (but not between N_2^+, NO^+, and O_2^+	Shelley et al., 1995. Lennartson et al., 2000.
Akebono/SMS (1989-2002) @up to 10000 km	RPA	< 50 eV/q m/q: 1 - 40	mostly <20 eV Sometimes separate among N_2^+, NO^+, and O_2^+	Whalen et al. 1990. Yau et al. ,1993. Yau et al., 1998.
AMPTE/CHEM (1984-1989) @Inner magnetosphere	TOF	1-300 keV/q m: <1 up to 90 m/q: <1, 74	Can separate N_2^+, NO^+, and O_2^+	Gloeckler and Hamilton, 1987.
AMPTE/SULEICA (1984-1986) @Inner magnetosphere	TOF		Detected metallic ions (SW charge state)	Stern, 1999. Hilchenback, 2004.
DE-1/RIMS (1981-1984) @568km x 4.6 RE	RPA	< 50 eV/q m/q: 1 - more than 32	Can separate N_2^+, NO^+, and O_2^+	Chappell et al., 1981. Craven et al., 1985.
DE-1/EICS (1981-1991) @568km x 4.6 RE	Magnet	10 eV/q - 17 keV/q m/q = 1 - 150 $m/\Delta m$ ~10	O_2^+, NO^+, N_2^+ separated (in 'drum mode')	Shelley et al. 1981.
MMS/HPCA (2015-present) @Magnetosphere	TOF	1 eV/q - 40 keV/q m/q: 1 - 16 (H^+, He^{++}, He^+, O^{++}, O^+)	$Fe^{6+\text{-}7+}$ by chance but not by search	Young et al., 2016. Gomez et al.,

(*1) energy is with respect to spacecraft potential

(*1) energy is with respect to spacecraft potential

Table 3.2: Planetary missions capable of separating metallic ions and molecular ions of < 100 keV

Table 3.2: Planetary missions capable of separating metallic ions and molecular ions of < 100 keV

mission/instrument with Earth flyby data	metallic ions	molecular ions from atomic ions	Earth flyby?	reference
STEREO/PLASTIC	TOF	0.2-80 keV up to Fe	molecular @Tail 200-300 R_E (2007)	Galvin et al., 2008 Kistler et al., 2010b
Cassini/MIMI-CHEMS	TOF	~10 – 220 keV m: 1 - 80	only ring current ions @ring current (1999)	Christon et al., 2017
JUICE/JDC (Launched 2023)	TOF	1 eV – 35 keV m: 1 - 70 m/Δm=30	Planned: 1 Moon (< 300 km) + 3 Earth (< 10000 km) flybys	Withmann, 2022
JUICE/NIM (Launched 2023)	LEF-reflection	< 10 eV (both neutrals + ions) m: 1 - 1000 m/Δm=800	same as above	Föhn et al., 2021

The TOF method has many variants: foil-type for energetic particles (e.g. Wilken et al., 2001), combination of an electrostatic analyzer with a foil-type TOF unit (e.g. Rème et al., 2001), combination of an electrostatic analyzer with a linear electric field embedded TOF, so called LEF-reflectron unit (e.g. Delcourt et al., 2016), combination of an ELECTROSTATIC ANALYSER with a grazing incidence microchannelplate (MCP) TOF (e.g. Devoto et al., 2008), combination of an ELECTROSTATIC ANALYSER with a gated TOF unit (e.g. Keller et al., 1999), combination of an ELECTROSTATIC ANALYSER with a reflecting surface TOF unit (Wittman, 2022), and straight start-end pair for a simple TOF. For hot plasma of 0.05 - 10 keV energy range, the LEF-reflectron so far provides the highest mass resolution m/∆m. The details of the different measurement methods can be found in a review paper (Wüest et al., 2007). As a general problem with the TOF method using start foil or start surface, some molecular ions are dissociated into atomic ions and atoms there, making the TOF spill out toward longer TOF from the molecular ion peak. This is why the Kaguya data does not include molecular ions. Nevertheless, TOF is the most liable method to separate the mass.

Separation of species within the same mass group (between C, N, and O; between N_2, CO, NO, and O_2) is another important challenge (particularly separation of N and O), but that requires m/∆m > 50 (we call instruments with such capability as mass spectrometer). The same or even better is required for the detection of metallics ions because of the much lower flux compared to the molecular ions.

As summarized in Table 1.1, there is a clear lack of mass spectrometers covering molecular and metallic ions for < 10 keV for near-Earth missions. However, mass spectrometers are regularly included in many deep-space missions, the Moon missions, and solar wind monitoring spacecrafts (like ACE: advanced composition explorer). Among them, Earth-flyby data exist for some mission such as Stereo. The Earth-flyby itself occurred for more missions such as Bepi-Columbo (MPO and MMO), Solar Orbiter, MAVEN, and Rosetta, but heavy ion data were not taken or not useful.

Although excluded from Table 3.1, heavy molecular ions (O_2^+) might be able to be separated from the atomic ions (O^+) by a simple electrostatic analyzer when ions are streaming with a group velocity, such as the far downstream of the Earth. In such cases, different masses correspond to different kinetic energies, and hence the different ion species appear as different groups in an energy-time spectrogram. SOHO/CELIAS (in the Venus magnetotail at 0.3 au) detected heavy ions of Venus tail origin, and well separated C^+ and O^+ (Grünwaldt et al., 1997) by carbon-foil time-of-flight (C-TOF). This kind of rough mass separation has been tried for the ion instrument onboard the THEMIS-ARTEMIS spacecraft, which are in a lunar orbit, when the Moon is within the terrestrial magnetotail and detects downstreaming ions of terrestrial origin. It allowed the separation of H^+ from heavy ions (Poppe et al., 2016a). However, the possible O_2^+ signature was not separated from the O+ signature. To separate them, all ion species must be downstreaming with exactly the same velocity, but this hypothesis breaks down at large distances since heavy ions tend to reach higher flow velocities than protons (Seki et al., 1998).

3.2 Analyses tools to extract molecular/metallic ions in the space missions

Table 3.3 summarizes the analyses tools of these data to extract the molecular and metallic ions. Note that some analyses tools might not be working with modern computer environments.

Table 3.3: Access method of relevant dataset and software with note on availability missions (everybody fill data type and software)

Table 3.3: Access method of relevant dataset and software with note on availability missions (everybody fill data type and software)

mission /instrument	@where	database	notes on the software (basically request-basis)
Cluster/CIS	Magnetosphere	ESA Cluster Science Archive (ASCII) for routine product: https://csa.esac.esa.int/csa-web/ A separate telemetry product ("selected TOF events") for TOF.	IFSI TOF software (IDL source code): Reads level-1 binary files (selected TOF events).
Cluster/Rapid	Magnetosphere	ESA Cluster Science Archive (ASCII) for near-raw product: https://csa.esac.esa.int/csa-web/	Direct event (TOF) Reduced TOF
e-POP/IRM	325-1500 km altitude	ePOP-data.phys.ucalgary.ca	(software for general-user access under development)
Arase/LEPI Arase/MEPI	@ring current and inward	ERG science center (CDF file): https://ergsc.isee.nagoya-u.ac.jp/data_info/erg.shtml.en	(1) IDL SPEDAS for main data products, omcluding TOF histograms. (2) IDL code for MEPI to look at raw PHA data
Kaguya/MAP-PACE IMA	Moon	SELENE data archive	(1) C code by Y. Saito (read binary data) (2) IDL code Y. Harada
Wind/STICS	Magnetotail	NASA cdaweb (web interface) and spdf (CDF file) https://spdf.gsfc.nasa.gov/pub/data/wind/sms/l2/	
Polar/TIDE	Magnetosphere below 8 R_E	Level-Zero Telemetry Files hosted by the GSFC https://spdf.gsfc.nasa.gov/pub/data/polar/ ftps://pwgdata.gsfc.nasa.gov/pub/compressed/po/tid/	
Polar/TIMAS	Magnetosphere below 8 R_E	POLAR TIMAS H1 and H2 high resolution data: https://lasp.colorado.edu/timas/info/h12-data/h12-data.html Summary data: https://lasp.colorado.edu/timas/data/summary/	https://lasp.colorado.edu/timas/info/h12-data/make_h2.pro https://lasp.colorado.edu/timas/info/h12-data/make_h2_cdf.pro
Geotail/STICS	Outer magnetosphere	summary plots available at http://sd-www.jhuapl.edu/Geotail/Years_dir.html	code developed by S. Nylund and S. Christon
Akebono/SMS	Magnetosphere below 10000 km	JAXA/ISAS Data Archives and Transmission System (DARTS): https://darts.isas.jaxa.jp/stp/akebono/SMS.html	under conversion to public database
AMPTE/CHEM	Inner magnetosphere	APL AMPTE site: http://sd-www.jhuapl.edu/AMPTE/chem/index.html NASA spdf site: https://spdf.gsfc.nasa.gov/pub/data/ampte/cce/	(1) Python code at UNH reading the CHEM FITS files (2) PHAFLUX fortran code calculates fluxes from PHA events
AMPTE/SULEICA	Inner magnetosphere	data is not easy to access	
DE-1/RIMS	Inner magnetosphere	NASA spdf site: https://spdf.gsfc.nasa.gov/pub/data/de/de1/plasma_rims/	summary spectra https://spdf.gsfc.nasa.gov/pub/data/de/de1/plasma_rims/de1_rims_summary-spectrograms_nasa-tm-19950009193.pdf
DE-1/EICS	Inner magnetosphere	NASA spdf site: https://spdf.gsfc.nasa.gov/pub/data/de/de1/particles_eics/	
MMS/HPCA	equatorial magnetosphere	NASA cdfweb and spdf site: https://spdf.gsfc.nasa.gov/pub/data/mms/mms1/hpca/srvy/l2/tof-counts/ https://spdf.gsfc.nasa.gov/pub/data/mms/mms2/hpca/srvy/l2/tof-counts/ so on	TOF at NASA cdfweb https://cdaweb.gsfc.nasa.gov/cgi-bin/eval1.cgi

3.3 Mesospheric and ionospheric dataset including sounding rocket

As the source region's information, datasets for the metal layers and ionospheric molecular ions are useful. Since they can be observed from the ground and sounding rocket in addition to some spaceborne observations (e.g., limb scanning), there are many databases, as summarized in Sect 2.3.2. Table 3.4 summarizes observation methods with some examples. We just show examples for the databases because most of them are not publicly available or the database is not internationally organized

Table 3.4: Available method of monitoring the uplift of the molecular and metallic ions in the ionosphere and mesosphere

method	where	examples	species	data availability
Resonance-Scattering Lidar	mesosphere - 80 km up to 200 km (only sometimes Na)	ALOMAR (1*): Tromsø for Na (*2):	Fe, Na, Ni, K, Ca (Mg cannot be observed at 285 nm because of the stratospheric ozone layer) Na from 2010-2019 at Tromsø	Plane et al. (2015) CEDAW database (http://cedar.openmadrigal.org/) has list but no "open" data site. Data (Na) at Tromsø upon request
ion/neutral mass spectrometer (sounding rocket)	mainly E-layer below 120 km	total < 10 for metallic ions (*3)	few paper/rockets, but not more knowledge than Lidar data (Plane's paper)	Kopp (1997) Grebowsky and Aikin (2002)
ion/neutral mass spectrometer (satellite)	< 30° lat < 400 km alt	Ogo 6, AE-C, AE-D,	molecular results are already included in standard model	
Satellite: limb optical	< 400 km alt	Odin/OSIRIS, (TIMED), Envisat/SCIAMACHY	Mg^+, Mg, Na and K	On request to University of Leeds (W. Feng)

*1: https://www.iap-kborn.de/en/research/department-optical-soundings-and-sounding-rockets/instruments-and-models/metal-lidar-kuehlungsborn/

*2: https://www.isee.nagoya-u.ac.jp/~nozawa/indexlidardata.html

*3: One example from molecular detection, one example from metallic detection, and example of obtaining extra information from Lidar observation of > 130 km

3.4 Modelling of contribution from meteor and space debris through deposition to the metal layer

Table 3.5: Models relevant to upflow of molecular and metallic ions reaching the exobase

Name	Description	Citation/availability
SAMI-3	Predict metallic ion in the ionosphere (Huba's model includes transport to 600 km)	
WACCM	Metallic ions in the ionosphere.	Feng et al., 2013; Wu et al., 2021
CABMOD	Examine differential ablation of meteoroids and deposition as a function of altitude and orbital position	Bones et. al. 2019, Vondrak et. al. 2008, Carrillo-Sanchez et. al. 2020. Data available on request(*1).
WACCM-X	Numerical model spanning the range of altitude from the Earth's surface to the upper thermosphere.	Wu et al., 2021 www2.hao.ucar.edu/ modeling/waccm-x
ORSAT	Predict the re-entry survivability of satellite and launch vehicle upper stage components.	Dobarco-Otero et. al. 2005 orbitaldebris.jsc.nasa.gov/reentry/ orsat.html
SCARAB	Simulate the re-entry of a satellite in detail.	Koppenwallner et. al. 2005 www.htg-gmbh.com/en/ htg-gmbh/software/scarab/
MASTER	Assess the debris or meteoroid flux imparted on a spacecraft on an arbitrary earth orbit.	Flegel et. al. 2009 sdup.esoc.esa.int/
LEGEND	Three-dimensional debris evolutionary model for long-term debris environment projection.	Liou et.al 2004 orbitaldebris.jsc.nasa.gov/ modeling/legend.html
-	A dynamical model of the sporadic meteoroid complex.	Wiegert et al., 2009
-	Fluid model (simulation) in the ionosphere	Shinagawa and Oyama, 2006
	Polar wind outflow model for < 300 km – > 8000 km	Glocer A (GFSC/Mishigan)

*1 Request to Juan Diego Carrillo Sanchez (juandiego.carrillosanchez@nasa.gov)

Table 3.5 summarizes models relevant to upflow of molecular and metallic ions reaching the exobase. The table also includes models of space debris as these could contribute to the mesospheric metal layer if their ablation altitudes are high enough. These models provide the distribution of the modeled species beyond what the empirical International Reference Ionosphere (IRI) model provides.

For the ionospheric and mesospheric heavy ions to be lifted, a common model of the neutral convection and electromagnetic fields to estimate the dynamics of the atomic ions can be used for both the molecular and metallic ions. Note that the available models still underestimate the upward convection in the polar region (see Shinagawa and Oyama, 2006). Even the solar flare effect, i.e., the heating of the ionosphere by the flare-related radiation, cannot reproduce the extremely high convection that is observed (Yamauchi et al., 2020). Still the existing models are a good start to estimate the upper limit and lower limit of the flux of metallic ions into the magnetosphere.

Since the ionospheric metal layer is most likely formed by the ablation of meteoroids, a current update to the ablation modeling is relevant. Then, we need an empirical model of lifting (expanding) the metal layer to the ionospheric altitude (up to > 120 km) such that an ionospheric/thermospheric model of upflow can be applied. Finally, we note that it is difficult to model once the molecular and metallic ions reach the exobase, because wave activity is required to lift them to the region where sufficient energization is expected.

4. Merit of combining data from different sources and models

In this section, we show some examples of the merit of combining data and knowledge from different sources.

4.1 Moon contribution to energetic (> 100 keV) ions

As summarized in Sect. 2.4, the mass spectrum of the very heavy ions in the Earth's upstream region while downstream of the Moon is consistent with that coming from the Moon. However, this is yet not sufficient to state that majority are of lunar origin, as discussed in Sect. 2.4.4. We revisit this problem by combining the Geotail/STICS observation with the other data such as the Moon location and the solar wind monitor.

4.1.1 Statistics of Energetic ions (Geotail)

Christon et al. (2020) examined the Geotail/STICS counts in term of the Moon location. To overcome the low count-rate problem (0-1 count per day), they integrated the data over nearly 20 years of Geotail data, and further integrated the data over the location for both the Geotail (four regions which are the same as Figure 2.1) and the Moon (six locations: the upstream near the new Moon, four sides, and the downstream near full Moon). Figure 4.1 shows the results. For example, sector 3 in Figure 4.1a shows the result of collecting all cases when the Moon is located sunward of Geotail's nominal orbital XGSE-YGSE range.

Figures 4.1b and 4.1c (Christon et al., 2020, Fig. 7) show the results for high Kp (≥ 3) and low Kp (≤ 2) cases, respectively. For both Kp cases, heavy ion counts (for m/q ≥ 28, i.e., molecular, metallic ions) in the upstream solar wind (SW/IM in the figure) show a peak at LLT sector 3 (5-day period near the new Moon), with a widening of the peak for higher Kp. This peak at LLT sector 3 is less obvious for the magnetosheath (SHEATH in the Figure 4.1) and there is nearly no peak at sector 3 in the magnetosphere (SPHERE) and plasma lobe (LOBE). Considering that heavy ion flux of m/q ≥ 28 escaping from the Earth (almost all are molecular ion) is nearly zero for low Kp, all these results indicate that Moon origin metallic ions are the major heavy (m/q > 20) ions in the upstream region. Here, the increase of the ion counts for high Kp (which generally means stronger solar wind) agrees with the general increase of both the Earth-origin molecular ion flux (not dependent on the

Moon location, and seen in all panels) and the Moon origin heavy ion flux (peak at LLT sector 3).

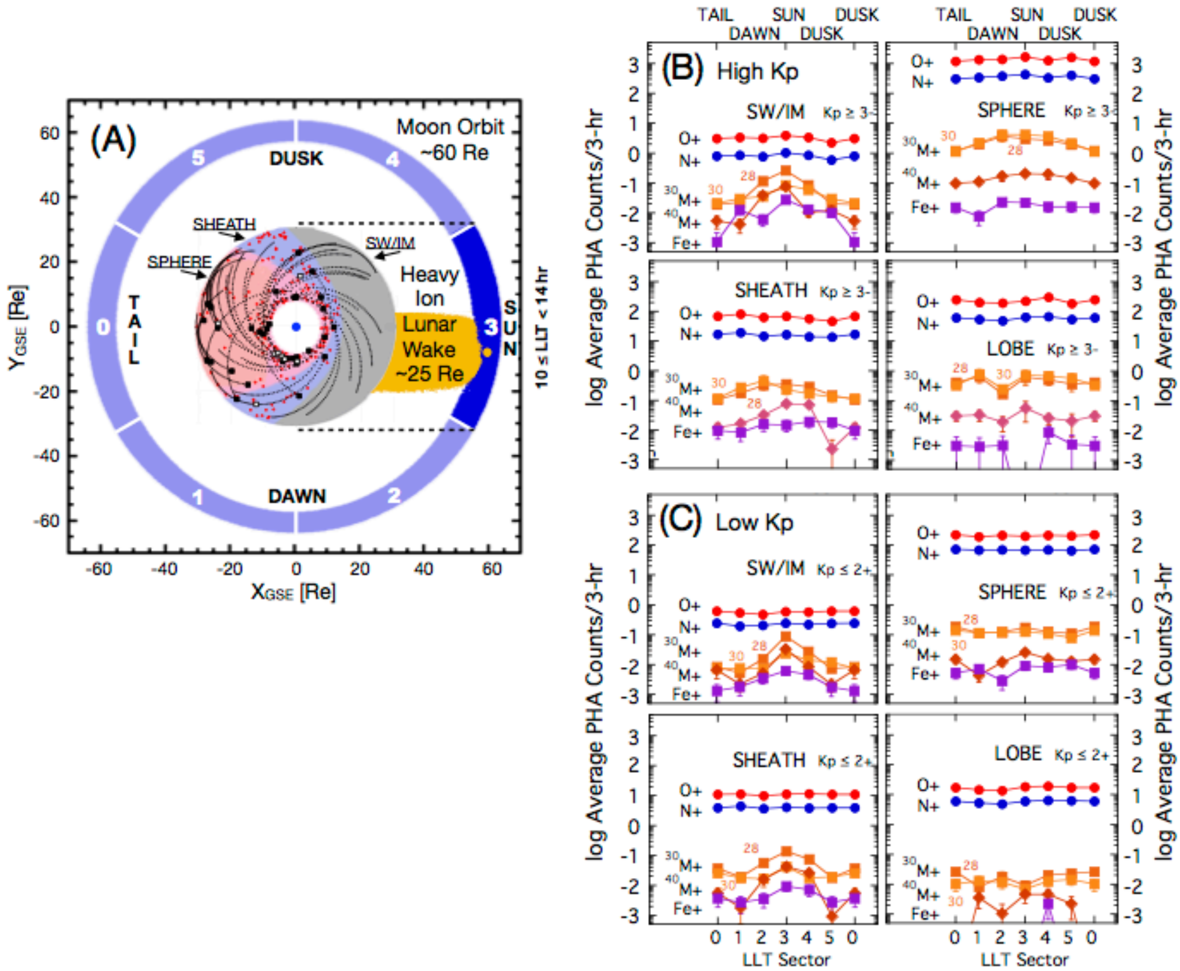

Figure 4.1: <<Lunar ion wake and local time.pdf>>

(A) A sketch of the Earth (blue dot at the center), the Moon's orbital range (~60 Re), and Geotail orbital range (~9 < R < 35 Re). Two spatial criteria for considering possible lunar pickup ion influence in Geotail/STICS suprathermal (~87 - 212 keV/e) ion measurements are the lunar local time (LLT) and the "Lunar-ion Wake". LLT marks the orbital location of the Moon with respect to the Earth-Sun line. For example, 10 hours ≤ LLT ≤ 14 hours (the sector marked as 3 in the figure) corresponds to the Moon location sunward of Geotail's nominal orbital XGSE -YGSE range. The "Lunar-ion Wake" (different from fluid dynamical "wake") drawn here (~25 Re width) is the region where very heavy ions of lunar origin (e.g., CO^{2+} or Fe^{+}) are expected exist in the nominal IMF at 1 au (~7 - 9 nT). Selected segments of Geotail orbits (dotted traces near Earth) terminate when an Fe^{+} was observed during low to moderate solar and geomagnetic conditions. White (black) squares indicate Fe^{+} observations obtained when the Moon was (not) in LLT-sector 3. Red dots show other measured Fe^{+} data. Three different regions (magnetosphere: "SPHERE", magnetosheath: SHEATH", and upstream of bow shock "SW/IM") are identified by different colours. The plasma lobe ("LOBE in Figure 1.1) overlies the SPHERE and not shown here. (B) Average counts/3-hours of low charge state ions at four different regions during Kp ≥ 3 and (C) those during Kp ≤ 2.

The results also indicate that unless the Moon is directly upstream of the Earth (i.e., except LLT sector 3), the magnetospheric heavy (m/q > 20: metallic) ions are mainly provided from the Earth with minor contribution from the Moon most of the time. Both contributions can be comparable if we limit to a 5-day average near new Moons because the peak values for m/q > 20 ions near LLT sector 3 are the same level between in the upstream (SW/IM and SHEATH) and in the magnetosphere (SPHERE). The enhancement near LLT sector 3 during high Kp suggests that there might exist periods (e.g., for Kp ≥ 5) when the metallic ions of lunar origin are found more than those from the Earth origin.

4.1.2 Case studies (combining Geotail and ACE)

To obtain a more concrete view of the Moon-origin ions in the magnetosphere with the existing dataset of very low count rates (0-1 count per day for singly-charged metallic ions of mass more than 33), we need to carefully select the conditions when the solar wind flux significantly increased while the Moon is upstream. Here we show the usefulness of combining different datasets (Geotail, ACE, and SOHO) for such a study. We selected CME-driven interplanetary shock evens (from list made by SOHO/CELIAS proton monitor) with significant flux increase of iron ion (Fe^{n+}) by three order of magnitude (to over 100 cm^{-2} s^{-1} str^{-1} MeV^{-1}) in ACE/ULEIS instrument) within two days from new Moon. Out of them, half-day resolution QL of Geotail/STICS is available for 10 events: 6 events when Geotail is located within the lunar wake, and 4 events outside the lunar wake.

For these “best” events, we counted all half-day counts when the interplanetary shock arrived and compared them from those when the Geotail was in the same region one orbit before (about 5 days before). Here, the region is judged from the orbit, low-energy particle (LEP) data and STICS data. Table 4.1 summarizes the results. The third column lists the change in the half-day triple-coincidence counts for m>34 and m/q≥34 (inside parenthesis are additional counts that satisfies m>20 and m/q≥34). For all cases, counts during one orbit before the CME arrival (5 days before, i.e., Geotail is outside the lunar wake) are zero. However, after the arrival of the interplanetary shock, the Geotail sometime detects counts corresponding to the metallic ions apparently heavier than O_2^+ if and only if the Geotail is located within the lunar wake.

Table 4.3: Change in the half-day integrated counts of low charge-state metallic ions observed by Geotail/STICS.

shock timing	location*3	triple: m>34	double: m/q 39-46
2000-04-06, 16:01	SH	0 to 1 (0 to 2)	0 to 41
2000-11-26, 07:15	SW	0 to 0 (0 to 0)	0-1 to 3
2002-09-07, 15:54	SW	0 to 1 (0 to 0)	0 to 7
2003-05-29, 11:52	SH	0 to 4 (0 to 0)	2 to 42
2004-01-22, 01:10	SH to SPH	0 to 11 (1 to 8)	201 to 463
2005-09-02*1, 13:32	SW	0 to 0 (0 to 0)	0 to 0
2000-10-28, 09:01	SW*4	0 to 2 (0 to 0)	2-4 to 2-3
2001-01-23, 10:15	SPH*4	0 to 0 (0 to 0)	243 to 193
2003-10-24*2, 14:47	SW*4	0 to 0 (0 to 0)	0 to 0
2004-09-13, 19:29	SW*4	0 to 0 (0 to 0)	0-1 to 1-3

*1: Peak of Aurigids meteor shower was 2005-08-31
*2: Peak of Orionids meteor shower was 2003-10-21
*3: SH: magnetosheath, SW: solar wind, SPH magnetosphere
*4: Geotail was not in the wake region for this time interval.

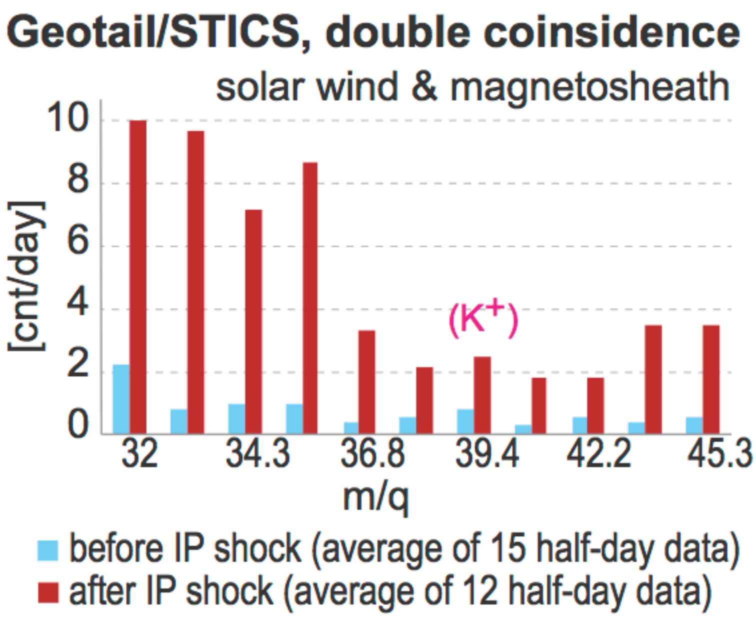

Figure 4.2: <m/q_STICS.ai> Mass-per-charge (m/q) distribution of double coincidence counts for mass ≥32 obtained by Geotail/STICS. Half-day data inside the solar wind or magnetosheath before and after the interplanetary (IP) shocks with highest Fe^{n+} fluxes listed in table 4.1 (total 8 events) are averaged. For each event, maximum two half-day data (if staying long within the solar wind) are included. A small peak is Spread of the major peak at around m/q=39 sticks out from the wide spread from m/q ≈ 32.

Since the majority of these cases were observed when the Geotail was in the solar wind, the result is consistent with the hypothesis that low charge-state heavy metallic ions in the upstream region seen in Figure 2.1 are mostly from the Moon when the solar wind had favorable conditions for ejecting the lunar elements (sputtering or charge exchange). This is more obvious in the double-coincidence counts for m/q ≥39 during the same half-day periods (fourth column of Table 4.3). Here, we take m/q ≥39 because its peak (corresponding to potassium ion K^+) is well separated from mass 32 (S^+ or P^+ rather than O_2^+ because it is most likely the lunar origin), as shown in Figure 4.2.

Thus, just combining the available summary data of the Geotail/STICS and a solar wind monitor can provide more insight on the metallic ions in the upstream region, and so it is worthwhile to try further combinations with the other datasets (e.g., geomagnetic activity) to examine, for example, the relative importance compared to the Earth origin ions. Ideally, we need new observations using dedicated instruments with much higher sensitivity for high mass (cf. Sect. 5). This is particularly important for the magnetospheric metallic ions because the ionospheric or mesospheric can also supply a significant amount and easily hide the lunar signal without specifying the external condition. However, the total Moon-origin ion flux might not be negligible when the Moon is upstream and the geomagnetic activity is moderate or quiet.

4.1.3 Low-energy ions near the Moon (Kaguya or Change-4, combining with ACE)
For the source environment near the Moon, it is again useful to compare the lunar ion flux leaving the Moon with the solar wind. With the capability of detecting these ions, Kaguya observed notable increase of the Moon-origin ions around the Moon when CIRs arrived at the Moon, as mentioned in Sect 2.4.3. Unfortunately, the operation of Kaguya/IMA was only from 2008 to early 2009, i.e., during the lowest solar activity in the space age (deepest minimum), and only very few CIRs of minor intensity occurred. This is not easy because such a study requires a good constellation of Kaguya (the orbit plane with respect to the Moon-Earth line changes depending on the Earth's season), a magnetospheric satellite (in the magnetosphere and lunar wake) and the Moon (e.g., at few days before and after new Moons) during the CIR arrival. Probably for these reasons, we could not find

a notable correlation between the Kaguya's soil-origin ion counts (time resolution of 1 day) and Cluster CODIF data.

Other than CMEs or CIRs, the Moon is exposed to high upstream plasma energy in the Earth's plasma lobe and mantle region because of the high flux of terrestrial escaping O^+ (Slapak et al., 2017; Yamauchi, 2019) when the Moon is in the magnetotail for about 5 days every month. For the Earth's plasma sheet, the Moon is exposed to hot (high energy) ions including terrestrial O^+, but the Kaguya observations for such periods are too short for the sensitivity of IMA instrument to examine the expected increase of sputtering inside the plasma sheet.

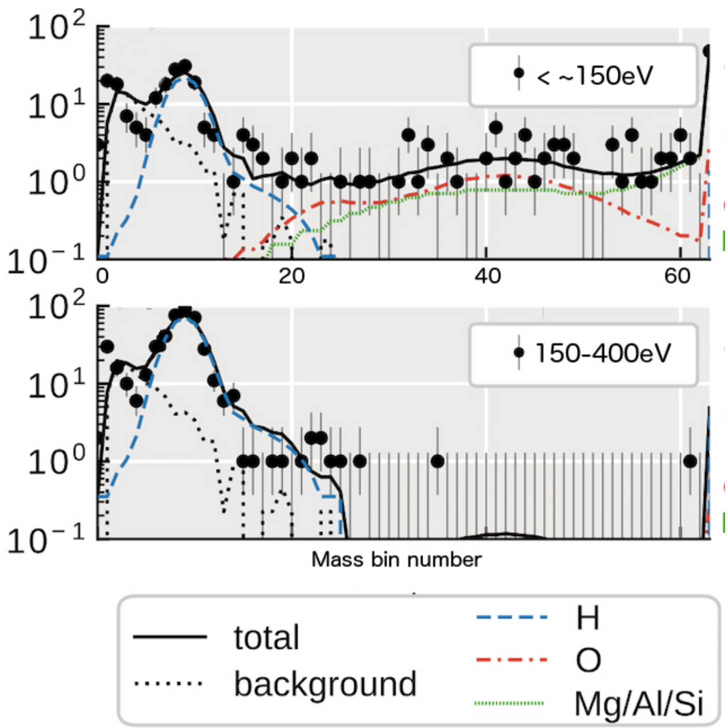

Figure 4.3: <<Asan2020egu2>> Energy-integrated mass spectrum of neutrals coming from the lunar surface observed by Chang'e4/ASAN during January - September 2019. The colored curves are modelled values assuming specific species. Upper: energy < 150 eV is integrated. Lower: energy > 150-400 eV are integrated. Comparing them, the high mass signals for < 150 eV indicates the heavy species.

Finally, the Chang'e-4 lunar rover is equipped with an ion/neutral instrument, the Advanced Small Analyzer for Neutrals: ASAN (Wieser et al., 2020a). ASAN is capable of separating the heavy species from proton/hydrogen (Wieser et al., 2020b), and is still operating after 5 years on the Moon surface since 2019. Including the FOV toward the lunar surface, ASAN can distinguish between the sputtering component and reflecting component based on energy analysis of the registered neutrals (Xie et al. 2021). Although its operation in many short (10-20 min) sessions give a total of only several hours every month, the much longer duration of the mission covers the inclining phase of solar cycle 25, and has already experienced several strong CMEs such as the one in December 2020. The count rate is marginally sufficient to separate H^+ and other elements (O^+ and heavier together), but it is still useful to examine the increase of sputtering heavy ions by the CME passage. Analysis is on-going.

4.2 Ionospheric origin of low-energy heavy molecular ions (in-situ observations)

4.2.1. Recent observations above the ionosphere

With the ability to measure low-energy ions up to ~100 eV, which is sufficient for measuring most ion upflow and outflow events in the full altitude range of the CASSIOPE (Swarm-E) satellite (perigee 325 km and initial apogee 1500 km), the e-POP/IRM instrument is capable of separating the heavy molecular ions from the N^+ and O^+ (Yau et al., 2015, 2016) in the topside ionosphere. It covers both the high-latitude (around the dayside cusp) outflow region and the auroral and sub-auroral outflow region. In a preliminary study (Foss, 2019; Foss et al., to be submitted 2024), upflow of the heavy molecular ion above the ionosphere are often detected on the equatorward side of the auroral ion outflow region, especially during geomagnetic active periods, in addition to in the dayside polar cap.

Figure 4.4 shows one example of the e-POP/IRM observation in the dayside at ~1400 km altitude when Kp = 3 and Dst =- 37 nT during the recovery phase of a moderate geomagnetic storm on 29 August 2014 (Dst minimum - 63 nT). The vertical axis is the time of arrival (TOA) at the detector which represents the TOF, and molecular ions correspond to TOA ~ 80-100. Both the count and TOA increased during 08:00:55 - 08:01:25 UT, at which the spacecraft is in the dayside at around ~ 72° magnetic latitude and ~ 1400 km altitude. This means that the molecular ions appeared in addition to O^+. Thus, e-POP can separate the heavy molecular ions from the atomic ions.

Figure 4.5 shows another example of the e-POP/IRM observation in the nightside at the altitude of 1360 km when Kp = 6+ and Dst = -87 nT during a major geomagnetic storm (Dst minimum -130 nT). Both the count and TOA suddenly increased at around 16:15:30 UT in the evening sub-auroral latidude (20.4 MLT, 53° Mlat.) indicating a mixture of molecular ions and atomic ions, with continued high count in the TOA range corresponding to atomic ions. This example shows that, unlike Akebono observation at higher altitude, heavy molecular ions can reach the topside ionosphere in the nightside sub-auroral region, at the equatorward side of the atomic ion outflow region in the auroral region.

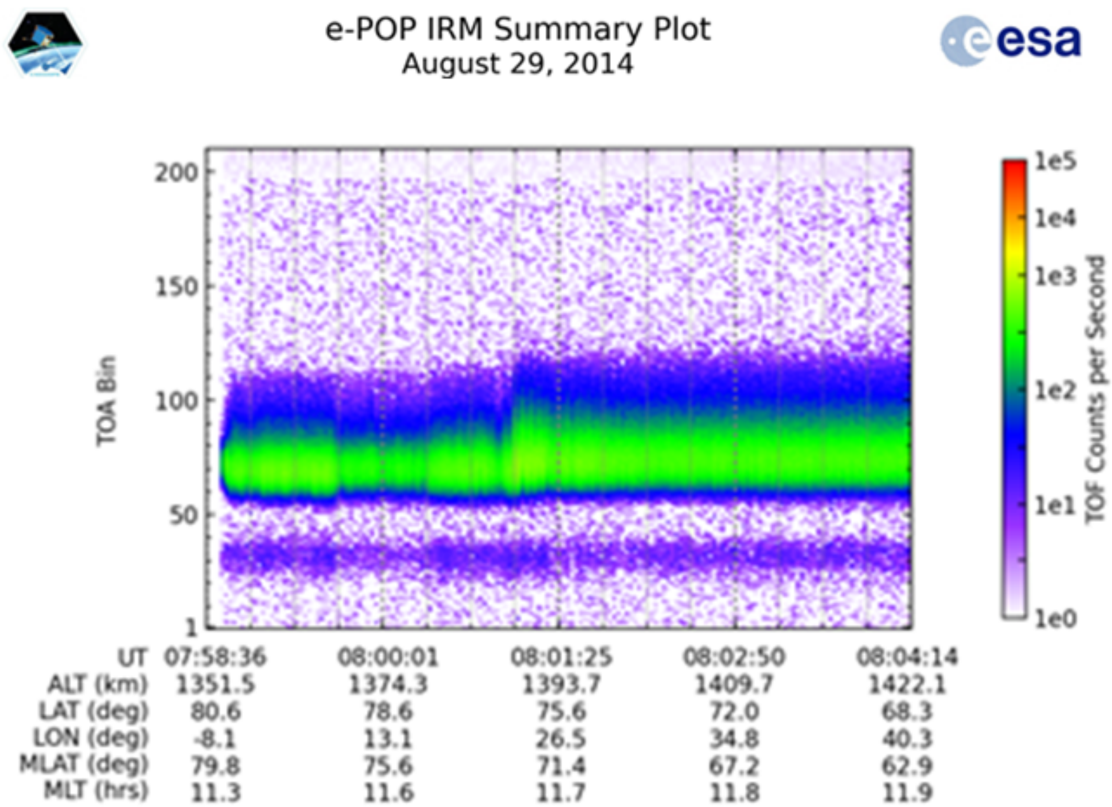

Figure 4.4 <ePOP-MI_sample_cut>: TOF-time spectrogram of observed ion count rates on e-POP during the recovery phase of a magnetic storm on 29 August 2014. Vertical axis is time of arrival at detector (TOA) which represents the TOF, and molecular ions correspond to TOA ~ 80-100.

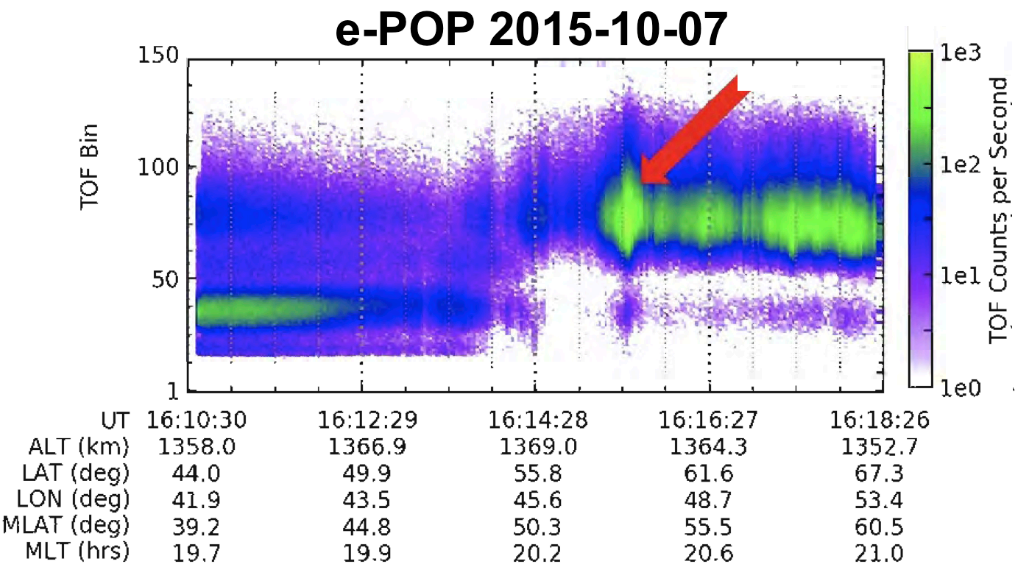

Figure 4.5 <ePOP_2015_1007>: Same as Figure 4.4 but for on 7 October 2015. This traversal took place just before the lidar event in Figure 4.12a.

The observed low- and mid-latitude events are predominantly low- or medium-flux events at low altitudes (<800 km). We here note that the lowest-latitude (<10° MLAT) events at 16-22 MLT are believed to be mostly associated with the Appleton anomaly and not part of the molecular ion upflow population. Otherwise, the other low-latitude detection of the molecular ions (particularly for < 800 km altitude) suggests that these molecular ions are convected equatorward in the ionosphere after originating at higher (auroral) latitudes. Thus, the ionospheric convection (both equatorward and upward) can be strong enough to transport heavy molecular ions to very low latitudes before they reach the topside ionosphere or before they undergo dissociative recombination to form a pair of neutral atoms (see Sect. 2.2.2).

The detection of molecular ions on the nightside by e-POP at 1400 km answers one of the questions in Sect. 2.2: at which altitude do the molecular ion upflows begin to disappear in the nightside outflow region where atomic ion upflows are detected at much higher altitudes such as Akebono and Polar? The difference in the observed ion upflows between molecular ions and atomic ions starts at about 1200 km altitude on the nightside. There are two possibilities for the cause of such difference between the molecular ions and atomic ions: insufficient pre-energization to reach the altitude at which the transverse ion energization starts (above 2000 km; Whalen et al., 1990; 1991), and the absence of main energization at the latitude of molecular ion formation and upflow.

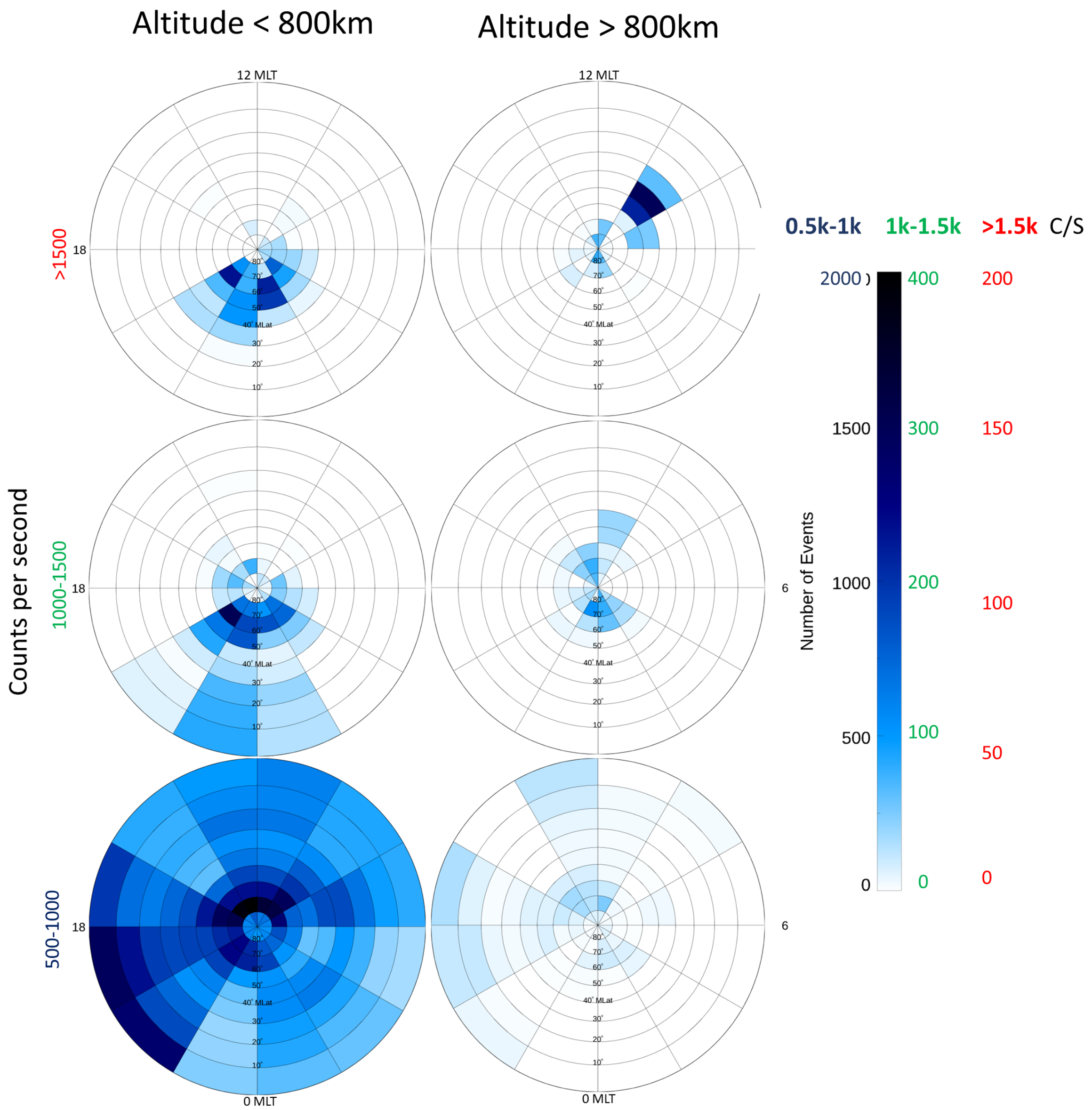

Figure 4.6: Statistical distributions of molecular ion detection observed by e-POP as a function of MLT and magnetic latitude (MLAT) below (left) and above (right) 800 km altitude, respectively; top to bottom: peak count rate >1500, = 1000-1500, and = 500-1000 counts-per-second, respectively. (Courtesy of V. Foss, to be submitted 2024)

For the first scenario, the pre-energization that is required above e-POP altitude for a molecular ion to reach 4000 km (2500 km) altitude must be less than 4 eV (2 eV) in the field-aligned direction, which is double (about the same as) the energy required from 500 km altitude to initial e-POP apogee (1500 km altitude) according to Table 2.1 in Sect. 2.

For the second scenario, energization of ions between the e-POP altitude and Akebono altitude including energization of all types must be less than 7 eV in the field-aligned direction. Neither of these two possibilities can be examined due to the lack of dedicated instruments for observing molecular ions in the magnetosphere.

4.2.2. Magnetospheric molecular ion measurements by non-optimized instruments

There are instruments that are not optimized for separating molecular ions from atomic ions, but still able to identify them under certain conditions, particularly if the ion outflow is very strong. We here show an example from the Cluster CODIF instrument.

The CODIF ion mass spectrometer onboard Cluster, with a mass resolution of $m/\Delta m \approx 5–7$ (Rème et al., 2001), was not designed to separate molecular NO-group ions and atomic CNO-group ions. Ions lose energy when going through the thin carbon foil in the instrument at the start of the time-of-flight section. This energy straggling in the foil leads to a long tail in the time-of-flight distribution of heavy ions. Therefore, the time-of-flight peak of the heavy molecular ions on CODIF overlaps with the tail of the O^+ peak, making it difficult to separate the molecular ions. Usually, the molecular ion counts are negligible compared to the O^+ tail. Therefore, the molecular ion counts have not been counted.

However, during some strong events, the flux of the molecular ions occasionally becomes high enough to have a separate peak above the oxygen tail in the TOF region where the molecular ion peak should appear (Dandouras et al., in preparation, 2024), as shown in Figure 4.7. In such cases, the molecular ions can be distinguished. By fitting multiple peaks to the time-of-flight spectra, the abundance of molecular ions can also be estimated.

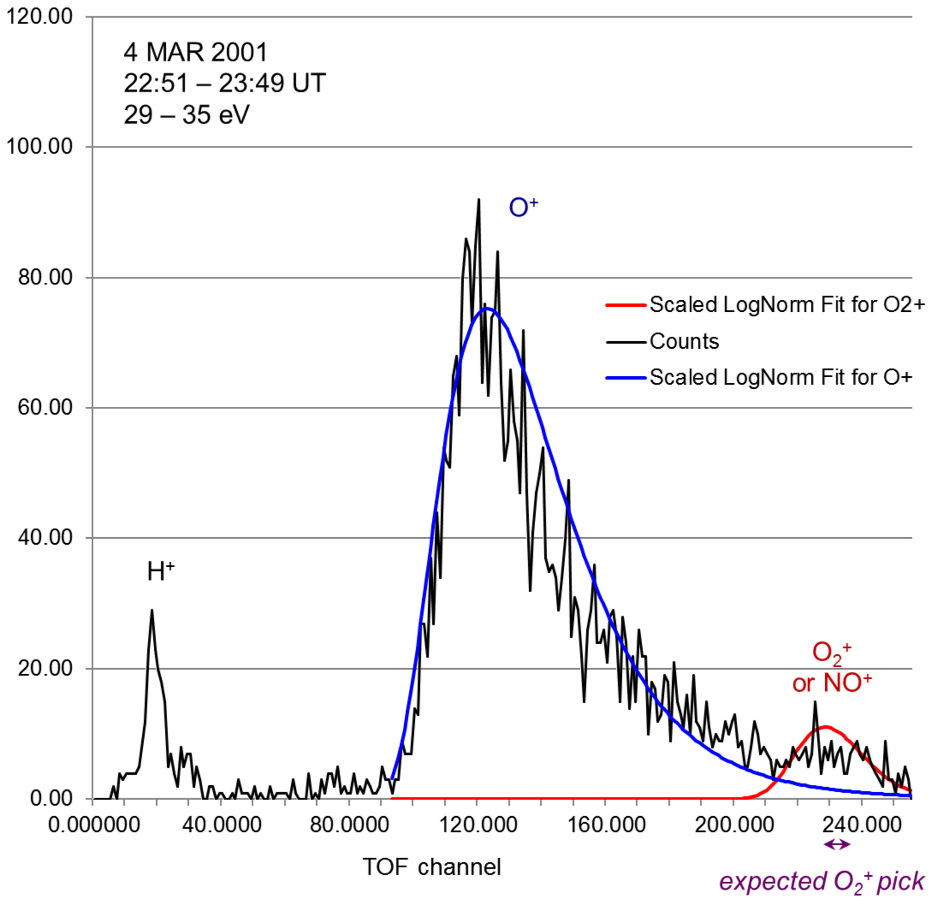

Figure 4.7 <Iannis_Figure 4a_CIS TOF fit> : Time-of-flight (TOF) histogram for the 29 – 35 eV ions detected by CODIF onboard Cluster on 4 March 2001 between 22:51 and 23:49 UT above the southern polar cap, while observing an upwelling ion beam. The blue and red curves represent the simulation results for atomic O^+ (blue curve) and fragments of molecular O_2^+ (red curve) ions entering the TOF section of the instrument, after their passage through the carbon foil where the molecular ions fragment (SRIM software simulation). The upwelling ion beam is dominated by the O^+ ions, but the instrument TOF data also show the existence of a weak O_2^+ (or NO^+) population.

Figure 4.8 shows one Cluster pass through the inner magnetosphere and over the polar cap during the 2003 Halloween storm. The top three panels show the H^+ energy spectrum and the pitch angle distributions for two energy ranges. The next three panels show the same parameters for O^+. Two clear spatial regions can be distinguished. From the beginning of the plot until ~15:15, Cluster is in the closed field line region of the inner magnetosphere. After 15:15 UT, it is moving out over the polar cap, and observing a narrow distribution of O^+ ions that is convecting tailward, likely from the cusp region.

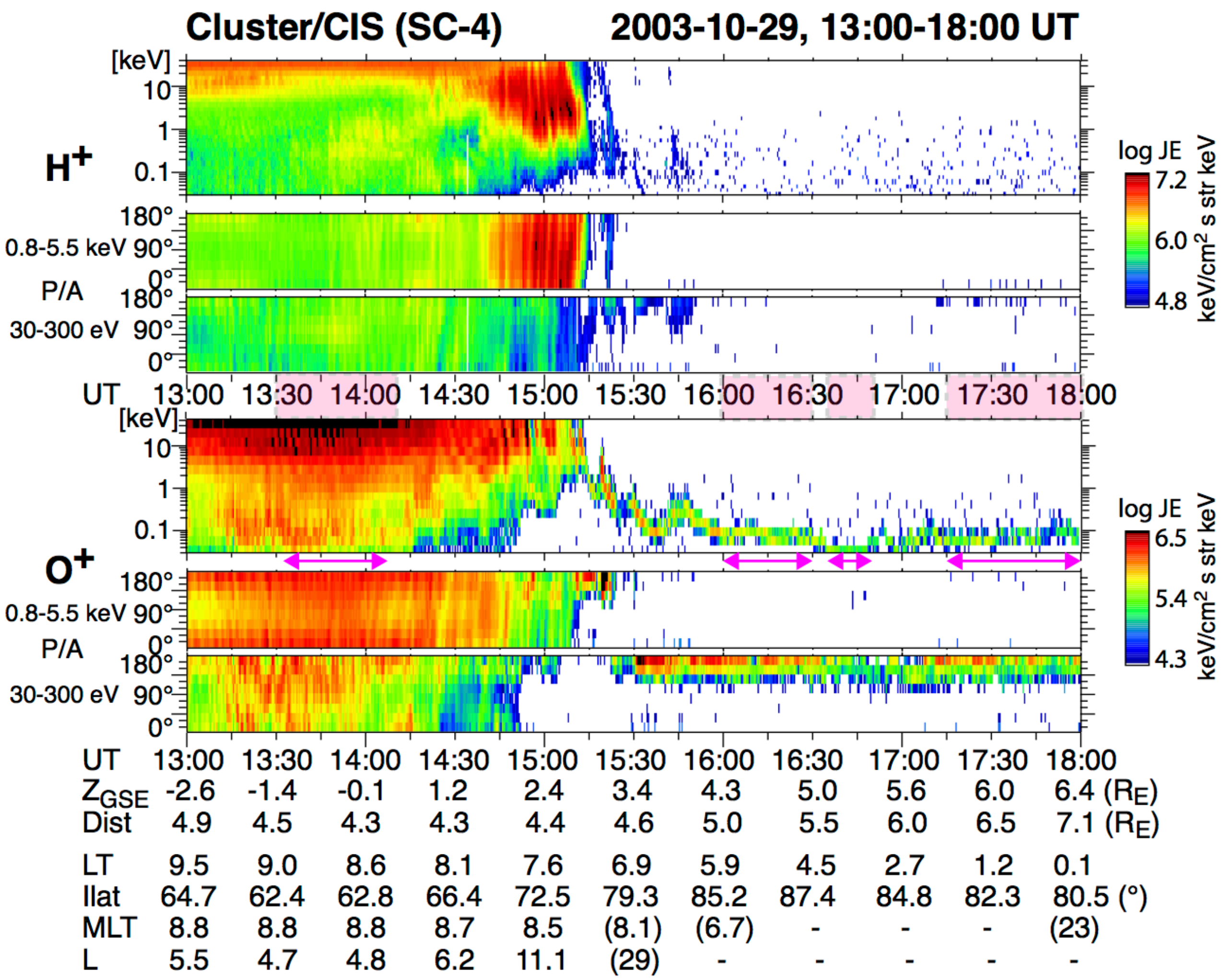

Figure 4.8 <HO_20031029b>: Custer CIS/CODIF observation of Halloween storm on 29 October 2003. Energy-time and pitch angle-time spectrograms for H^+ (upper panels) and for heavy ions (labeled as O^+) are displayed. The periods indicated by horizontal arrows and hatches correspond to periods when the time-of-flight distributions were obtained, as shown in Figure 4.8 (16:00-16:30 UT, 16:35-16:50 UT, and 17:15-18:00 UT) and Figure 10 (13:30-14:10 UT), respectively.

For ions flowing over the polar cap where solar wind electric field drives ion convection perpendicular to the magnetic field, the combination of the field-aligned upflow and this perpendicular convection leads to the “velocity filter effect”, in which the ions become spatially separated by their velocity. In Figure 4.8, such a narrow energy-banded O^+ is seen after 15:10 UT. The pitch angles of these O^+ are nearly against the magnetic field, i.e., flowing outward from the Earth's northern hemisphere. Such a spectrogram with narrow band O^+ is typically seen in the polar cap.

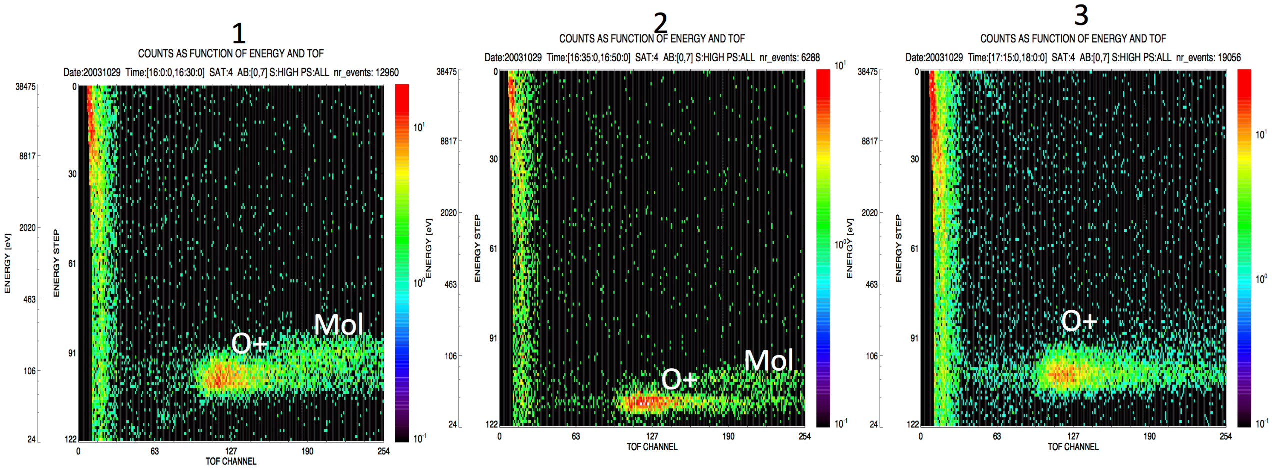

Figure 4.9 <cluster_O2_20031029>: Energy versus time-of-flight scatter plot of ion events measured by Cluster CIS/CODIF during the Halloween storm on 29 October 2003. (a) 16:00-16:30 UT, (b) 16:35-16:50 UT, and (c) 17:15-18:00 UT. These periods are indicated by horizontal arrows and hatches in Figure 4.8. Horizontal axis is time-of-flight (TOF), which is inversely proportional to the velocity in the instrument. The vertical axis is ion energy (channel 80: ~500 eV; channel 90: ~200 eV; and channel 105: ~90 eV).

For this time period (after 15:10 UT), the time-of-flight (TOF) spectra of the CODIF data can be used to determine if molecular ions coexist with O^+. Figure 4.9 shows a scatter plot of energy versus TOF for three time periods labeled in Figure 4.8. During the first two time periods (16:00-16:30 UT and 16:35-16:50 UT) both in the morning sector in the polar cap, the low-energy O^+ ions are evident, with a peak at a TOF channel around 100, and a long tail towards higher TOF. But the O^+ peak is accompanied by a second track at higher energy and longer time-of-flight consistent with molecular ions. Such separation in energy of the outflowing ions is typically seen in the polar cap between H^+ and O^+ (e.g., Nilsson et al., 2006), and hence is attributed to mass difference for Figure 4.9, too. During the last time period (17:15-18:00 UT, the midnight sector near the polar cap boundary), only the O^+ track is observed showing that the molecules from the dayside outflow are not reaching this location.

There are also low energy field-aligned ions observed during the inner magnetosphere perigee pass (L < 5). The pitch angles of O^+ at 30-300 eV, shown in the bottom panel of Figure 4.8, have peaks close to either at 0 or 180 degrees. The field-aligned dominance indicates that these heavy ions directly come from the ionosphere, including those trapped and bouncing after outflowing from even lower latitude (Quinn and McIlwain, 1979). In both cases, the source is at lower latitude than the ions seen in the polar cap (e.g., after

15:10 UT in Figure 4.8). To evaluate the existence of molecular ions, we again examine the time-of-flight. Figure 4.10 shows the result for the ions at 30-200 eV during 13:15 - 14:10 UT (perigee pass at L < 5) where the low-energy field-aligned O^+ is observed. Here we show a histogram instead of a scatter plot. The expected TOF location of the molecular ions is marked with the blue arrow. A clear enhancement is observed there, indicating that molecular ions were outflowing not just in the cusp region, but in the lower latitude closed-field line region at < 62-63° Inv, as well, for this intense storm.

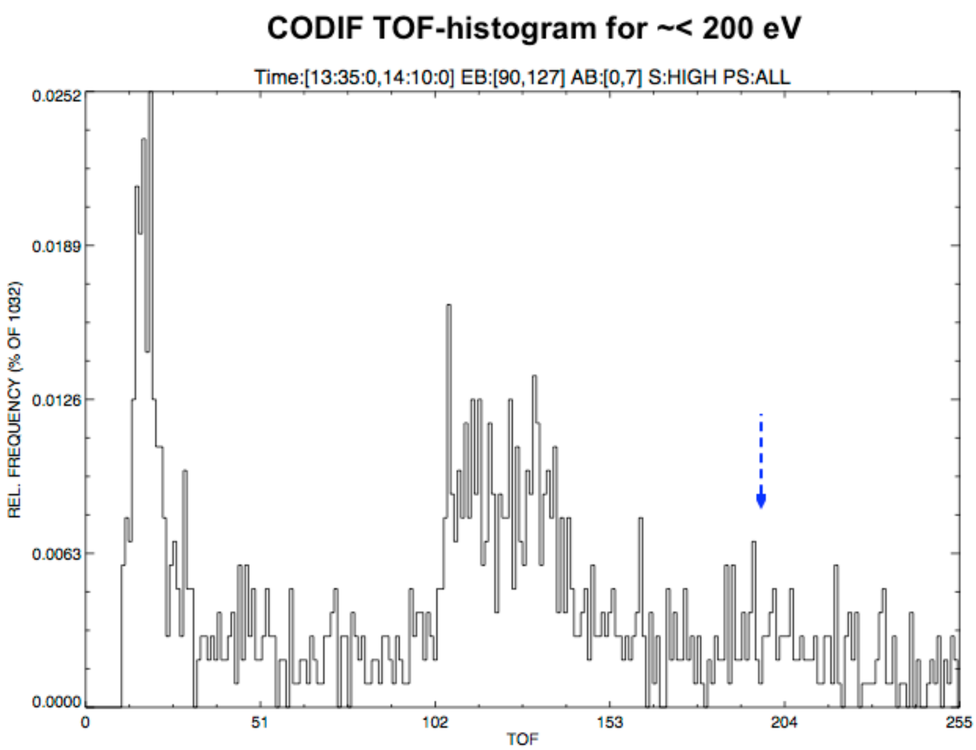

Figure 4.10 <fromPPT_Lynn1330_1410>: Time-of-flight Histogram of ion events in the energy range 30-200 eV during 13:15 - 14:10 UT, where outflowing ions are observed. The vertical dashed arrow corresponds to the expected location of molecular ions (m/q ~ 30).

4.2.3 Ground-based data

To investigate the ion upflow, incoherent scatter (IS) radars such as EISCAT VHF and UHF radars have long been used to infer the extraordinary upward convection up to about 500 km altitude (e.g., Wahlund et al., 1992; Ogawa et al., 2019, Takada et al., 2021). However, these IS radar observations cannot separate the ion composition, and need assumptions to estimate the heavy ion upflow (assume certain composition ratio of H^+, O^+, and N_2^+ for EISCAT case). Furthermore, for the actual ionospheric observations, the obtained maximum upward ion velocities are a few hundred m/s (~ 10^{-3} eV), which are negligible compared to the escape velocity (10^1 eV). Therefore, the upflow observation by these IS radars does not necessarily mean an upflow above the exobase, or, more importantly, must not be interpreted simply as the upflow of molecular ions at higher altitudes, as shown in Sect 4.2.1 (significant high-altitude/low-altitude difference observed by e-POP and Akebono). The heavy ion upflow at sub-auroral latitudes (where e-POP detected molecular ions with sufficient flux) needs sufficient additional energization (via wave-particle interactions, for example) to the magnetosphere, and this is not easy because of the lower electromagnetic activity than the auroral latitude.

Thus, using an IS radar to estimate the molecular ion motion is very misleading and is not recommended unless one makes a statistical study with the radar data and e-POP observation using many traversals. On the other hand, the EISCAT radars can monitor the general upflow condition, allowing us to define the necessary condition for molecular ions to reach the topside ionosphere, particularly for the dayside polar cap source.

4.3 Upper atmospheric source of metallic ions (Ground-based observation, Model)

4.3.1 Re-visit of Fe^+

As covered in Sect. 2.3, there are layers of neutral metal atoms in the atmosphere that appear globally between about 75 and 110 km as well as layers of ionized metal atoms between about 90 and 130 km (Plane 2003; Plane et al., 2015a). As discussed in Sect. 2.3.3, these metallic ions in the lower part of the ionosphere can reach the exobase ionosphere where heavy molecular ions are detected because of the similar mass as these molecular ions. The same mass-argument applies to the energization process above the ionosphere; i.e., metallic ions that have arrived at the exobase should reach the magnetosphere. However, with a mass only twice the O_2^+ mass, Fe^+ (mass 56) was detected with only 350 counts by Geotail over 20 years (about 2 count per month), which is far below the detection of the heavy molecular ions in the magnetosphere (Sect 2.2). This low detection rate can set the boundary condition for ionospheric transport models for vertical ion transport, which are still under development (e.g., Shinagawa and Oyama, 2006).

4.3.2. Lidar observation combining with magnetospheric patchy data

As summarized in Sect 2.3.2, metallic ions (Na, K, Fe, Ca, Ca^+, Li, Ni and AlO) in the lower ionosphere and thermosphere are mainly observed by many methods. If limited to low altitudes below the mesosphere, the modern resonance lidar is able to make diurnal observations (Plane, 2003). Even the vertical velocity can be measured (e.g., down to 1 cm/s resolution for Na atoms) between 80 and 105 km by Na lidar (Gardner et al., 2014). The vertical fluxes for other species can also be estimated by co-locating the other lidar (e.g., Fe lidar).

Although the altitude range for the lidar measurement covers only the lower part of the ionosphere, such monitoring helps qualitatively understanding the dynamics of metallic species during the ionospheric conditions that enhance the molecular ion upflow above the exobase because the required upward convection for such transport is common (“strong”) for both the metallic ions and heavy molecular ions, as mentioned in Sect. 2.3.3. In this sense, monitoring the dynamics of metal layers (AlO, Ni, Na, and Fe with existing technology) in the ionosphere when the molecular ion upflow is observed by low-altitude satellite could be useful because any lidar data can potentially be compared with low-altitude satellite observations that is capable of separating heavy ion (mass > 20 amu) such as e-POP. For example, statistics of conjugate observations for better understanding of the dynamics of the metal species in the condition that molecular ion upflow is enhanced.

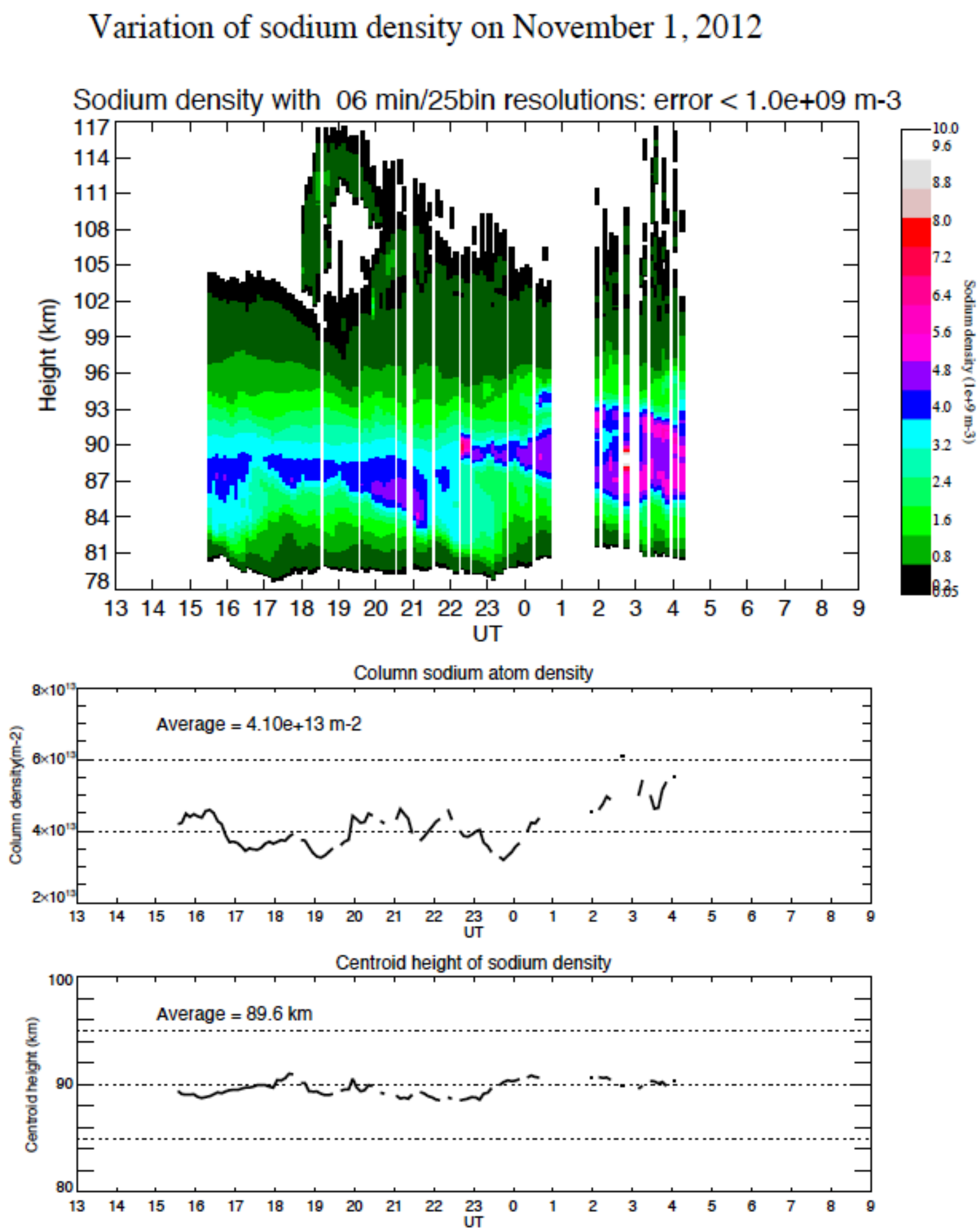

Figure 4.11 <nozawa_lidar_121101>: Sodium (Na) atom density (top), column sodium atom density (middle), and the centroid height (bottom) with 6 min/1 km resolutions obtained with the sodium LIDAR at Tromsø on 1 November 2012. This particular sodium lidar at Tromsø cannot make observations under sunlit conditions (this is why the observation started late).

Here we show an example for Na atom observation. The sodium atom layer usually exists between 80 and 110 km with a peak height between ~87-92 km. The lower edge of the sodium layer is sharp with a scale height of 2 – 3 km, reflecting the rapid conversion of Na into molecules such as $NaHCO_3$ (Plane, 2003). The top-side of the layer also has a small scale-height because of the conversion of Na into Na^+ in the lower ionosphere. Figure 4.11 shows sodium atom density data obtained at Tromsø (67° geomagnetic latitude; (69.6°N, 19.2°E) in geographic coordinate) (Nozawa, et al., 2014) over 11 hours, starting from 15:30 UT on 1 November 2012.

On this particular night (1 November 2012), the upper part of the sodium layer extended above 110 km from about 18 to 20 UT. The column sodium density (middle panel) varies with time, and does not show any particular increase during the time interval. The centroid height of the sodium density (bottom panel) varies with time in height range between 89 and 91 km, and again no special feature is found during 18 and 20 UT. It was rather geomagnetically active interval with 3 hourly local K index (3-hour resolutions) at Tromsø being 6 (15-18 UT) and 6 (18-21 UT). Thus, although the cause of the extension of the sodium density above 110 km is not clear at a moment, auroral activity could be involved.

Figure 4.12 shows one such example on 7 October 2015 during the major storm as summarized in Sect. 4.2.1. Tromsø Na lidar data (sodium density) started observation from 17 UT, about the one hour after e-POP detected heavy molecular ion upflow at around 20.4 MLT (corresponds to about 19 UT at Tromsø) as shown in Figure 4.6. The local K-index (3-hour resolutions) at Tromsø was 5, 7, 6, 4, 5 from 15 UT on 7 October 2015 and AL reached < -1500 nT at 18-19 UT. While the e-POP observation for the traversals at later hours are not optimum, both Dst and AE are developing during the following few hours after the e-POP detection of molecular ions at around 16:15 UT.

During that few hours, the lidar detected significant variation of sodium density and thickness of the layer. The upper edge of the sodium layer (the density of 5×10^7 m^{-3}) was located at 100 km at 17 UT, decreasing with time to reach about 95 km at 23 UT on the same night. The auroral activity was high, implying that the sodium density variation and the altitude variation can be partly due to the auroral effect and gravity waves, superimposed on the diurnal tidal variation. This upward expansion of the Na signal, which is not as clear as the Figure 4.11 (1 November 2012), can be due to daily variation but may also have some relation with enhanced access of the molecular ions to the topside ionosphere, which is suggested from the e-POP observation.

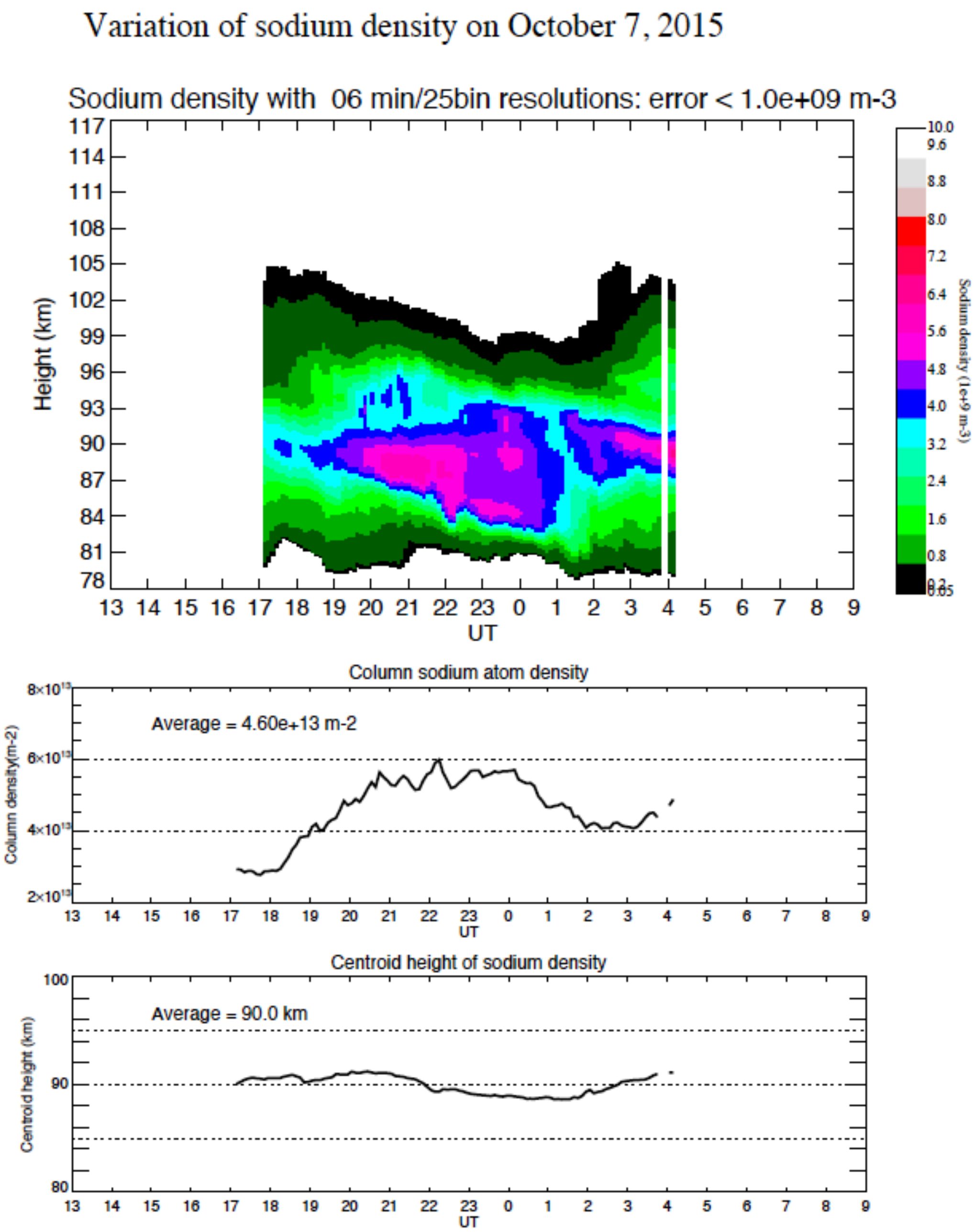

Figure 4.12 <nozawa_lidar_151007 >: Same as Figure 4.11a but for on 7 October 2015, right after the e-POP event in Figure 4.12b.

Finally, very long-time monitoring of the metal layer by lidar potentially have another merit from space safety monitoring viewpoint. For elements that the space debris has much more fraction than meteorite, we might be able to see the effect of ablation of space debris (space waste) as the new deposit.

4.3.3 Model of neutral wind for heavy elements

The possibility of metallic ions reaching the exobase and magnetosphere can be explored using models of the upper atmospheric transport of heavy elements to high altitudes potentially beyond the exobase. Recently, two global circulation models, SAMI3 (Huba et al., 2019) and WACCM-X (Wu et al., 2021), have been developed to study the transport of metallic ions in the thermosphere. WACCM-X is a chemistry-climate model that includes the injection of metals from meteoric ablation, and the full neutral and ion-molecule chemistry of Fe (m = 56), Mg (m = 24) and Na (m = 23). This model shows that metal ions are transported to altitudes above 400 km at low geomagnetic latitudes by **E x B** forcing - the so-called daily "fountain effect" (Wu et al., 2021).

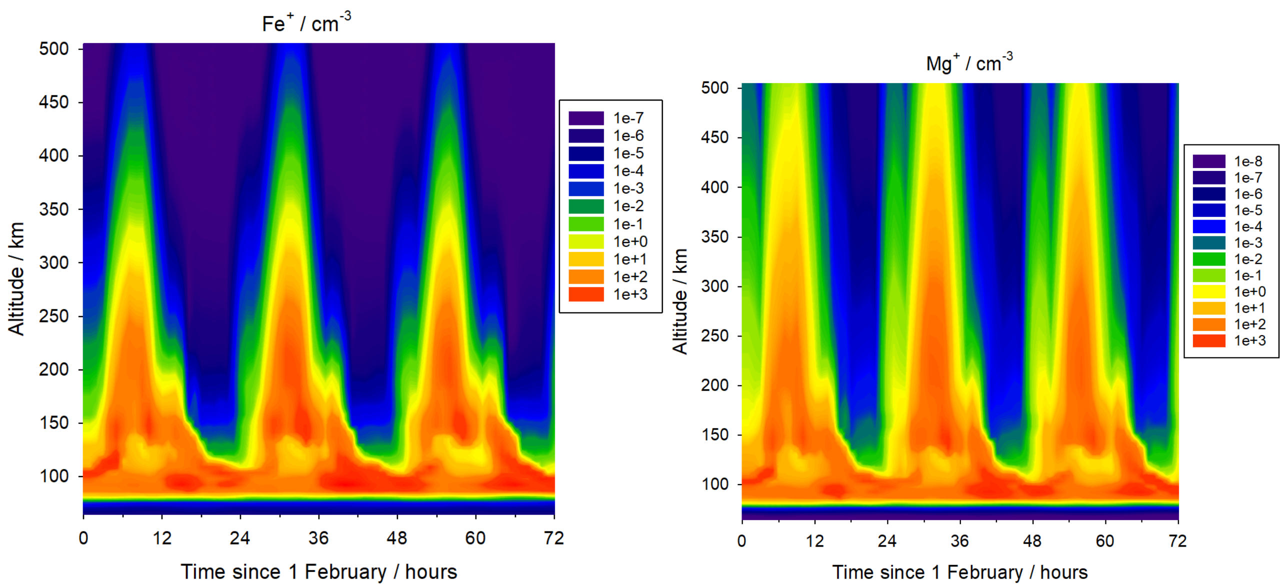

Figure 4.13 Modelled Fe^+ (left-hand panel) and Mg^+(right-hand panel) concentrations (units: ion cm^{-3}) calculated by WACCM-X for 3 days from February 1st, at 80º S and 90º E. The time axis refers to UT. Although the highest Fe^+ and Mg^+ concentrations are in the main layers below 120 km, there is significant uplift of the metal ions to ~500 km (the model top) starting around 03:00 UT (0900 LT).

Figure 4.13 shows an example of WACCM-X model output for the southern polar region during average geomagnetic conditions in February (i.e., slightly after the summer solstice

and perihelion, when ionizing solar radiation maximizes). The model predicts that both Fe^+ and Mg^+ daily reach 500 km altitude, which is the top of the model and most likely above the exobase, even during average geomagnetic condition. By reaching the exobase, these metallic ions may access the space in the same manner as molecular ions. Figure 4.10b shows that more Mg^+ than Fe^+ reaches this altitude, reflecting its lower mass. This behaviour is only seen in the model for southern polar latitudes during summer. The corresponding uplift in northern polar latitudes during summer is much smaller.
Considering the high-altitude location where molecular ions are known to reach high altitudes (Sect. 2.2), those metallic ions that reach the exobase might even access the high altitude, particularly for disturbed periods when we expect stronger upward convection and hence these metallic ions may reach the magnetosphere.

4.4 Re-entering space debris as a heavy ion source: Outlook and unanswered questions

Table 2.5: Orbiting artificial objects

	2019-01	2022-12	2023-12
orbiting satellite*1	~ 5000	~ 9780	~ 11500
debris on catalogue	~ 22300	~ 32400	~ 35110
total mass of orbiting objects	> 8400 t	> 10500 t	> 11500 t
∑ fragmentation events	> 500	> 630	> 640
number of debris（>10cm）	~ 36500 (model estimate 2021)		
number of debris（1-10cm）	~ 1 million (model estimate 2021)		
number of debris（0.1-1cm）	~ 130 million (model estimate 2021)		

ESA (2023b), space debris by numbers, December, 2023, www.esa.int/Our_Activities/Operations/Space_Debris/Space_debris_by_the_numbers
*1. Both functional and nonfunctional ones

Today's society is heavily reliant on the space infrastructure (satellites), and one can safely assume that this dependence will only increase in the near future (ESA, 2023a). The surge of large satellite constellations (LSC) consisting of several 1000 satellites due to the commercialization of space will increase the number and mass of spacecraft launched into Earth' orbit exponentially. The start of this exponential rise stemming from the installation of LSCs can already be seen today, as depicted in Figure 4.14. Over less than five years, total mass of orbiting objects increased by 20%, their number by more than 50% as shown in Table 2.5.

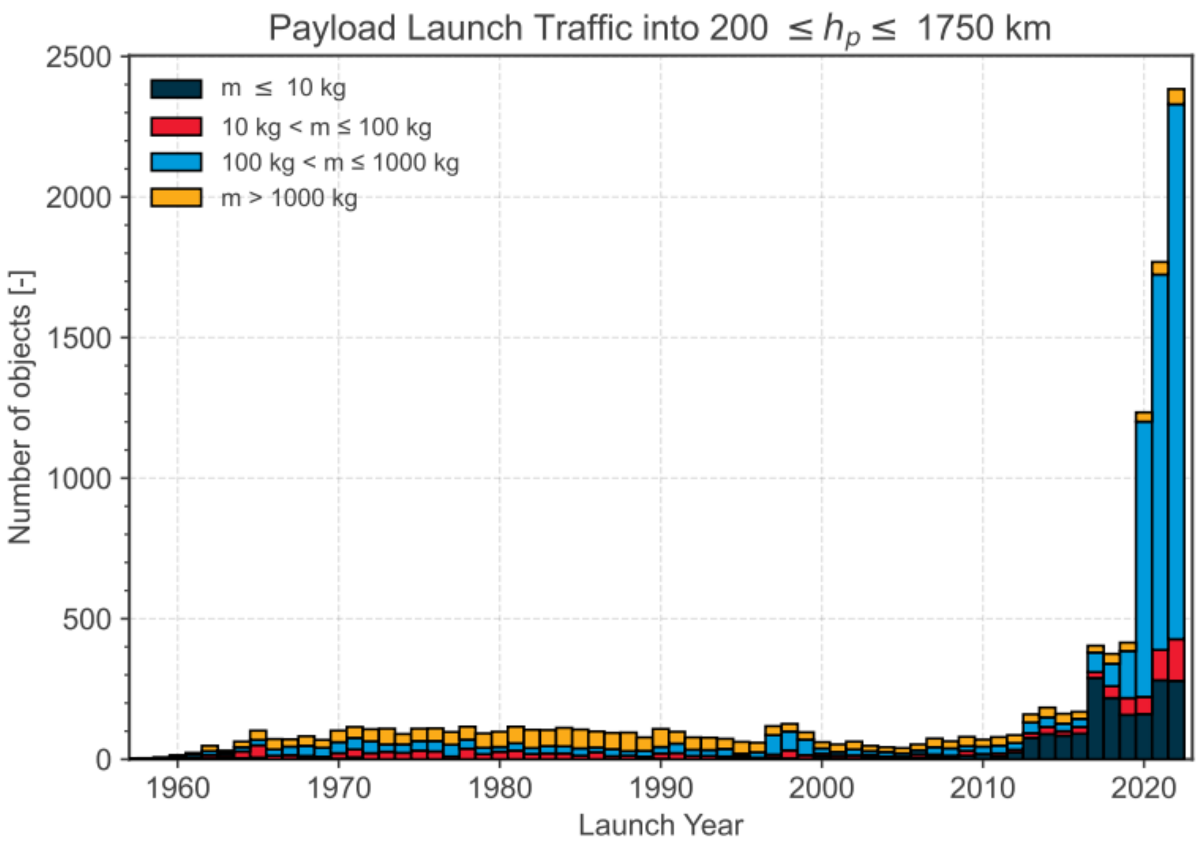

Figure 4.14: ESA (2023a), Annual space environment report, September 2023 (www.sdo.esoc.esa.int/environment_report/Space_Environment_Report_latest.pdf)

Decommissioning of spacecraft and remnants of launches lead to the re-entry of space debris/waste into the atmosphere, where it ablates and injects atoms and ions as described in Sect. 2.3.2. However, very few existing studies modelling spacecraft re-entry focus on the atmospheric mass injection as this topic has been mostly disregarded in the past.

Comprehensive atmosphere mass input calculations and observations of particles transported downwards to stratosphere heights show that the injection of metal atoms and ions into the atmosphere is already higher due to the ablation of space debris/waste than the meteoroid input for some element species, currently Al, Cu, Ge, Li and Pb (Schulz et al., 2021, Murphy 2023). Other rare metallic elements have also been observed (such as

Nb, Ag, and Hf) and even traces of a large number of additional metals. In the future, the projected and already occurring strong increase in on-orbit spacecraft mass will lead to other element species injecting more mass compared to the natural input, namely Ti and Ni and a large number of the trace metals. Thus, the possibility of environmental effects and the contamination of the mesospheric heavy ion source should not be underestimated as even the rocket-boosters used to launch payloads into space contribute to the artificial influx as they partially ablate during re-entry (Schulz et al., 2021). It has even been suggested that the increase of re-entering material due to mega-constellations can begin an uncontrolled experiment of geoengineering by altering the Earth's albedo (Boley and Byers, 2021).

Additionally, fragmentation events like explosions, impacts and loss of mass (solid rocket motor dust, paint flakes and other ejecta), or deliberate destructions lead to a continued growth of the number of space objects parallel to the increasing overall mass (Lawrence et al., 2022). Fragmentation is a constant source of sub 100 μm particles in LEO, which are extremely numerous (see Table 2.5). It is currently unclear how far down the size range of these sources extend. It is also unclear whether these particles undergo further processing and transport to contribute as a heavy ion source before particles are lost from the system due to atmospheric drag or solar radiation. Space missions measuring dust in this size range in LEO, like dust instruments on board Destiny+ asteroid mission (Krueger et al. 2019), are vital in studying these questions.

Finally, the increase in rocket launches might have an effect on ion transport from mesospheric heights due to gravity and acoustic waves generated by rocket exhaust (e.g Noble 1990; Mabie et al. 2016), although its effectiveness is unclear.

5. Summary and Future observation

5.1 Summary of unanswered science questions

For high charge-state heavy ions that obviously originate from the solar wind (including solar energetic particles), there are some statistics for each large-scale region as shown in Figure 1.1, but even the basic entry route, the entry mechanism (similarity and difference from the alpha particle), and energization level from the original source are still unanswered. This is mainly due to the severe limitation of the existing instruments for such measurements. So far Geotail/STICS provided the best dataset for high charge-state heavy ions in the magnetosphere and its surroundings, but the instrument capability is limited to high energy (> 100 keV) and to very low time resolution for heavy ions. Therefore, we could not even separate between the direct effect of the solar wind and magnetospheric activity that influence the configuration of the magnetospheric boundary.

The same problem applies to the low charge-state metallic and heavy molecular ions, which have several candidates as the source. We here stress that their extremely low flux (no single source is hiding the other source like H^+ or O^+) in turn gives unique information of the source and the supply route as the tracer. In addition, even the sources are not determined: the Moon and/or the Earth's upper atmosphere, and for the upper atmosphere a fraction of the ions coming from the nightside sub-auroral region compared to the dayside polar region. The only route so far established is dayside high-latitude (through the plasma lobe) for heavy molecular ion that is the same route as one of the routes for O^+ circulation and hence is expected to take the similar route and energization until they reach the inner magnetosphere (Yamauchi, 2019, and references therein). The other routes are difficult to identify, and it is even more difficult to evaluate the effect of the external conditions (e.g., solar wind, magnetospheric activity, Moon phase) under which ions from these sources appear.

Nevertheless, by re-examining the existing data from instruments that were not designated for separating molecular ions (e.g., Cluster/CODIF), and combining with new data (e.g., from e-POP), we could identify new direct supply routes of the molecular ions (auroral region) to the inner magnetosphere, which is independent from the known high-latitude route.

Re-examination of existing data (e.g., Geotail/STIC and ACE) and combining other datasets (e.g., Kaguya and Chang'e) is also important in evaluating the Moon source as discussed in Sect. 4.1: We cannot rule out the possibility of a substantial contribution from the Moon during CIR/CME time periods. Thus, we still do not know the relative importance among the Moon, mesosphere, or the solar wind as the source of the low-charge state metallic ions. In this respect, further examination of Kaguya (mission terminated in 2009) is important as well as continued analyses of on-going e-POP and Arase, all of which are capable of detecting molecular ions and/or metallic ions.

For the other possible clues to investigate the upflow of the metallic ions, new models like WACCM-X and SAMI show that metallic ions might be transported regularly to altitudes above 500 km (above the exobase) in the particular locations (high-latitude). There models should ideally be combined with ionosphere-magnetosphere models and with possible observations in future (see Sect. 5.3 below). Such model-model and model-observation comparisons will further determine the probability that these heavy metallic ions can be lifted into the magnetosphere. Finally, contamination by space debris/waste emerges as a new open question, requiring new works in the future.

5.2 Desired specification for observation and model

Since our observational knowledge on the heavy molecular and metallic ions ($m > 20$) in the magnetospheric is very poor, we first need to define what measurements are highest priority for these ions. The lack of dedicated missions in the past is partly because it has been difficult to design ion instruments that can separate heavy species with sufficient geometric factor. To design the optimum set of feasible instrumentation, we need to know the limitation of the ion instruments on board past and current spacecraft. The limitations are:

1. In energy coverage: e.g., the IRM ion mass spectrometer onboard e-POP was limited to ions up to 90 eV/e (Yau and Howarth, 2016), and the STICS ion mass spectrometer onboard Geotail had an energy threshold of ~10 keV (Williams et al., 1994).
2. Ambiguity of ion trajectory with finite entrance cross-section and small deviation of electric and magnetic field inside the instrument reduce the mass resolution: e.g., the

CODIF ion mass spectrometer onboard Cluster had a mass resolution of m/Δm ≈ 5–7 (Rème et al., 2001), and HPCA onboard MMS had m/Δm ≈ 4 (Young et al. 2016).

3. Size of the instrument and upper limit of the field strength inside the instruments limit the mass range.
4. Fragmentation of the molecular ions when going through the thin carbon foil limits the molecular ion measurements for foil-type TOF instruments (e.g., Heredia-Avalos and Garcia-Molina, 2000).
5. Small geometric factor, which requires long integration time to accumulate adequate counting statistics for minor species (e.g., Haaland et al., 2020). Currently, obtaining angular (pitch angle) information within a short sampling time and at high mass resolution is not easy.
6. The instrument sensitivity degrades the over the years due to the detector gain fatigue mechanism (e.g., Kistler et al., 2013).
7. Gaussian (as opposed to exponential) line shape of instrument mass response results in non-negligible contributions to the measured minor ion counts from nearby major ion species (cf. Figure 4.7).

As a result, even the separation of the molecular ion measurements (separating m/q ≈ 30 from m/q = 16 without charge state information) has been difficult for medium energy (50 eV – 50 keV), for which Arase was the first magnetospheric mission that can separate the molecular ion group at the medium-energy. The instrument onboard Wind aimed the resolution in design, but the achieved resolution was not sufficient due to technical issues. Therefore, unlike traditional ion mass analyzers for the four major magnetospheric species (the H^+, He^{++}, He^+, and O^+ group), we cannot require sufficient resolution for all directions (temporal, energy, angular) when measuring the metallic and heavy molecular ions.

With these limitations in mind, we have to define the direction of instrumentation and measurement improvements to advance our knowledge.

1. Have a mass range up to > 60 amu, to include Fe ions and heavy ionospheric molecular ions (see Figure 1.1).
2. Cover most important energy ranges that are different in different magnetospheric regions: from cold ions (eventually few eV by ram flow) up to < 100 eV corresponding to the upwelling ions at low altitudes below the main energization region (Yau et al., 2021), from a few eV up to a few keV corresponding to the outflowing heavy ions at high

altitudes above the main energization region or the cusp (Kistler et al., 2010a), up to few 10’s of keV corresponding to energetic heavy ions streaming down tail (Christon et al., 1994; Seki et al., 1998), and to a higher energy range for ions in the ring current, where the returning ions experience adiabatic acceleration (Ejiri, 1978). The wide energy range is also needed in the magnetospheric boundary region where pickup cold heavy ions and foreshock heavy ions can gain energy (Grünwaldt et al., 1997, Stasiewicz et al., 2013).

3. Obtain modest angular resolution with respect to the magnetic field while providing a mass resolution $m/\Delta m \geq 15$ over a wide energy range. This allows separating minor molecular ions (m = 25 - 35) from CNO-group atomic ions (m < 20), and minor heavier metallic ions (m > 40) from molecular ions. Such a mass resolution can be achieved through an isochronous TOF ion mass spectrometer, such as e.g. the MSA instrument onboard BepiColombo MMO (Delcourt et al., 2016) and JDC instrument onboard JUICE (Wittmann, 2022), or through a grazing incidence MCP time-of-flight ion mass spectrometer (Devoto et al., 2008). Alternatively, for ions up to keV, a magnetic ion mass spectrometer such as the IMA instrument onboard Mars Express (Barabash et al., 2006) would achieve this requirement by tuning the mass range and size (Nicolaou et al., 2017). The advantage of this design is that the ions do not touch the instrument elements other than the final detector (no fragmentation nor loss of energy).
4. Employ a high geometric factor design, or a new filtering/starting TOF mechanism (against the fragmentation of the molecular ions at the starting foil/surface of TOF) to allow for the separation of molecular ions within 30 minutes for keV range and 10 minutes for cold ions.
5. Employ a high mass resolution design of $m/\Delta m \geq 60$, to separate Al^+ (m = 27) from Si^+ (m=28) or N_2^+ (m = 28) at least above the ionosphere and in the ring current. The CELIAS/MTOF instrument on the SOHO spacecraft provided such a mass resolution for solar wind ions, i.e., for 0.5 - 30 keV/nuc ions (Hovestadt et al. 1995). There are designs and prototyping for such instruments that allow even for $m/\Delta m > 100$ (Wurz et al., 1998). Rosetta was equipped with a design for cold (<10 eV) ions (Balsiger et al. 2007). The technology is also available for hot (0.05-10 keV) ions on Kaguya/IMA instrument (Saito et al., 2010), i.e., $m/\Delta m>15$, and improved to $m/\Delta m > 40$ for Mio (launched 2018), and $m/\Delta m > 100$ for MMX (to be launched in 2026).
6. Time resolution must be sufficient to separate different possible supply routes (e.g., the direct supply from the ionosphere and detoured supply through the tail) and to complete

the traversal over each region. Here, the mass resolution and time resolution are related, and higher energy ranges generally require longer integration time due to the much lower ion flux in the Earth's magnetosphere. If we require as low as $m/\Delta m > 15$, instruments that fulfil this requirement (tens of minutes to hours to move from one region to another for high-altitude mission) are available almost all energy ranges.

The monitoring of the heavy ions is needed both in the magnetospheric region and in the possible source region. While the solar wind is being monitored at L1 for space weather monitoring purposes, new monitoring spacecraft or base is need for the Moon and the ionosphere/mesosphere. Here, the ionosphere includes both lower altitudes and above the exobase. To correlate any "event" in the source region and magnetospheric observation, time resolution must be comparable or less than such an "event", which means a time resolution < 10 minutes (e.g., substorms) for ionospheric origin low energy ions and hours for Moon origin ions or magnetospheric high-energy ions.

On the other hand, the duration of heavy ion events in the magnetosphere can be as long as a few days, i.e., the time scale of magnetic storms. Also, CME and CIR last several hours to a day. The question is then whether the heavy ions are supplied intermittently or continuously, or simply at one time with a slow and long decay. To distinguish between them, we need continuous monitoring (i.e., to return to the same region) for many days in raw. These time-scale requirements limit the types of acceptable spacecraft orbits.

5.3 Desired missions and observations

For in-situ observations, the best is to have dedicated mission, even as a secondary objective of any mission. Alternatively, placing a set of instruments on non-science missions such as Earth Observation satellites and Space Safety missions (including geostationary one) or the transfer spacecraft to/from the coming Lunar Gateway. The current plan for the Lunar Gateway is to be equipped with HERMES (Heliophysics Environmental and Radiation Measurement Experiment Suite) instrument package, comprising also the SPAN-Ai Ion Mass Spectrometer (2 eV - 40 keV ions, although $m/\Delta m$ about 10 at moment).

In all cases, the key instruments are (1) an ion mass spectrometer of $m/\Delta m > 60$ for wide mass range of $m/q>60$, and (2) lower mass resolution (yet $m/\Delta m > 15$) but sufficient angular resolution of at least 22.5° (6° is ideal because, for example, this is needed to detect the position where the ions are generated around the Moon), while keeping mass range up to $m/q > 60$. (3) In addition, adding total ion flux without mass resolution but with very good $\Delta E/E$ is good complement for absolute accuracy in velocity and particularly the density. The energy range of the instruments are divided into (a) cold, (b) hot up to few tens keV, and energetic. For the hot ions, it would be wise to divide into two different energy ranges to have better energy and mass resolution. In this case, it is also wise to use different detection methods for such divided energies each. In addition to the ion instruments, technology of the (4) optical limb observation from satellites has also advanced, e.g. sounding of Mg^+. If limb observation becomes possible for the other metallic species, this would be a strong satellite tool in future.

Any of these key instruments are useful to be placed on the other missions mentioned above (as a package). As for the dedicated mission, it would be good to have a multi-spacecraft mission with the spacecraft having different orbits, such as low altitude (400 - 4000 km), mid-altitude (2000 - 30000 km), and high-altitude (4 - 10 Re), as well as the ionospheric source (200 - 500 km). Monitoring of the possible source population is also important. For the solar wind source, L1 monitoring spacecraft has been and will provide key information, whereas for the Moon source, the coming Lunar Gateway would be a good platform to place the key instrument like Kaguya/IMA.

If allowed only one spacecraft, then that mission should aim for all escaping ions, and have a highly elliptic because most of the Earth observation satellites are in nearly circular orbit, such as the ESCAPE (European SpaceCraft for the study of Atmospheric Particle Escape) mission, which was proposed to ESA in response to the M5 call (Dandouras et al., 2018). The proposed ESCAPE mission spacecraft was designed as a slowly spinning spacecraft on a high inclination 500 km × 33 000 km orbit, i.e., with a perigee at the terrestrial exobase, and was equipped with instrumentation responding to the above criteria. With many ion mass instruments with an optical monitor of the exospheric heavy atoms, it was designed to separate even nitrogen and oxygen. With modern technology, several dips into much lower altitude to cover the middles thermosphere and ionosphere could be considered, similar to what MAVEN satellite did for Mars with the Neutral Gas and Ion Mass Spectrometer (NGIMS) instrument onboard.

The monitoring of the source region is also essential. Since the Moon monitor is mentioned in previous subsection, we here describe the Earth part (ground-based observations) including the ultimate source of meteorites. Here, the important outputs are how much of the source ions may reach the exobase and topside ionosphere. This requires, in addition to monitoring the geomagnetic activity that is already available, (1) instruments and models that provide upward transport of heavy ions in the mesosphere, ionosphere, and thermosphere with high spatial resolution, and (2) monitoring of possible source population (although it is only "possible" source with current understanding) of the amount of metallic ions and atoms in the lower part of the ionosphere. Candidate for (1) is modern incoherent scatter radar such as EISCAT_3D, and candidate for (2) is lidars.

For lidars, we need to keep the observation site, and even expand to more sites (ideally two latitudes at ~80° and ~60° in both hemispheres corresponding to two major outflow latitudes that e-POP revealed, and three longitudinal locations to separate temporal and diurnal variations) as well as target species. We particularly need to monitor Ca^+ layer (ionized form) and Fe layer (originated from mainly meteoroids but space debris/waste might become detectable first in amount), while searching for AlO (the Al species observable by lidar) could be useful for evaluating the contribution from the space debris/waste, although its current AlO density predicted by an atmospheric model is very low (Plane et al., 2021)

Since it is unclear how much transient enhancements of the metal layer influence the total upward transport (such as by meteor showers and large re-entry events of space debris/waste) it is desirable to gain a more complete picture of the current input of mass to the atmosphere. This also includes the observation of the ablation process, by which the material is distributed in the atmosphere. These observations should be performed using many different detection methods (e.g. dust detectors, lidars, radars, optical systems) and missions.

The observation of the ablation process is particularly important for evaluating the ablation of space debris/waste because the modelling and indirect observations suggest that minor species such as Al, Cu, Ge, Li and Pb coming from space debris/waste might already constitute a significant contamination to the naturally occurring particles from meteoroids. There are currently no data on very small-scale debris statistics and evolution. For evaluating this effect, a multi-probe experimental flight through a possible ion cloud (after re-entry of the fist probe that imitates the space debris/waste) would be useful. Such an experiment would gather information on the ablated amount and altitude distribution, as well as the effectiveness of vertical transport of the generated ion cloud. For such an experiment, remote observation from the LEO satellite should also be added by aligning the re-entry orbit to the ideal LEO satellite for monitoring. As a similar attempt, Deadalus proposal (Sarris et al., 2020) is can make such attempt although the target is ionosphere but not mesosphere.

5.4 Modelling of upward transport of metallic and molecular ions in the ionosphere and mesosphere

It would be ideal if one can assimilate the relatively rare observations (e.g., in Sect. 4) into thermospheric and ionospheric transport models. The molecular ion upflow at sub-auroral latitude and sudden expansion of the metal layer (see the example in Sect. 4.3.2 for Na) are examples that need to be reproduced by transport models.

For modelling (particularly for evaluating the ablation of space debris/waste), the source flux for the solar wind and the upper atmospheric molecular ion distribution as the ground state are well understood. Also, in the case of the mesospheric metal layers, the current understanding is quite mature, and we have a long history of measurements and models. As such, for the purpose of transport to the magnetosphere, the mass input to these metal layers by meteoroids is no longer required in modelling except for the increasing input from the ablation of the space debris/waste.

On the other hand, understanding the transport of heavy metals from the mesosphere to higher altitudes needs further understood because of lack of monitoring satellites for these heavy ions for past 40 years as summarized in Table 3.1. The last capable satellite was DE-2 in early 1980's and flight much higher altitude than exobase. Alongside such additional observations, model development is also needed to evaluate the transport of metallic ions to beyond the exobase. Currently WACCM-X reaches 500 km altitude but not further. One possible development could be to couple such atmospheric and ionospheric models with magnetospheric models of wave-particle interaction. This would extend the modelling regime into the magnetosphere and would yield predictions that could be compared with measurements.

Al though the meteoric mass input to the atmosphere is roughly known and it is possible to estimate the contribution from the re-entry of human-made objects (e.g., satellites and space debris), the details concerning the ablation needs more modelling and observations, and total influx estimates and its composition need refining. These details are needed in order to estimate in what way and how much these influxes contribute to the mesospheric metal layer. This is particularly important for space debris/waste to prognose the future evolution of the metal layer by the increasing launch of rockets to the space. Almost no observational work has been done on examining the deposition altitude distribution and composition from deorbiting debris. Thus, comprehensive modelling of the ablation process of space debris/waste is needed. Due to the complex nature of the ablation and the subsequent chemical and physical processing of the injected material, modelling should be complemented and validated by more detailed and numerous observations of spacecraft re-entries, especially of spacecraft resembling typical orbital and mass characteristics of the already numerous low-Earth orbit communication satellites (LCS). Although there are estimates on the total influx of debris based on the mass of objects contained in regions that will deorbit, the deposition altitudes are key to understanding the impact on our atmosphere. In some areas it might be time-critical to intensify the research before the anthropogenic influence due to the increase in re-entry of space debris/waste reaches a level that causes significant perturbations to natural environment in the atmosphere and the space.

6. Conclusion

Very minor ions in the magnetosphere have unique information because of their low flux (no single source is hiding the other source like the case for H^+ or O^+), on both the source and the transport route. However, their transport is not well understood because of the lack of observations, which partly results from the instrument capabilities for the terrestrial missions in the past and present. While we need new observations with suitable instrumentation, the technology and design of which are already available and are used in current planetary missions, re-examining the exiting datasets, and combining different datasets can also give new insights on this subject. We have shown several examples for such re-examinations of data, e.g., the importance of considering the Moon and space debris/waste as the detectable sources for the metallic ions in the magnetosphere. Therefore, a related database of measurements taken by old instruments listed in section 3 with designs more than 20-years old are still useful, along with more recent models. This in turn means that we need new observations and missions in the near future with available technology, as summarized in section 5.

Acknowledgments

The work was supported by International Space Science Institute (ISSI) in Bern, through ISSI International Team project #518. JMCP was supported by the European Office of Aerospace Research and Development (award no. FA8655-21-1-7031). We thank Victoria Foss for providing Figure 4.6, which is from her thesis research and is to be submitted for publication, and thank Wuhu Feng (National Centre for Atmospheric Science, UK) for providing the WACCM-X data shown in Figure 4.13. The French participation in the Cluster project (part of the work by ID) has been supported in part by CNES. IM's work is within a project funded by Research Council of Norway, NFR 275503.

Dst and AE (used in Sect. 4.2.1 and Sect. 4.3.1) are provided by the World Data Center for Geomagnetism, Kyoto (https://wdc.kugi.kyoto-u.ac.jp/wdc/Sec3.html). Tromsø geomagnetic field (used in Sect. 4.3.1) is provided by Tromsø Geophysical Observatory (https://flux.phys.uit.no/stackplot/). Kp (used in Sect. 4.1.1 and 4.2.1) is provided by GFZ German Research Centre for Geosciences (https://isdc.gfz-potsdam.de/kp-index/). SOHO proton monitor data (used in Sect. 4.1.2) is provided by the SOHO/CELIAS/MTOF Proton Monitor team (https://space.umd.edu/pm/). Geotail STICS, LEP, and orbit data (used in Sect. 4.1.2) are provided by GEOTAIL/EPIC Science Data Center (http://sd-www.jhuapl.edu/Geotail/Years_dir.html), Geotail database (https://www.stp.isas.jaxa.jp/geotail/) and ERG Science Center (https://ergsc.isee.nagoya-u.ac.jp/cef/orbit.cgi), respectively. ACE level 3 data (used in Sect. 4.1.2) is provided by the ACE team (https://izw1.caltech.edu/ACE/ASC/DATA/level3/summaries.html). All Cluster data are available at the Cluster Science Archive (https://csa.esac.esa.int/csa-web/).

Funding: see acknowledgement

Ethics approval and consent to participate: Not applicable

Consent for publication: all agreed

Data availability: see acknowledgement and tables in section 3

Materials availability: see acknowledgement

Code availability: summarized in tables in section 3

Author contribution: All contributed discussion and Sections 1 and 3. MY overviewed all sections. For Section 2 and 4, the main contributors are: Solar wind observations (CS, LMK, PW), the Moon observations and models (YS, PW, MY), magnetospheric observations (CS, ID, SH, LMK, YS, MY), ionospheric outflow observation and model (ID, SW, MY, AWY), ionosphere (AWY), meteoroid/debri ablation (DK, JMCP, LS, IM), metal layers (SN, JMCP), Section 5 (ID, DK, LMK, JMCP, LS, YS, PW, MY, AWY).

Rereferences

Aellig MR, Hefti S, Grünwaldt H, et al (1999) The Fe/O elemental abundance ratio in the solar wind as observed with SOHO CELIAS CTOF. J. Geophys. Res., 104:24769-24780. https://doi.org/10.1029/1999JA900309

Aikin AC, Goldberg RA (1973) Metallic ions in the equatorial ionosphere. J. Geophys. Res. 78:734. https://doi.org/10.1029/JA078i004p00734

Anders E and Grevesse N (1989) Abundances of elements: Meteoritic and solar. Geochim. Cosmochim. Acta 53: 197-214.

Arai T, Okada T, Yamamoto Y, et al (2008) Sulfur abundance of asteroid 25143 Itokawa observed by X-ray fluorescence spectrometer onboard Hayabusa. Earth, Planets, and Space 60:21-31. https://doi.org/10.1186/BF03352758

Asamura K, Kazama Y, Yokota S, et al (2018): Low-energy particle experiments-ion mass analyzer (LEPi) onboard the ERG (Arase) satellite, Earth Planets Space, 70, 70, https://doi.org/10.1186/s40623-018-0846-0

Asplund M, Grevesse N, Sauval AJ, Scott P (2009) The chemical composition of the sun, Ann. Rev. Astron. Astrophys, 47:481-522, doi:10.1146/annurev.astro.46.060407.145222

Balsiger H, Altwegg K, Bochsler P, Eberhardt P, et al (2007), ROSINA - Rosetta Orbiter Spectrometer for Ion and Neutral Analysis, Space Science Review 128, 745-801.

Bame SJ, Asbridge JR, Hundhausen AJ, and Strong IB (1968a), Solar wind and magnetosheath observations during the January 13-14, 1967, geomagnetic storm, J. Geophys. Res., 73(17), 5761-5767, doi:10.1029/JA073i017p05761.

Bame SJ, Hundhausen AJ, Asbridge JR, and Strong IB (1968b) Solar wind ion composition, Phys. Rev. Lett., 20, 393-395, doi:10.1103/PhysRevLett.20.393

Bame SJ, Asbridge JR, Hundhausen AJ, and Montgomery MD (1970), Solar wind ions: $^{56}Fe^{+8}$ to $^{56}Fe^{+12}$, $^{28}Si^{+7}$, $^{28}Si^{+8}$, $^{28}Si^{+9}$, and $^{16}O^{+6}$, J. Geophys. Res., 75(31), 6360-6365, doi:10.1029/JA075i031p06360.

Bame SJ, Asbridge JR, Feldman WC, et al (1975) Solar wind heavy ion abundances. 43:463-473. https://doi.org/10.1007/BF00152368

Barabash S, Lundin R, Andersson H, et al (2006), The Analyzer of Space Plasmas and Energetic Atoms (ASPERA-3) for the Mars Express Mission. Space Sci Rev 126, 113-164, doi: 10.1007/s11214-006-9124-8

Barabash S, Fedorov A, Lundin R, et al (2007), Measurements from Mars Express show that the solar wind is removing only a small amount of Mars' atmosphere, implying that the formally abundant H2O and CO2 remain underground, Science, 315(5811), 501-503, doi:10.1126/science.1134358.

Battie F, Fossati T, and Gallucci S (2013) Vega 4th stage direct re-entry survivability analysis and causality risk assessment, in Proceeding of 6th European Conference on Space Debris, 723, 57

Benna M, Mahaffy PR, Grebowsky JM, et al (2015), Metallic Ions in the upper atmosphere of Mars from the passage of Comet C/2013 A1 (Siding Spring), Geophys. Res. Lett., 42, 4670-4675, doi:10.1002/2015GL064159

Berchem J, Russell CT (1982) The thickness of the magnetopause current layer: ISEE 1 and 2 observations. J Geophys Res 87:2108-2114. https://doi.org/10.1029/JA087iA04p02108

Berner RA (1999), Atmospheric oxygen over Phanerozoic time, Proc. Natl. Acad. Sci. USA, 96, 1095510957.

Berner RA (2006) Geocarbsulf: A combined model for Phanerozoic atmospheric O2 and CO2, Geochim. Cosmochim. Acta, 70, 5653-5664. doi:10.1016/j.gca.2005.11.032

Bochsler P (1989) Velocity and abundance of silicon ions in the solar wind. 94:2365-2373. https://doi.org/10.1029/JA094iA03p02365

Bochsler P (2007) Minor ions in the solar wind. 14:1-40. https://doi.org/10.1007/s00159-006-0002-x

Bochsler P, Geiss J, Kunz S (1986) Abundances of carbon, oxygen, and neon in the solar wind during the period from August 1978 to June 1982. 103:177-201. https://doi.org/10.1007/BF00154867

Bochsler P, Ipavich FM, Paquette JA, et al (2000) Determination of the abundance of aluminum in the solar wind with SOHO/CELIAS/MTOF. 105:12659-12666. https://doi.org/10.1029/1999JA005085

Bochsler P, Lee MA, Karrer R, et al (2010) Kinetic temperatures of iron ions in the solar wind observed with STEREO/PLASTIC. In: Maksimovic M, Issautier K, Meyer-Vernet N, et al (eds) Twelfth international solar wind conference. pp 257-260

Boley AC, Byers M (2021) Satellite mega-constellations create risks in Low Earth Orbit, the atmosphere and on Earth. Sci Rep 11:10642. https://doi.org/10.1038/s41598-021-89909-7

Bones, DL, Carrillo-Sánchez JD, Kulak AN, Plane JMC (2019), Ablation of Ni from micrometeoroids in the upper atmosphere: experimental and computer simulations and implications for Fe ablation, Planet. Space Sci., 179, 104725, doi:10.1016/j.pss.2019.104725

Bones, DL, Carrillo-Sánchez JD, Connell SDA, Kulak AN, Mann GW, Plane JMC (2022), Ablation Rates of Organic Compounds in Cosmic Dust and Resulting Changes in Mechanical Properties During Atmospheric Entry, Earth Space Sci., 9, e2021EA001884, doi:10.1029/2021EA001884

Borovička J, Koten P, Shrbený L, et al (2014) Spectral, photometric, and dynamic analysis of eight Draconid meteors. Earth Moon Planets 113:15-31. https://doi.org/10.1007/s11038-014-9442-x

Borovička J, Spurný P, Koten P (2007) Atmospheric deceleration and light curves of Draconid meteors and implications for the structure of cometary dust. A&A 473:661-672. https://doi.org/10.1051/0004-6361:20078131

Breneman HH and Stone EC (1985). “Solar coronal and photospheric abundances from solar energetic particle measurements.” Astrophys. Jou. 299: L57-L61.

Brosch N, Häggström I, Pellinen-Wannberg A (2013) EISCAT observations of meteors from the sporadic complex. \mnras 434:2907-2921. https://doi.org/10.1093/mnras/stt1199

Brownlee DE, Tsou P, Anderson JD, et al (2003) Stardust: Comet and interstellar dust sample return mission. J. Geophys. Res. 108:8111. https://doi.org/10.1029/2003JE002087

Buttsworth D, Morgan R, and Jenniskens P (2013), Near-ultraviolet emission spectroscopy of the Hayabusa reentry, J. Spacecraft Rockets, 50, 1109-1120, doi:10.2514/1.A32500

Campbell-Brown MD, Borovička J, Brown PG, Stokan E (2013) High-resolution modelling of meteoroid ablation. A&A 557:A41. https://doi.org/10.1051/0004-6361/201322005

Campbell-Brown, M.D. (2019), Meteoroid structure and fragmentation, Planet. Space Sci., 169, 1-7, https://doi.org/10.1016/j.pss.2019.03.005

Canfield DE (2005), The early history of atmospheric oxygen: homage to Robert M. Garrels, Annu. Rev. Earth Planet. Sci., 33, 1-36, doi:10.1146/annurev.earth.33.092203.122711

Carpenter, J, C. Speak, A. Chouker, M. Talevi, R. Nakamura, A. Santangelo, I. Crawford, D. Cullen, B. Bussey, and J. Grenouilleau (2018), Research Opportunities on the Deep Space Gateway: Findings from the Workshop and Call for Ideas (2018). ESA-HSO-K-RP-0284

Carrillo-Sánchez, J. D.; Gómez-Martín, J. C.; Bones, D. L.; Nesvorný, D.; Pokorný, P. Benna, M.; Flynn, G. F.; Plane, J. M. C. (2020) Cosmic dust fluxes in the atmospheres of Earth, Mars, and Venus, Icarus, 335, art. no. 113395, doi:10.1016/j.icarus.2019.113395

Carter LN, Forbes JM (1999) Global transport and localized layering of metallic ions in the upper atmosphere. Ann Geophys 17:190-209. https://doi.org/10.1007/s00585-999-0190-6

Ceplecha Z, Borovička J, Elford WG, et al (1998) Meteor Phenomena and Bodies. Space Science Reviews 84:327-471. https://doi.org/10.1023/A:1005069928850

Chappell CR, Fields SA, Baugher CR, et al (1981), The retarding ion mass spectrometer on dynamics Explorer-A, NASA technical report NASA-TM-82418. https://ntrs.nasa.gov/citations/19810016373

Chappell CR, Olsen RC, Green JL, et al (1982), The discovery of nitrogen ions in the earth's magnetosphere, Geophys. Res. Lett., 9, 937-940.

Christon SP, Gloeckler G, Williams DJ, et al (1994), Energetic atomic and molecular ions of ionospheric origin observed in distant magnetotail flow-reversal events, Geophys. Res. Lett., 21, 3023-3026

Christon SP, Hamilton DC, Plane JMC, et al (2017), Discovery of suprathermal ionospheric origin fe^{+} in and near earth’s magnetosphere, J. Geophys. Res., 122, https://doi.org/10.1002/2017JA024414

Christon SP, Hamilton DC, Mitchell DG, et al (2019) Suprathermal magnetospheric atomic and molecular heavy ions at and near earth, jupiter, and saturn: Observations and identification. J. Geophys. Res., 124, https://doi.org/10.1029/2019JA027271

Christon SP, Hamilton DC, Mitchell DG, Plane JMC, and Nylund SR (2020), Suprathermal magnetospheric atomic and molecular heavy ions at and near Earth, Jupiter, and Saturn: Observations and identification, J. Geophys. Res., 125, e2019JA027271, doi:10.1029/2019JA027271

Chu X, Yu Z, Gardner CS, Chen C, and Fong W (2011), Lidar observations of neutral Fe layers and fast gravity waves in the thermosphere (110-155 km) at McMurdo (77.8S, 166.7E) Antarctica, Geophys. Res. Lett., 38, L23807, doi:10.1029/2011GL050016

Cladis JB (1986), Parallel acceleration and transport of ions from polar ionosphere to plasma sheet, Geophys. Res. Lett., 13, 893-896, doi:10.1029/GL013i009p00893

Colaprete A, Sarantos M, Wooden DH, et al (2016) How surface composition and meteoroid impacts mediate sodium and potassium in the lunar exosphere. Science 351:249-252. https://doi.org/10.1126/science.aad2380

Collier MR, Hamilton DC, Gloeckler G, et al (1996) Neon-20, oxygen-16, and helium-4 densities, temperatures, and suprathermal tails in the solar wind determined with WIND/MASS. 23:1191-1194. https://doi.org/10.1029/96GL00621

Craven PD, Olsen RC, Chappell CR, Kakani L (1985) Observations of molecular ions in the earth's magnetosphere, J. Geophys. Res., 90, 7599-7605, doi:10.1029/JA090iA08p07599.

Crismani MMJ, Schneider NM, Plane JMC, et al (2017), Detection of a persistent meteoric metal layer in the Martian atmosphere, Nat. Geosci. 10, 401-404, doi:10.1038/ngeo2958

Dandouras I, Yamauchi M, and the ESCAPE proposal team (2016), European SpaceCraft for the study of Atmospheric Particle Escape (ESCAPE), Mission proposals to 2016 ESA's call for M5 Mission, http://cluster.irap.omp.eu/public/ESCAPE/ESCAPE$_$M5$_$Proposal$_$V1.1.pdf

Dandouras I, Yamauchi M, J. De Keyser J, et al (2018), ESCAPE: A mission proposal for ESA-M5 to systematically study Exosphere and atmospheric escape using European, Japanese, and US instruments (Japanese with English Abstract/Tables/Figures), in Proceedings of the 18th Space Science Symposium, SA6000118033, S10-001, 9-10 Jan, 2018, JAXA/ISAS. https://repository.exst.jaxa.jp/dspace/handle/a-is/876320

Dandouras I, Blanc M, Fossati L et al (2020), Future Missions Related to the Determination of the Elemental and Isotopic Composition of Earth, Moon and the Terrestrial Planets. Space Sci Rev, 216, doi:10.1007/s11214-020-00736-0

Dandouras I (2021), Ion outflow and escape in the terrestrial magnetosphere: Cluster advances. J. Geophys. Res.: Space Physics, 126, doi: 10.1029/2021JA029753

Delcourt DC, Sauvaud JA, and Moore TE (1993), Polar wind ion dynamics in the magnetotail. J. Geophys. Res., 98, 9155-9169, doi:10.1029/93JA00301

Delcourt D, et al (2016), The Mass Spectrum Analyzer (MSA) on board the BepiColombo MMO, J. Geophys. Res. Space Physics, 121, 6749- 6762, doi:10.1002/2016JA022380

Del Pozo, C. F, Hargreaves, J. K, and Aylward, A. D. (1997), Ion composition and effective ion recombination rate in the nighttime auroral lower ionosphere. J. Atmosph. Solar Terr. Phys. 59, 15, 1919-1943

Devoto, P, Médale, J.-L, and Sauvaud, J.-A. (2008), Secondary electron emission from distributed ion scattering off surfaces for space instrumentation, Rev. Sci. Instru., doi: 10.1063/1.2912821

Dobarco-Otero J, Smith RN, Bledsoe KJ, et al (2005) The Object Reentry Survival Analysis Tool (ORSAT)... In 56th international astronautical congress of the international astronautical federation, the international academy of astronautics, and the international institute of space law, B6-3. doi:10.2514/6.IAC-05-B6.3.06

Dukes CA and Baragiola RA (2015) The lunar surface-exosphere connection: Measurement of secondary-ions from Apollo soils, Icarus, 255, 51-57, doi:10.1016/j.icarus.2014.11.032

Eastman T, Christon S (1995) Ion composition and transport near the earth's magnetopause. Washington DC American Geophysical Union Geophysical Monograph Series 90:131. https://doi.org/10.1029/GM090p0131

Eberhardt P, Geiss J, Graf H, et al (1972) Trapped solar wind noble gases in Apollo 12 lunar fines 12001 and Apollo 11 breccia 10046. Lunar and Planetary Science Conference Proceedings 3:1821-1856

Ejiri M (1978) Trajectory traces of charged particles in the magnetosphere, J. Geophys. Res., 83, 4798-4810, doi:10.1029/JA083iA10p04798

Elphic RC, Funsten III HO, Barraclough BL, et al (1991). Lunar surface composition and solar wind-induced secondary ion mass spectrometry, Geophys. Res. Lett., 18(11), 2165-2168, https://doi.org/10.1029/91GL02669.

Elphic R.C., et al (2015) LADEE science results and implications for exploration, in 2015 Annual Meeting of the Lunar Exploration Analysis Group, No. ARC-E-DAA-TN27029, 2015, https://ntrs.nasa.gov/citations/20160000571

ESA (2019), SpaceEnvironment Report 2019, https://www.esa.int/Safety_Security/Space_Debris.

ESA (2023a), Annual space environment report, https://www.sdo.esoc.esa.int/environment_report/Space_Environment_Report_latest.pdf

ESA (2023b), Space debris by the numbers, https://www.esa.int/Our_Activities/Operations/Space_Debris/Space_debris_by_the_numbers

Feldman U, Landi E, Schwadron NA (2005) On the sources of fast and slow solar wind. J. Geophys. Res. (Space Physics) 110:A07109. https://doi.org/10.1029/2004JA010918

Feng W, Marsh DR, Chipperfield MP, et al (2013), A global atmospheric model of meteoric iron, J. Geophys. Res. Atmos., 118:9456-9474, doi:10.1002/jgrd.50708

Föhn, M, Galli, A, Vorburger, A, Tulej, M, Lasi, D, Riedo, A, et al (2021), Description of the ion-optical system of a mass spectrometer for JUpiter's ICy moons Explorer, IEEE Aerospace Conference, Big Sky, MT, USA, 50100, 1-14, https://doi.org/10.1109/AERO50100.2021.9438344

Fomenkova MN, Evlanov EN, Muknin LM, et al (1989) Chemical composition and properties of comet Halley dust particles as obtained during VEGA Mission. Meteoritics 24:267

Foss, V. (2019) Molecular Ions in Ion Upflows and their Effect on Hot Atomic Oxygen Production. MSc thesis, University of Calgary, Canada

Flegel SK, Gelhaus J, Möckel M, et al (2009) Multi-layer insulation model for MASTER-2009, Acta Astronautica, 69, 911-922, doi:10.1016/j.actaastro.2011.06.015

Friedman, J. S, X. Chu, C. G. M. Brum, and X. Lu, Observation of a thermospheric descending layer of neutral K over Arecibo, J. Atmos. Sol.-Terr. Phys.104 (2013) 253-259.

Fritsche B, Klinkrad H, Kashkovsky A, and Grinberg E (2000), Spacecraft disintegration during uncontrolled atmospheric Re-entry, Acta Astronautica, 47, 513-522, doi:10.1016/S0094-5765(00)00090-4

Füri E. and Marty B (2015), Nitrogen isotope variations in the Solar System, Nature Geosci., 8, 515-522, doi:10.1038/ngeo2451

Futaana Y, Barabash S, Holmström M, and Bhardwaj A (2006) Low energy neutral atoms imaging of the Moon, Plan. Space Sci., 54, 2, 132-143, doi:10.1016/j.pss.2005.10.010

Galvin AB, Ipavich FM, Gloeckler G, et al (1996), Solar wind composition: First results from SOHO and future expectations. In: American astronomical society meeting abstracts #188. p 49.05

Galvin AB, Kistler LM, Popecki MA et al (2008), The Plasma and Suprathermal Ion Composition (PLASTIC) Investigation on the STEREO Observatories, Space Sci Rev 136, 437-486. doi:10.1007/s11214-007-9296-x

Gao B, Mathews JD (2015) High-altitude radar meteors observed at Jicamarca Radio Observatory using a multibaseline interferometric technique. Monthly Notices of the Royal Astronomical Society 452:4252-4262. https://doi.org/10.1093/mnras/stv1548

Gardner, C. S, Liu, A. Z, Marsh, D. R, Feng, W, and Plane, J. M. C. (2014), Inferring the global cosmic dust influx to the Earth's atmosphere from lidar observations of the vertical flux of mesospheric Na, J. Geophys. Res., 119, 7870-7879, doi:10.1002/2014JA020383.

Geiss J, Eberhardt P, Bühler F, et al (1970), Apollo 11 and 12 solar wind composition experiments: Fluxes of He and Ne isotopes. J., Geophys. Res. 75, 5972. https://doi.org/10.1029/JA075i031p05972

Geiss J, Balsiger H, Eberhardt P. et al (1978) Dynamics of magnetospheric ion Composition as observed by the GEOS mass spectrometer. Space Sci Rev 22, 537-566, doi:10.1007/BF00223940

Geiss J, Gloeckler G, Balsiger H, et al (1992), Plasma composition in Jupiter's magnetosphere: Initial results from the solar wind ion composition spectrometer. Science 257, 1535-1539. https://doi.org/10.1126/science.257.5076.1535

Geiss J, Gloeckler G, von Steiger R (1995), Origin of the solar wind from composition data. Space Sci Rev 72,49-60. https://doi.org/10.1007/BF00768753

Geiss, J, Bühler, F, Cerutti, H, Eberhardt, P, Filleux, Ch, Meister, J, and Signer, P. (2004), The Apollo SWC Experiment: Results, Conclusions, Consequences. Space Sci. Rev., 110:307-335, doi: 10.1023/B:SPAC.0000023409.54469.40.

Gerding M, Daly S, Plane JMC (2019) Lidar soundings of the mesospheric nickel layer using Ni(^{3}F) and Ni(^{3}D) transitions, Geophys. Res. Lett., 46, 408-415, doi:10.1029/2018GL080701

Giammanco C, Wurz P, Karrer R (2008) Minor ion abundances in the slow solar wind. 681:1703-1707. https://doi.org/10.1086/588578

Gilbert JA, Lepri ST, Landi E, Zurbuchen TH (2012) FIRST MEASUREMENTS OF THE COMPLETE HEAVY-ION CHARGE STATE DISTRIBUTIONS OF C, O, AND Fe ASSOCIATED WITH INTERPLANETARY CORONAL MASS EJECTIONS. The Astrophysical Journal 751:20. https://doi.org/10.1088/0004-637x/751/1/20

Gloeckler G and Hamilton DC (1987), AMPTE ion composition results, Phys. Scr., 1987, 73-84. doi:10.1088/0031-8949/1987/T18/009

Gloeckler G, Wilken B, Stuedemann W, Ipavich FM, Hovestadt D et al (1985), First composition measurement of the bulk of the storm-time ring current (1 to 300 keV/e) with AMPTE-CCE. Geophys. Res. Lett., 12, 325-328, https://doi.org/10.1029/gl012i005p00325

Gloeckler G, Geiss J, Balsiger H, et al (1992) The solar wind ion composition spectrometer. Astronomy and Astrophysics Supplement Series 92:267-289

Gomez, R. G, Fuselier, S. A, Mukherjee, J, Gonzalez, C. A, Burch, J. L, Strangeway, R. J, & Starkey, M. J. (2019), The extra-magnetospheric ion environment as observed by the Magnetospheric Multiscale mission hot plasma composition analyzer (MMS-HPCA), J. Geophys. Res., 124, 1509-1524. doi:10.1029/2018JA025392

Gomez Martín JCG, Bones DL, Carrillo-Sánchez JD, James AD, Trigo-Rodríguez JM, Fegley B Jr. and Plane JMC (2017), Novel experimental simulations of the atmospheric injection of meteoric metals, Astrophys. J., 836, 212, doi:0.3847/1538-4357/aa5c8f

Gorney DJ, Church SR, and Mizera PF (1982) On ion harmonic structure in auroral zone waves: The effect of ion conic damping of auroral hiss, J. Geophys. Res., 87, 10479-10486, doi:10.1029/JA087iA12p10479

Grande M, Perry CH, Blake JB, et al (1996). Observations of iron, silicon, and other heavy ions in the geostationary altitude region during late March 1991, J. Geophys. Res, 101, 24707-24718, doi:10.1029/96ja00044

Grebowsky JM and Bilitza D (2000), Sounding Rocket Data Base of E- and D-Region Ion Composition. Adv. Space Res. 25, doi:10.1016/S0273-1177(99)00916-3

Grebowsky JM, and Aikin AC (2002): In situ measurements of meteoric ions, in: Meteors in the earth's atmosphere, edited by: Murad, E., and Williams, I. P., Cambridge University Press, Cambridge, 189-214.

Grebowsky JM, Benna M, Plane JMC, et al (2017) Unique, non-Earthlike, meteoritic ion behavior in upper atmosphere of Mars. Geophys. Res. Lett. 44, doi:10.1002/2017GL072635

Grevesse N (1984) Accurate atomic data and solar photospheric spectroscopy. Physica Scripta Volume T 8:49-58. https://doi.org/10.1088/0031-8949/1984/T8/008

Grevesse N and Sauval AJ (1998). Standard solar composition, Space Sci. Rev. 85: 161-174.

Grevesse N, Scott P, Asplund M. and Jacques Sauval A (2015), The elemental composition of the Sun III. The heavy elements Cu to Th?, Astron. Astrophys, 573, A27, https://doi.org/10.1051/0004-6361/201424111

Gritsevich MI (2009) Determination of parameters of meteor bodies based on flight observational data. Advances in Space Research 44:323-334. https://doi.org/10.1016/j.asr.2009.03.030

Gronoff G, Arras P, Baraka S, et al (2020). Atmospheric escape processes and planetary atmospheric evolution. J. Geophys. Res., 125. doi: 10.1029/2019JA027639

Gruchoła S, Galli A, Vorburger, A, and Wurz P. (2021): "Future Venus missions and flybys: A collection of possible measurements with mass spectrometers and plasma instruments,"Adv. Sp. Res., 68(8), 3205-3217, DOI: 10.1016/j.asr.2021.07.024

Grünwaldt, H, et al (1997), Venus tail ray observation near Earth, Geophys. Res. Lett., 24, 1163-1166, doi.org:10.1029/97GL01159

Gulkis S, Alexander C (2008) Composition measurements of a comet from the rosetta orbiter spacecraft. Space Sci Rev 138:259-274. https://doi.org/10.1007/s11214-008-9335-2

Haaland S, Daly PW, Vilenius E, et al (2020), Suprathermal Fe in the Earth's plasma environment: Cluster RAPID observations, J. Geophys. Res., 125, e27596, https://doi.org/10.1029/2019JA027596

Haaland S, Daly PW, Vilenius E (2021) Heavy metal and rock in space: Cluster RAPID observations of Fe and Si. J. Geophys. Res. 126, e2020JA028852. https://doi.org/10.1029/2020JA028852

Halekas JS, Poppe AR, Delory GT, et al (2012), Lunar pickup ions observed by ARTEMIS: Spatial and temporal distribution and constraints on species and source locations, J. Geophys. Res., 117, E06006, doi:10.1029/2012JE004107

Halekas JS, Benna M, Mahaffy PR, et al (2015), Detections of lunar exospheric ions by the LADEE neutral mass spectrometer, Geophys. Res. Lett., 42, 5162-5169, doi:10.1002/2015GL064746

Hamilton DC, Gloeckler G, Ipavich FM, et al. (1988), Ring current development during the great geomagnetic storm of February 1986, J. Geophys. Res., 93, 14343-14355. doi:10.1029/JA093iA12p14343

Harrison J, Kaiser A, and Vanden JM (2010), Atmospheric oxygen level and the evolution of insect body size, Proc. R. Soc. B, 277, 19371946, doi:10.1098/rspb.2010.0001

Heber VS, McKeegan KD, Steele RCJ, et al (2021) Elemental abundances of major elements in the solar wind as measured in genesis targets and implications on solar wind fractionation. 907:15. https://doi.org/10.3847/1538-4357/abc94a

Heidrich-Meisner V, Peleikis T, Martin K, et al (2016) Observations of high and low Fe charge states in individual solar wind streams with coronal-hole origin. Astronomy and Astrophysics 593:A70. https://doi.org/10.1051/0004-6361/201527998

Heikkila WJ, Winningham JD (1971) Penetration of magnetosheath plasma to low altitudes through the dayside magnetospheric cusps. 76:883. https://doi.org/10.1029/JA076i004p00883

Heredia-Avalos S, and Garcia-Molina R (2000), Energy loss of swift oxygen molecular ions traversing amorphous carbon foils, Physics Letters, A275, 73-79

Heritier KL, Altwegg K, Balsiger H, et al (2017) Ion composition at comet 67P near perihelion: Rosetta observations and model-based interpretation. Monthly Notices of the Royal Astronomical Society 469:S427-S442. https://doi.org/10.1093/mnras/stx1912

Hervig ME, Brooke JSA, Feng W, et al (2017) Constraints on meteoric smoke composition and meteoric influx using SOFIE observations with models, J. Geophys. Res. 122, 13495-13505, doi:10.1002/2017JD027657

Hervig ME, Plane JMC, Siskind DE, Feng WH, Bardeen CG, and Bailey SM (2021), New Global Meteoric Smoke Observations From SOFIE: Insight Regarding Chemical Composition, Meteoric Influx, and Hemispheric Asymmetry, J. Geophys. Res.-Atmospheres, 126, art. no.: e2021JD035007, doi:10.1029/2021jd035007

Hilchenbach M, Hovstadt D, Klecker B, and Möbius E (1993), Observation of energetic lunar pick-up ions near earth, Adv. Space Res., 13, 321-324, https://doi.org/10.1016/0273-1177(93)90086-Q

Hilchenbach, M. (2004), Remote Sensing of the Lunar or Asteroid Surfaces via Pick-Up Ions in the Solar Wind Downward Direction, ESA SP-543, 55-58.

Hill S (1976), Influence of atmospheric oxygen concentration on acetylene reduction and efficiency of nitrogen fixation in intact Klebsiella pneumoniae, Microbiol., 93, 335-345, doi: 10.1099/00221287-93-2-335

Hoffman JH, Dodson WH, Lippincott CR, Hammack HD (1974), Initial ion composition results from the Isis 2 satellite, J. Geophys. Res., 79, 4246--4251, doi:10.1029/JA079i028p04246.

Höffner J, and Friedman JS (2004), The mesospheric metal layer topside: a possible connection to meteoroids, Atmos. Chem. Phys., 4, 801-808, www.atmos-chem-phys.org/acp/4/801

Hollingsworth A, Engelen RJ, Textor C, et al (2008) Toward a monitoring and forecasting system for atmospheric composition: The GEMS project. Bulletin of the American Meteorological Society 89:1147. https://doi.org/10.1175/2008BAMS2355.1

Hovestadt D, Hilchenbach M, Bürgi A, et al (1995), CELIAS - charge, element and isotope analysis system for SOHO. Solar Phys., 162, 41-481. https://doi.org/10.1007/BF00733436

Huba, J. D, Krall, J, & Drob, D. (2019). Global ionospheric metal ion transport with SAMI3. Geophysical Research Letters, 46, 7937-7944, https://doi.org/10.1029/2019GL083583

Hulfeld L, Küchlin S, Jenny P (2021) Three dimensional atmospheric entry simulation of a high altitude cometary dustball meteoroid. A&A 650:A101. https://doi.org/10.1051/0004-6361/202140305

Hultqvist B (2002) Downward ion acceleration at auroral latitudes: cause of parallel electric field, Ann. Geophys., 20, 1117-1136, doi:10.5194/angeo-20-1117-2002

Hultqvist B, Øieroset M (eds) (1997) Transport across the boundaries of the magnetosphere. Kluwer Academic Publishers

Hundhausen AJ, Asbridge JR, Bame SJ, Gilbert HE, and Strong IB (1967) Vela 3 satellite observations of solar wind ions: A preliminary report, J. Geophys. Res., 72, 87-100, https://doi.org/10.1029/JZ072i001p00087.

Hunten DM 493 (1967) Spectroscopic studies of the twilight airglow. Space Sci. Rev. 6, 493-573, doi:10.1016/j.jastp.2005.06.010

Inness A, Ades M, Agustí-Panareda A, et al (2019) The CAMS reanalysis of atmospheric composition. Atmospheric Chemistry & Physics 19:3515-3556. https://doi.org/10.5194/acp-19-3515-2019

Ipavich FM, Galvin AB, Lasley SE, et al (1998) Solar wind measurements with SOHO: The CELIAS/MTOF proton monitor. 103:17205-17214. https://doi.org/10.1029/97JA02770

Istomin VG (1963) Absolute concentrations of ion components of the Earth's atmosphere at altitudes between 100 and 200 km. Planetary and Space Science 11:169-172. https://doi.org/10.1016/0032-0633(63)90139-9

Izmodenov VV (2007) Filtration of interstellar atoms through the heliospheric interface. 130:377-387, doi:10.1007/s11214-007-9203-5

James AD, Brooke JSA, Mangan TP, Whale TF, Plane JMC, and Murray BJ (2018), Nucleation of nitric acid hydrates in polar stratospheric clouds by meteoric material, Atmos. Chem. Phys., 18, 4519-4531, doi:10.5194/acp-18-4519-2018

Janches, D, Swarnalingam N, Carrillo-Sánchez JD, Gómez Martin JC, Marshall R, Nesvorny D, Plane JMC, Feng W, Pokorny P (2017), Radar Detectability Studies of Slow and Small Zodiacal Dust Cloud Particles. III, The Role of Sodium and the Head Echo Size on the Probability of Detection, Astrophys. J., 843, 1, doi:10.3847/1538-4357/aa775c

Jarosewich E (1990) Chemical analyses of meteorites: A compilation of stony and iron meteorite analyses. Meteoritics 25:323. https://doi.org/10.1111/j.1945-5100.1990.tb00717.x

Jenniskens P, Albers J, Koop MW, Odeh MS, et al (2016), Airborne observations of an asteroid entry for high fidelity modeling, AIAA 2016-0999, 54th AIAA Aerospace Sciences Meeting, doi:10.2514/6.2016-0999

Johnson B and Goldblatt C (2015), The nitrogen budget of Earth, Earth Sci. Rev., 148, 150-173, doi:10.1016/j.earscirev.2015.05.006

Jones AV (1974) Optical Emissions from Aurora. in "Aurora", Geophysics and Astrophysics Monographs, vol 9. Reidel Publishing Company, Dordrecht. doi:10.1007/978-94-010-2099-2_4

Jurewicz AJG, Burnett DS, Woolum DS, et al (2007) SIMS results for solar-wind elemental abundances from genesis collectors. Meteoritics and Planetary Science Supplement 42:5299

Kallenbach R, Ipavich FM, Bochsler P, et al (1998) Isotopic composition of solar wind calcium: First in situ measurement by CELIAS/MTOF on board SOHO. 498:L75-L78. https://doi.org/10.1086/311296

Kallio E, S. Dyadechkin, P. Wurz, and M. Khodachenko, "Space weathering on the Moon: Farside-nearside solar wind precipitation asymmetry," Planet. Sp. Sci. 166 (2019) 9-22, DOI: 10.1016/j.pss.2018.07.013.

Kameda S, Ikezawa S, Sato M, et al (2017): Ecliptic north-south symmetry of hydrogen geocorona, Geophys. Res. Lett., 44, 11706--11712. https://doi.org/10.1002/2017GL075915

Kane TJ, Gardner CS (1993) Lidar observations of the meteoric deposition of mesospheric metals. Science 259:1297-1300. https://doi.org/10.1126/science.259.5099.1297

Karrer R, Bochsler P, Giammanco C, et al (2007) Nickel isotopic composition and Nickel/Iron ratio in the solar wind: Results from SOHO/CELIAS/MTOF. 130:317-321. https://doi.org/10.1007/s11214-007-9220-4

Kastinen D, Kero J (2022) High-altitude meteors detected by the interferometric MU radar. Monthly Notices of the Royal Astronomical Society. https://doi.org/10.1093/mnras/stac2791

Kastinen D, Vierinen J, Grydeland T, Kero J (2023) Using radar beam-parks to characterize the Kosmos-1408 fragmentation event. Acta Astronautica 202:341-359. https://doi.org/10.1016/j.actaastro.2022.10.021

Keller JW, Chornay DJ, Hunsaker FH, and Ogilvie KW (1999), Gated time-of-flight plasma composition analyzer for space physics research, Rev. Sci. Instr., doi: 10.1063/1.1149881

Kero J, Szasz C, Pellinen-Wannberg A, Wannberg G, Westman A, and Meisel DD (2008), Three-dimensional radar observation of a submillimeter meteoroid fragmentation, Geophys. Res. Lett., 35, L04101, doi:10.1029/2007GL032733

Kero J, Fujiwara Y, Abo M, et al (2012) MU radar head echo observations of the 2011 October Draconids: MU observations of the 2011 October Draconids. Monthly Notices of the Royal Astronomical Society 424:1799-1806. https://doi.org/10.1111/j.1365-2966.2012.21255.x

Kero J, Campbell-Brown MD, Stuber G, et al (2019), Radar observation of meteors, in "Meteoroids: Sources of Meteors on Earth and Beyond", (eds) Ryabova G. O., Asher D. J., and Campbell-Brown M. D., Cambridge University Press, p. 65-89, doi:10.1017/9781108606462.008

Kessler DJ, and Cour-Palais BG (1978), Collision frequency of artificial satellites: The creation of a debris belt, J. Geophys. Res., 83(A6), 2637-2646, doi:10.1029/JA083iA06p02637.

Kissel J, Brownlee DE, Buchler K, et al (1986) Composition of comet Halley dust particles from Giotto observations. Nature 321:336-337. https://doi.org/10.1038/321336a0

Kistler KM, et al (2005), Contribution of nonadiabatic ions to the cross-tail current in an O^+ dominated thin current sheet, J. Geophys. Res., 110, A06213, doi:10.1029/2004JA010653

Kistler LM, Mouikis CG, Klecker B, and Dandouras I (2010a), Cusp as a source for oxygen in the plasma sheet during geomagnetic storms. J. Geophys. Res., 115, doi: 10.1029/2009JA014838

Kistler LM, Galvin AB, Popecki MA, Simunac KDC, et al (2010b), Escape of O+ through the distant tail plasma sheet, Geophys. Res. Lett., 37, L21101, doi:10.1029/2010GL045075

Kistler LM, Mouikis CG, Genestreti KJ (2013) In-flight calibration of the Cluster/CODIF sensor, Geosci. Instrum. Method. Data Syst., 2, 225-235, doi:10.5194/gi-2-225-2013

Klecker B, Möbius E, Hovestadt D, et al (1986), Discovery of energetic molecular ions (NO^+ and O_2^+) in the storm time ring current, Geophys. Res. Lett. 13, 632-635, https://doi.org/10.1029/GL013i007p00632

Klinkrad H (2005),Re-entry prediction and on-ground risk assessment, in Proceeding of 6th US/Russian Space Surveillance Workshop

Kopp E (1997) On the abundance of metal ions in the lower ionosphere. J. Geophys. Res. 102:9667-9674. https://doi.org/10.1029/97JA00384

Koppenwallner G, Fritsche B, Lips T, and Klinkrad H (2005) SCARAB - a multi-disciplinary code for destruction analysis of space-craft during re-entry. In Proceedings of the Fifth European Symposium on Aerothermodynamics for Space Vehicles, ESA-SP. 563, 8-11

Korth A, Richter AK, Loidl A, et al (1987) The heavy ion analyser PICCA for the Comet Halley fly-by with Giotto. Journal of Physics E Scientific Instruments 20:787-792. https://doi.org/10.1088/0022-3735/20/6/037

Koten, P, et al (2006), The beginning heights and light curves of high-altitude meteors, Meteor. Planet. Sci., 41, 1271-1419, https://onlinelibrary.wiley.com/doi/pdf/10.1111/j.1945-5100.2006.tb00523.x

Krauss S, Fichtinger B, Lammer H, et al (2012): Solar flares as proxy for the young Sun: satellite observed thermosphere response to an X17.2 flare of Earth's upper atmosphere, Ann. Geophys., 30, 1129-1141, https://doi.org/10.5194/angeo-30-1129-2012.

Kronberg EA, Bucik R, Haaland S, et al (2011): On the origin of the energetic ion events measured upstream of the Earth's bow shock by STEREO, Cluster, and Geotail, J. Geophys. Res., 116, A02210, doi:10.1029/2010JA015561

Ku S-B, Edwards GE, Tanner CB (1977), Effects of Light, Carbon Dioxide, and Temperature on Photosynthesis, Oxygen Inhibition of Photosynthesis, and Transpiration in Solanum tuberosum, Plant Physiol, 59, 868-872, doi:10.1104/pp.59.5.868

Kumar S, Hanson WB (1980), The morphology of metallic ions in the upper atmosphere, J. Geophys Res., 85, 6783-6801, doi:10.1029/JA085iA12p06783

Lammer H, Kasting JF, Chassefière E, et al (2008), Atmospheric escape and evolution of terrestrial planets and satellites, Space Sci. Rev., 139, 399-436, doi:10.1007/s11214-008-9413-5

Lammer H, Sproß L, Grenfell JL et al (2019), The role of N2 as a geo-biosignature for the detection and characterization of Earth-like habitats, Astrobiology, 19, 927-950, doi:10.1089/ast.2018.1914

Langowski MP, von Savigny C, Burrows JP, Feng W, Plane JMC, et al (2015) Global investigation of the Mg atom and ion layers using SCIAMACHY/Envisat observations between 70 and 150 km altitude and WACCM-Mg model results. Atmos. Chem. Phys. 15:273-295, doi:10.5194/acp-15-273-2015

Lawrence, A, Rawls, M.L, Jah, M. et al (2022), The case for space environmentalism. Nature Astronomy, 6, 428-435 doi:10.1038/s41550-022-01655-6

Leblanc, F, Schmidt, C, Mangano, V. et al (2022), Comparative Na and K Mercury and Moon Exospheres. Space Sci Rev 218, 2, doi:10.1007/s11214-022-00871-w

Lee JH, Kim KH, Baek SM et al (2024), The relationship between the energization of Moon-originating ions and terrain type on the lunar surface. J. Geophys. Res., 129, e2023JA032076, doi:10. 1029/2023JA032076

Lennartsson OW, Collin HL, Ghielmetti AG, and Peterson WK (2000) JASTP, 62(6), 477-483. A statistical comparison of the outflow of N_2^+, NO^+ and O_2^+ molecular ions with that of atomic O^+ ions using Polar/TIMAS observations. doi:10.1016/S1364-6826(00)00019-5

Le Roy L, Altwegg K, Balsiger H, et al (2015) Inventory of the volatiles on comet 67P/Churyumov-Gerasimenko from Rosetta/ROSINA. Astronomy and Astrophysics 583:A1. https://doi.org/10.1051/0004-6361/201526450

Lips T, Wartemann V, Koppenwallner G, Klinkrad H, et al (2005), Comparison of ORSAT and SCARAB reentry survival results, in Proceedings of 4th European Conference on Space Debris, 587, 533

Lin M-Y and Ilie R (2022) A review of observations of molecular ions in the Earth's magnetosphere-ionosphere system, Frontiers Astronomy Space Sci., 8, https://doi.org/10.3389/fspas.2021.745357

Liou J-C, Hall DT, Krisko PH, and Opiela JN (2004) LEGEND - a three-dimensional LEO-to-GEO debris evolutionary model, Adv Space Res, 34, 981-986, doi:10.1016/j.asr.2003.02.027

Lodders K, Palme H, and Gail H-P (2009), Abundances of the elements in the solar system, Chapter 4.4, in Landolt-Börnstein, Group VI Astronomy and Astrophysics 4B (Solar System), Springer-Verlag, Berlin, doi:materials.springer.com/lb/docs/sm_lbs_978-3-540-88055-4_34

Loesche WJ (1969) Oxygen sensitivity of various anaerobic bacteria, Appl. Microbiol., 18, 723-727

Loranc M., Hanson WB, Heelis RA, andSt-Maurice J-P (1991), A morphological study of vertical ionospheric flows in the high-latitude region, J. Geophys. Res., 96, 3627-3646, doi:10.1029/90JA02242.

Lundin R (1997) Observational and theoretical aspects of processes other than merging and diffusion governing plasma transport across the magnetopause. 80:269-304. https://doi.org/10.1023/A:1004930105714

Lundin, R. and Guglielmi, A. (2006), Ponderomotive forces in cosmos, Space Sci. Rev., 127, 1-116. https://doi.org/10.1007/s11214-006-8314-8

Mabie J, Bullett T, Moore P, and Vieira G (2016), Identification of rocket-induced acoustic waves in the ionosphere, Geophys. Res. Lett., 43, 11024-11029, doi:10.1002/2016GL070820

McComas, D.J., Alexander, N., Allegrini, F. et al (2017), The Jovian Auroral Distributions Experiment (JADE) on the Juno Mission to Jupiter, Space Sci Rev 213, 547-643. doi:10.1007/s11214-013-9990-9

Magg E, Bergemann M, Serenelli A, et al (2022), Observational constraints on the origin of the elements IV. Standard composition of the Sun, Astron. Astrophys, 661, A140, https://doi.org/10.1051/0004-6361/202142971

Mahaffy PR, Hodges RR, Benna M, et al (2015), The neutral mass spectrometer on the lunar atmosphere and dust environment explorer mission, in "The Lunar Atmosphere and Dust Environment Explorer Mission (LADEE)", editted by Elphic, R. and Russell, C., Springer, Cham, https://doi.org/10.1007/978-3-319-18717-4_3

Mall U, E. Kirsch K, Cierpka B et al (1998), Direct observation of lunar pick-up ions near the Moon, Geophys. Res. Lett., 25(20), 3799-3802, https://doi.org/10.1029/1998GL900003

Manuel OK, Hwaung G (1983) Solar abundances of the elements. Meteoritics 18:209. https://doi.org/10.1111/j.1945-5100.1983.tb00822.x

Mann I, et al (2010), Dust plasma interactions in near earth space and interplanetary medium, Space Sci. Rev. 161, 1- 47.

Mathews, J. D. (2020): New lidar observations of Ca^+ in the mesosphere and lower thermosphere over Arecibo, Geophysi. Res. Lett., 47, e2020GL087113, 2020. https://doi.org/10.1029/2020GL087113

Mitchell DG, Roelof EC, Bame SJ (1983) Solar wind iron abundance variations at speeds 600 km s^{-1}, 1972-1976. J. Geophys. Res. 88, 9059-9068. https://doi.org/10.1029/JA088iA11p09059

Moore TE, and Delcourt DC (1995), The geopause, Rev. Geophys., 33, 175-209, doi:10.1029/95RG00872

Moore TE, Chappell CR, Chandler MO et al (1995), The Thermal Ion Dynamics Experiment and Plasma Source Instrument. Space Sci Rev 71, 409-458, doi:10.1007/BF00751337

Moore TE, Peterson WK, Russell CT, et al (1999), Ionospheric mass ejection in response to a CME, Geophys. Res. Lett., 26, 2339-2342, doi:10.1029/1999GL900456

Murphy DM, Abou-Ghanem M, Cziczo DJ, et al (2023) Metals from spacecraft reentry in stratospheric aerosol particles. Proc Natl Acad Sci USA 120:e2313374120. https://doi.org/10.1073/pnas.2313374120

Nahar SN, Bautista MA, & Pradhan AK (1997). Electron-ion recombination of neutral iron. The Astrophysical Journal, 479, 497-503.

Nakamura E, Makishima A, Moriguti T, et al (2012) Space environment of an asteroid preserved on micrograins returned by the Hayabusa spacecraft. Proc. Natl. Acad. Sci.,109, E624-E629. https://doi.org/10.1073/pnas.1116236109

Nesvorny D, Janches D, Vokrouhlicky D, et al (2011) Dynamical model for the zodiacal cloud and sporadic meteors. Astrophys. J. 743, 129, doi:10.1088/0004-637X/743/2/129

Nicolaou G, Yamauchi M, Nilsson H, Wieser M, and Fedorov A (2017), Simulations as a tool for higher mass resolution spectrometer: Lessons from existing observations, Geophys. Res. Abstr., 19, EGU2017-16565, presented at EGU General Assembly, Vienna, April 2017

Nilsson H, Waara M, Arvelius S, et al (2006) Characteristics of high altitude oxygen ion energization and outflow as observed by Cluster: a statistical study, Ann. Geophys., 24, 1099-1112, https://doi.org/10.5194/angeo-24-1099-2006

Nilsson H, Waara M, Marghitu O, et al (2008), An assessment of the role of the centrifugal acceleration mechanism in high altitude polar cap oxygen ion outflow. Ann. Geophys., 26, 145-157. Doi: 10.5194/angeo-26-145-2008

Noble ST (1990) A large-amplitude traveling ionospheric disturbance excited by the space shuttle during launch, J. Geophys. Res., 95, 19037-19044, doi:10.1029/JA095iA11p19037

Nozawa S., Kawahara TD, Saito N, et al (2014), Variations of the neutral temperature and sodium density between 80 and 107 km above Tromsø during the winter of 2010-2011 by a new solid state sodium LIDAR, J. Geophys. Res., 119, doi:10.1002/2013JA019520, 441-451, 2014.

Ogawa Y, Seki K, Keika K, Ebihara Y (2019), Characteristics of CME- and CIR-driven ion upflows in the polar ionosphere, J. Geophys. Res., 124, 3637-3649

Ogilvie KW, Coplan MA (1995) Solar wind composition. Reviews of Geophysics 33:615-622. https://doi.org/10.1029/95RG00122

Park S-H, Laboulais JN, Leyland P, and Mischler S (2021), Re-entry survival analysis and ground risk assessment of space debris considering by-products generation, Acta Astronautica, 179, 604-618, doi:10.1016/j.actaastro.2020.09.034

Paschmann G (1997) Observational evidence for transfer of plasma across the magnetopause. 80:217-234. https://doi.org/10.1023/A:1004926004806

Paschmann G, Haaland SE, Phan TD, et al (2018) Large-scale survey of the structure of the dayside magnetopause by MMS. J Geophys Res 123:2018-2033. https://doi.org/10.1002/2017JA025121

Passas-Varo M, Van der Velde O, Gordillo-Vázquez FJ, et al (2023), Spectroscopy of a mesospheric ghost reveals iron emissions, Nat Commun 14, 7810, doi:10.1038/s41467-023-42892-1

Peterson WK, Andersson L, Callahan BC, et al (2008), Solar-minimum quiet time ion energization and outflow in dynamic boundary related coordinates, J. Geophys. Res., 113, A07222, doi:10.1029/2008JA013059

Perry CH, Grande M, Zurbuchen TH, et al (2000), Use of Fe charge state changes as a tracer for solar wind entry to the magnetosphere, Geophysical Res. Lett., 27, 2441-2444, doi:10.1029/2000GL003780

Pillinger CT, Gardiner LR, Jull AJT (1976) Preferential sputtering as a method of producing metallic iron, inducing major element fractionation and trace element enrichment. Earth and Planetary Science Letters 33:289-299. https://doi.org/10.1016/0012-821X(76)90237-5

Plane JMC (1991) The chemistry of meteoric metals in the Earth’s upper atmosphere, International Reviews in Physical Chemistry, 10, 55-106. https://doi.org/10.1080/01442359109353254

Plane JMC (2003) Atmospheric chemistry of meteoric metals. Chem. Rev. 103:4963-4984, doi:10.1021/cr0205309

Plane JMC (2012), Cosmic dust in the earth's atmosphere, Chem. Soc. Rev., 41, 6507-6518, doi;10.1039/c2cs35132c

Plane JMC, Cox RM, Rollason RJ (1999) Metallic layers in the mesopause and lower thermosphere region. Advances in Space Research 24:1559-1570. https://doi.org/10.1016/S0273-1177(99)00880-7

Plane JMC, Feng W, Dawkins ECM (2015a) The mesosphere and metals: Chemistry and changes, Chem. Rev., 115, 4497-4541, doi:10.1021/cr500501m

Plane JMC, Bailey SM, Baumgarten G, Rapp M (2015b) Layered phenomena in the mesopause region. J. Atmos. Solar-Terrestr. Phys. 127:1-2, https://doi.org/10.1016/j.jastp.2015.04.008

Plane JMC, Carrillo-Sanchez JD, Mangan TP, et al (2018a) Meteoric metal chemistry in the martian atmosphere. J. Geophys. Res., 123, 695-707. doi:10.1002/2017JE005510

Plane JMC, Flynn GJ; Määttänen A, Moores JE, Poppe AR, Carrillo-Sanchez JD, Listowski C (2018b), Impacts of Cosmic Dust on Planetary Atmospheres and Surfaces, Space Sci. Rev., 214, 23, doi:10.1007/s11214-017-0458-1

Plane JMC, Daly SM, Feng W, Gerding M, Gomez Martin JC (2021), Meteor-ablated aluminum in the mesosphere-lower thermosphere. J. Geophys. Res, 126, e2020JA028792, doi:10.1029/2020JA028792

Popova OP, Strelkov AS, and Sidneva SN (2007), Sputtering of fast meteoroids' surface, Adv. Space Res., 30, 567-573, doi:10.1016/j.asr.2006.05.008.

Poppe AR, Samad R, Halekas JS, et al (2012), ARTEMIS observations of lunar pick-up ions in the terrestrial magnetotail lobes, Geophys. Res. Lett., 39, L17104, doi:10.1029/2012GL052909

Poppe AR, Fillingim MO, Halekas JS, Raeder J, and Angelopoulos V (2016a), ARTEMIS observations of terrestrial ionospheric molecular ion outflow at the Moon, Geophys. Res. Lett., 43, 6749-6758, doi:10.1002/2016GL069715.

Poppe AR, Halekas JS, Szalay JR, Horányi M, Levin Z, and Kempf S (2016b), LADEE/LDEX observations of lunar pickup ion distribution and variability, Geophys. Res. Lett., 43, 3069-3077, doi:10.1002/2016GL068393.

Quinn JM and McIlwain CE (1979), Bouncing ion clusters in the Earth's magnetosphere, J. Geophys. Res., 82, 7365-7370, https://doi.org/10.1029/JA084iA12p07365

Rafano Carná SF, and Bevilacqua R (2019), High fidelity model for the atmospheric re-entry of CubeSats equipped with the Drag De-Orbit Device, Acta Astronautica, 156, 134-156, doi:10.1016/j.actaastro.2018.05.049

Raizada S, Tepley CA, Zhou Q, et al (2015) Dependence of mesospheric Na and Fe distributions on electron density at Arecibo. Earth, Planets, and Space 67:146. https://doi.org/10.1186/s40623-015-0322-z

Raizada S, Smith JA, Lautenbach J, Aponte N, Perillat P, Sulzer M, & Mathews JD (2020), New lidar observations of Ca+ in the mesosphere and lower thermosphere over Arecibo, Geophys. Res. Lett., 47, e2020GL087113, doi:10.1029/2020GL087113.

Reames DV (1995) Coronal abundances determined from energetic particles, Adv. Space Res.h 15,41-51

Reames DV, Meyer JP, von Rosenvinge TT (1994) Energetic-particle abundances in impulsive solar flare events. Astrophysical Journal Supplement 90:649. https://doi.org/10.1086/191887

Reinhard R (1986) The giotto experiments. ESA Journal 46:41-51

Reisenfeld DB, Burnett DS, Becker RH, et al (2007) Elemental abundances of the bulk solar wind: Analyses from genesis and ACE. 130:79-86. https://doi.org/10.1007/s11214-007-9215-1

Raizada, S., Smith, J. A., Lautenbach, J., Aponte, N., Perillat, P., Sulzer, M., and

Rème H, Aoustin C, Bosqued JM, et al (2001) First multispacecraft ion measurements in and near the Earth's magnetosphere with the identical Cluster ion spectrometry (CIS) experiment, Ann. Geophys., 19, 1303, doi: 10.5194/angeo-19-1303-2001

Reme H, Bosqued JM, Sauvaud JA, et al (1997) The cluster ion spectrometry (cis) experiment. 79:303-350. https://doi.org/10.1023/A:1004929816409

Reynolds R, Jost J, Rubin G, and J. Vila J (2001), Radar measurements of the reentry of the ariane 504 EPC, Adv. Space Res., 28, 1269-1275, doi:10.1016/S0273-1177(01)00396-9

Richards PG, Torr DG, Reinisch BW, et al (1994) F2 peak electron density at Millstone Hill and Hobart: Comparison of theory and measurement at solar maximum, J. Geophys. Res., 99, 15005-15016, doi:10.1029/94JA00863

Rieck KA (2015) Solar Wind Sodium and Potassium Abundance Analysis in Genesis Diamond-on-Siliconand Silicon Bulk Solar Wind Collectors, and How Hydration Affects the Microtexture of Olivine Phase Transformation at 18 GPa. Phd, University of Arizona

Rojas J, Duprat J, Engrand C, et al (2021), The micrometeorite flux at Dome C (Antarctica), monitoring the accretion of extraterrestrial dust on Earth, Earth and Planetary Science Letters, 560, art. no.: 116794, doi:10.1016/j.epsl.2021.116794

Ryabova GO, Asher DJ, Campbell-Brown MD (2019) Meteoroids: Sources of meteors on earth and beyond. Cambridge University Press

Sagdeev RZ, Kissel J, Bertaux JL, et al (1986) The element composition of comet Halley dust particles - preliminary results from the VEGA PUMA analyzers. Soviet Astronomy Letters 12:254

Saito Y, Yokota S, Asamura K, et al (2010), In-flight Performance and Initial Results of Plasma Energy Angle and Composition Experiment (PACE) on SELENE (Kaguya), Space Sci. Rev., 154, 1-4, 265-303, doi:10.1007/s11214-010-9647-x

Sarantos M, Hartle RE, Killen RM, et al (2012), Flux estimates of ions from the lunar exosphere, Geophys. Res. Lett., 39, L13101, doi:10.1029/2012GL052001.

Sarris et al (2020), Earth Explorer 10 candidate mission Daedalus: report for assessment, https://esamultimedia.esa.int/docs/EarthObservation/EE10_Daedalus_Report-for-Assessment-v1.0_13Nov2020.pdf

Schillings A, Nilsson H, Slapak R, et al (2017) Relative outflow enhancements during major geomagnetic storms - Cluster observations, Ann. Geophys., 35, 1341-1352, https://doi.org/10.5194/angeo-35-1341-2017

Schmid J, Bochsler P, Geiss J (1988) Abundance of iron ions in the solar wind. 329:956. https://doi.org/10.1086/166440

Schneider NM, Deighan JI, Stewart AIF, et al (2015), MAVEN IUVS observations of the aftermath of the Comet Siding Spring meteor shower on Mars, Geophys. Res. Lett. 42, 4755-4761, doi:10.1002/2015GL063863

Schulz L and Glassmeier K-H (2021) On the anthropogenic and natural injection of matter into Earth's atmosphere, Adv. Space Res. 67,1002-1025. doi:10.1016/j.asr.2020.10.036

Schunk R., and Nagy A. (2009), Ionospheres, Cambridge Univ. Press, Cambridge, U.K.

Seki K, Hirahara M, Terasawa T, et al (1998), Statistical properties and possible supply mechanisms of tailward cold O+ beams in the lobe/mantle regions, J. Geophys. Res., 103, 4477-4489, doi:10.1029/97JA02137

Seki K, Keika K, Kasahara S, et al (2019). Statistical properties of molecular ions in the ring current observed by the Arase (ERG) satellite. Geophys. Res. Lett., 46, 8643-8651, doi:10.1029/ 2019GL084163

Servaites JC (1977), pH Dependence of Photosynthesis and Photorespiration in Soybean Leaf Cells, Plant Physiol, 60, 693-696, doi:10.1104/pp.60.5.693

Shelley EG, Johnson RG, and Sharp RD (1972), Satellite observations of energetic heavy ions during a geomagnetic storm, J. Geophys. Res., 77, 6104--6110, doi:10.1029/JA077i031p06104.

Shelley EG, Simpson DA, Sanders TC (1981), The energetic ion composition spectrometer (EICS) for the Dynamics Explorer-A, Space Sci. Instrum., 5, 443-454.

Shelley EG, Ghielmetti AG, Balsiger H, et al (1995), The Toroidal Imaging Mass-Angle Spectrograph (TIMAS) for the polar mission. Space Sci Rev 71, 497-530. doi:10.1007/BF00751339

Shinagawa H and Oyama S (2006): A two-dimensional simulation of thermospheric vertical winds in the vicinity of an auroral arc. Earth Planet Space 58, 1173ΓÇô1181 2006. https://doi.org/10.1186/BF03352007

Simpson JA (1983) Elemental and isotopic composition of the galactic cosmic rays. Annual Review of Nuclear and Particle Science 33:323-382. https://doi.org/10.1146/annurev.ns.33.120183.001543

Slapak R, Schillings A, Nilsson H, et al (2017), Atmospheric loss from the dayside open polar region and its dependence on geomagnetic activity: Implications for atmospheric escape on evolutionary timescales. Annales Geophysicae, 35, 721-731, doi: 10.5194/angeo-35-721-2017

Solomon SC (1991) Optical aeronomy. Reviews of Geophysics 29:1089-1109

Stasiewicz K, Markidis S, Eliasson B, et al (2013), Acceleration of solar wind ions to 1 MeV by electromagnetic structures upstream of the Earth's bow shock, Europhys. Lett., 102, 49001, doi:10.1209/0295-5075/102/49001

Stern SA (1999), The lunar atmosphere: History, status, current problems, and context. Rev. Geophys. 37 (4), 453-491, doi:10.1029/1999RG900005

Stüdemann W, Wilken B (1982) Detection efficiency of a heavy ion time-of-flight spectrometer with thin carbon foils in the start detector. Review of Scientific Instruments 53:175-180. https://doi.org/10.1063/1.1136948

Stüeken EE, Som SM, Claire M et al (2020), Mission to Planet Earth: The First Two Billion Years. Space Sci. Rev., 216, doi:10.1007/s11214-020-00652-3

Sydorenko D, Rankin R, and Yau AW (2016), Enhanced N^2 and O^2 densities inferred from EISCAT observations of Pc5 waves and associated electron precipitation, J. Geophys. Res. Space Physics, 121, 549–566, doi:10.1002/2015JA021508

Takada M, Seki K, Ogawa Y, et al (2021), Low-altitude ion upflow observed by EISCAT and its effects on supply of molecular ions in the ring current detected by Arase (ERG). J. Geophys. Res., 126, e2020JA028951, https://doi.org/10.1029/2020JA028951

Tanaka T, Saito Y, Yokota S, et al (2009), First in situ observation of the Moon-originating ions in the Earth's Magnetosphere by MAP-PACE on SELENE (KAGUYA), Geophys. Res. Lett., 36, L22106, doi:10.1029/2009GL040682

Terada K, Yokota S, Saito Y, et al (2017). Biogenic oxygen from Earth transported to the Moon by a wind of magnetospheric ions. Nature Astronomy, 1, 0026, doi: 10.1038/s41550-016-0026

Tsuda TT, Chu X, Nakamura T, et al (2015), A thermospheric Na layer event observed up to 140 km over Syowa Station (69.0ºS, 39.6ºE) in Antarctica, Geophys. Res. Lett., 42, 3647-3653, doi:10.1002/2015GL064101, 2015.

Thomas E, Simolka J, DeLuca M, Horanyi M, Janches D, Marshall RA, Munsat T, Plane JMC, and Sternovsky Z (2017), Experimental setup for the laboratory investigation of micrometeoroid ablation using a dust accelerator, Rev. Sci. Instrum., 88, 034501, doi.org:10.1063/1.4977832

Treumann RA, Labelle J, Bauer TM (1995) Diffusion processes: An observational perspective. Washington DC American Geophysical Union Geophysical Monograph Series 90:331. https://doi.org/10.1029/GM090p0331

Vierinen J, Fentzke J, Miller E (2014) An explanation for observations of apparently high-altitude meteors. MNRAS 438:2406-2412. doi:10.1093/mnras/stt2358

Vondrak T, Plane JMC, Broadley SL, and Janches D (2008), A chemical model of meteoric ablation, Atmospheric Chemistry and Physics, 8, 7015-7031, doi:10.5194/acp-8-7015-2008

von Steiger R. (1995). Solar wind composition and charge states. Solar Wind Eight, Dana Point, CA, USA, Eds. D. Winterhalter, J.T. Gosling, S.R. Habbal, W.S. Kurth and M. Neugebauer, AIP Press, 193-198.

von Steiger R, Geiss J, Gloeckler G (1997) Composition of the solar wind. in "Cosmic winds and the heliosphere". p 581

von Steiger R, Schwadron NA, Fisk LA, et al (2000) Composition of quasi-stationary solar wind flows from Ulysses/Solar wind ion composition spectrometer. J. Geophys. Res. 105:27217-27238. https://doi.org/10.1029/1999JA000358

von Steiger R, Zurbuchen TH (2002) Kinetic properties of heavy solar wind ions from Ulysses-SWICS, Adv. Space Res., 30, 73-78. https://doi.org/10.1016/S0273-1177(02)00174-6

von Steiger R, Zurbuchen TH, McComas DJ (2010) Oxygen flux in the solar wind: Ulysses observations. 37, L22101, https://doi.org/10.1029/2010GL045389

von Zahn U, Höffner J, McNeil WJ (2002) Meteor trails as observed by lidar. In: Murad E, Williams IP (eds) Meteors in the earth's atmosphere. p 149 von Zahn, U. (2005), The total mass flux of meteoroids into the Earth's upper atmosphere, in proceedings of 17th ESA Symposium on European Rocket and Balloon Programmes and Related Research, 30 May - 2 June 2005, ESA SP-590, 33-39

Vorburger A, Wurz P, Barabash S, et al (2014), First Direct Observation of Sputtered Lunar Oxygen, J. Geophys. Res. 119(2), 709-722.

Wahlund J-E, Opgenoorth HJ, Häggström I, et al (1992), EISCAT observations of topside ionospheric ion outflows during auroral activity: Revisited, J. Geophys. Res., 97(A3), 3019-3037, doi:10.1029/91JA02438

Werner R, Guineva V, Stoeva P, Spasov St (1989) The spectrum of comet Halley obtained by VEGA-2. Advances in Space Research 9:221-224. https://doi.org/10.1016/0273-1177(89)90264-0

Westphal AJ, Huss GR, Koeman-Shields E, et al (2019) Abundance of manganese in the solar wind using dual-implant calibration. LPI

Whalen BA, Burrows JR, Yau AW, et al (1990), The suprathermal ion mass spectrometer (SMS) onboard the Akebono (EXOS-D) satellite, J. Geomagn. Geoelectr., 42, 511-536. doi:10.5636/jgg.42.511

Whalen BA, Watanabe S, and Yau AW (1991) Observations in the transverse ion energization region, Geophys. Res. Lett., 18, 725–728, doi:10.1029/90GL02788

Wiegert P, Vaubaillon J, Campbell-Brown M (2009) A dynamical model of the sporadic meteoroid complex, Icarus, 201, 295-310, doi:10.1016/j.icarus.2008.12.030

Wieser M, and Barabash S (2016), A family for miniature, easily reconfigurable particle sensors for space plasma measurements, J. Geophys. Res. 121, 11588-11604, doi:10.1002/2016JA022799.

Wieser M, Barabash S, Futaana Y, et al (2010), First observation of a mini-magnetosphere above a lunar magnetic anomaly using energetic neutral atoms, Geophys. Res. Lett., 37, L05103, doi:10.1029/2009GL041721.

Wieser M., Barabash S., Wang X.-D., Grigoriev A., Zhang A., Wang C., and Wang W. (2020a), The Advanced Small Analyzer for Neutrals (ASAN) on the Chang'E-4 Rover Yutu-2. Space Sci. Rev., 216, 73, doi: 10.1007/s11214-020-00691-w

Wieser M., Barabash S., Wang X.-D., Zhang A., Wang C., and Wang W. (2020b), Solar wind interaction with the lunar surface: Observation of energetic neutral atoms on the lunar surface by the Advanced Small Analyzer for Neutrals (ASAN) instrument on the Yutu-2 rover of Chang'E-4, presentation at EGU General Assembly 2020, May 2020, doi:10.5194/egusphere-egu2020-9199

Wilken B, Stüdemann W (1984) A compact time-of-flight mass-spectrometer with electrostatic mirrors. Nuclear Instruments and Methods in Physics Research 222:175-180. https://doi.org/10.1016/0167-5087(84)90391-0

Wilken B, Weiss W, Stuedemann W, Hasebe N (1987) The Giotto implanted ion spectrometer (IIS): physics and techniques of detection. Journal of Physics E Scientific Instruments 20:778-785. https://doi.org/10.1088/0022-3735/20/6/036

Wilken B, Axford WI, Daglis I, et al (1997) RAPID - the imaging energetic particle spectrometer on cluster. Space Science Reviews 79:399-473. https://doi.org/10.1023/A:1004994202296

Wilken B, Daly PW, Mall U, et al (2001) First results from the RAPID imaging energetic particle spectrometer on board Cluster. Ann Geophys 19:1355-1366. https://doi.org/10.5194/angeo-19-1355-2001

Williams DJ, et al (1994), Geotail energetic particles and ion composition instrument, J. Geomag. Geoelectr., 46,39-57

Wimmer-Schweingruber RF, Crooker NU, Balogh A, et al (2006) Understanding Interplanetary Coronal Mass Ejection Signatures, Space Sci. Rev. 123, 177-216, doi10.1007/s11214-006-9017-x

Wittmann P (2022), The Jovian Plasma Dynamics and Composition Analyzer (JDC) for ESA's JUICE mission, PhD thesis, Kiruna: Umeå University and Swedish Institute of Space Physics, 2022. IRF Scientific Reports 314. ISBN: 978-91-7855-770-7 (digital) ISBN: 978-91-7855-769-1 (print) https://urn.kb.se/resolve?urn=urn:nbn:se:umu:diva-193773

Wu JF, Feng W, Liu HL, et al (2021) Self-consistent global transport of metallic ions with WACCM-X. Atmos Chem Phys 21:15619-15630, doi:10.5194/acp-21-15619-2021

Wüest M, Evans DS, and von Steiger R (2007), Calibration of Particle Instruments in Space Physics, ISSI Scientific Report, SR-007, International Space Science Institute, Bern, Switzerland, https://www.issibern.ch/PDF-Files/SR-007.pdf.

Wurz P (2005), Solar wind composition, In “The Dynamic Sun: Challenges for Theory and Observations”, ESA SP-600, 5.2, 1-9

Wurz P (2012), Erosion Processes Affecting Interplanetary Dust Grains, in Nano Dust in the Solar System: Discoveries and Interpretations. Springer-Verlag Berlin Heidelberg, Astrophysics and Space Science Library, Volume 385, 161-178, doi:10.1007/978-3-642-27543-2_8

Wurz, P., Gubler L., Bochsler P., and Möbius E., "Isochronous Mass Spectrometry for Space Plasma Applications," American Geophysical Union Monograph on Measurement Techniques for Space Plasmas, Vol. 102 (1998), 229-235.

Wurz P., R.F. Wimmer-Schweingruber, K. Issautier, P. Bochsler, A.B. Galvin, and F.M. Ipavich (2001), Composition of magnetic cloud plasmas during 1997 and 1998, American Institute Physics on Solar and Galactic Composition, CP-598, 145-151.

Wurz P, Wimmer-Schweingruber R, Bochsler P, Galvin A, Paquette JA, and Ipavich F (2003),"Composition of magnetic cloud plasmas during 1997 and 1998, Solar Wind X, American Institute Physics, 679, 685-690.

Wurz P, Bochsler P, Paquette JA, and Ipavich FM (2003) Calcium abundance in the solar wind. 583:489-495. https://doi.org/10.1086/344834

Wurz P., Gamborino D., Vorburger A., and Raines J.M. (2019), "Heavy Ion Composition of Mercury's Magnetosphere," Jou. Geophys. Res. 124, 2603-2612, doi:10.1029/2018JA026319.

Wurz P, Rohner U, Whitby JA, Kolb C, Lammer H, Dobnikar P, and Martín-Fernández JA (2007), "The Lunar Exosphere: The Sputtering Contribution," Icarus 191, 486-496, doi10.1016/j.icarus.2007.04.034.

Wurz P, Fatemi S, Galli A, et al (2022), Particles and photons as drivers for particle release from the surfaces of the Moon and Mercury, Space Sci. Rev., 218(3), 83 pages, doi:10.1007/s11214-022-00875-6.

Xie L, Li L, Zhang A, et al (2021). Inside a lunar mini-magnetosphere: First energetic neutral atom measurements, Geophys. Res. Lett., 48, e2021GL093943. https://doi.org/10.1029/2021GL093943

Xie L, Zhang A, Li L, et al (2022), Chang'E-4 Energetic Neutral Atom Observation Reveals New Features about the Solar Wind-Moon Interaction. Chinese J. Space Sci., 42, 11-24, doi:10.11728/cjss2022.01.20220113

Yamauchi M (2019), Terrestrial ion escape and relevant circulation in space, Ann. Geophys., 37, 1197-1222, doi:10.5194/angeo-37-1197-2019

Yamauchi M, Eliasson L, Lundin R, and Norberg O (2005): Unusual heavy ion injection events observed by Freja, Ann. Geophys., 23, 535-543, https://doi.org/10.5194/angeo-23-535-2005.

Yamauchi M, Johnsen MG, Enell C-F, et al (2020), High-latitude crochet: solar-flare-induced magnetic disturbance independent from low-latitude crochet, Ann. Geophys., 38, 1159-1170, doi:10.5194/angeo-38-1159-2020

Yau AW, Peterson WK and Shelley EG (1988), Quantitative Parametrization of Energetic Ionospheric Ion Outflow, in "Modeling Magnetospheric Plasma", eds T.E. Moore, J.H. Waite, T.W. Moorehead and W.B. Hanson, 211-217, AGU, doi:10.1029/GM044p0211

Yau AW and Whalen BA (1992) Auroral ion composition during large magnetic storms, Can. J. Physics, 70, 500-509, doi:10.1139/p92-085

Yau AW, Whalen BA, Goodenough C, et al (1993), EXOS D (Akebono) observations of molecular NO^+ and N_2^+ upflowing ions in the high-altitude auroral ionosphere. J. Geophys. Res., 98, 11205-11224, https://doi.org/10.1029/92JA02019

Yau AW and André M (1997). Sources of ion outflow in the high latitude ionosphere. Space Sci. Rev.s, 80, 1-25, doi:10.1023/A:1004947203046

Yau AW, James HG (2015) CASSIOPE enhanced polar outflow probe (e-POP) mission overview. 189:3-14. https://doi.org/10.1007/s11214-015-0135-1

Yau AW and Howarth A (2016), Imaging thermal plasma mass and velocity analyzer, J. Geophys. Res., 121, 7326-7333, doi:10.1002/2016JA022699

Yau AW, Abe T, André M, Howarth AD, and Peterson WK (2021), Ionospheric Ion Acceleration and Transport, in “Space Physics and Aeronomy Collection Volume 2: Magnetospheres in the Solar System, Geophysical Monograph 259”, Edited by Romain Maggiolo, Nicolas André, Hiroshi Hasegawa, and Daniel T. Welling, American Geophysical Union, Published by John Wiley & Sons, Inc., doi: 10.1002/9781119815624.ch14

Yokota S and Saito Y (2005) Estimation of picked-up lunar ions for future compositional remote SIMS analyses of the lunar surface. Earth Planet Space, 57, 281-289 (2005). doi:10.1186/BF03352564

Yokota S, Saito Y, Asamura K, et al (2009), First direct detection of ions originating from the Moon by MAP-PACE IMA onboard SELENE (KAGUYA), Geophys. Res. Lett., 36, L11201, doi:10.1029/2009GL038185

Yokota S, Kasahara S, Mitani T, et al (2017): Medium-energy particle experiments-ion mass analyzer (MEP-i) onboard ERG (Arase), Earth Planets Space, 69, 172, https://doi.org/10.1186/s40623-017-0754-8

Yokota S, Terada K, Saito Y, et al (2020), KAGUYA observation of global emissions of indigenous carbon ions from the Moon. Sci. Adv., 6, eaba1050, https://doi.org/10.1126/sciadv.aba1050

Young PR (2005) The Ne/O abundance ratio in the quiet Sun. Journal of Astronomy and Astrophysics 444: L45-L48. https://doi.org/10.1051/0004-6361:200500206

Young DT, Geiss J, Balsiger H, et al (1977), Discovery of He^{2+} and O^{2+} ions of terrestrial origin in the outer magnetosphere, Geophys. Res. Lett., 4, 561-564, doi:10.1029/GL004i012p00561

Young DT, Balsiger H, Geiss J (1982) Correlations of magnetospheric ion composition with geomagnetic and solar activity. J. Geophys. Res. 87:9077-9096. https://doi.org/10.1029/JA087iA11p09077

Young DT, Burch JL, Gomez RG, et al (2016), Hot plasma composition analyzer for the magnetospheric multiscale mission. Space Sci. Rev., doi: 10.1007/s11214-014-0119-6

Zahnle KJ, Gacesa M, and Catling DC (2019), Strange messenger: A new history of hydrogen on Earth, as told by Xenon, Geochimica et Cosmochimica Acta, doi: 10.1016/j.gca.2018.09.017

Zettergren M., Semeter J., Burnett B., et al (2010), Dynamic variability in F-region ionospheric composition at auroral arc boundaries. Ann. Geophys. 28, 651-664, doi:10.5194/angeo-28-651-2010

Zettergren M., Semeter J., Heinselman C., and Diaz, M (2011), Incoherent scatter radar estimation of F region ionospheric composition during frictional heating events. J. Geophys. Res. 116, doi:10.1029/2010JA016035

Zhou, X.-Z., Angelopoulos, V., Poppe, A.R., and Halekas, J.S. (2013), ARTEMIS observations of lunar pickup ions: Mass constraints on ion species, J. Geophys. Res. Planets, 118, 1766-1774, doi:10.1002/jgre.20125, 2013.

Zurbuchen TH, Fisk LA, Gloeckler G, von Steiger R (2002) The solar wind composition throughout the solar cycle: A continuum of dynamic states. Geophysical Research Letters 29:1352. https://doi.org/10.1029/2001GL013946

Zurbuchen TH, Raines JM, Slavin JA, et al (2011) MESSENGER observations of the spatial distribution of planetary ions near mercury. Science 333:1862. https://doi.org/10.1126/science.1211302

Zurbuchen TH, Weberg M, von Steiger R, et al (2016) Composition of coronal mass ejections. The Astrophysical Journal 826:10. https://doi.org/10.3847/0004-637X/826/1/10